Wake Vortices of Landing Aircraft

Anton Stephan

München 2013

Wake Vortices of Landing Aircraft

Anton Stephan

Dissertation
an der Fakultät für Physik
der Ludwig–Maximilians–Universität
München

vorgelegt von
Anton Stephan
aus Charkow (Ukraine)

München, Dezember 2013

Erstgutachter: Prof. Dr. George Craig
Zweitgutachter: Prof. Dr. Ulrich Schumann
Tag der mündlichen Prüfung: 26.02.2014

Für meine Familie

Abstract

As a consequence of lift generation, flying aircraft generate a complex turbulent wake consisting of strong coherent flow structures. The evolution of the aircraft's wake prior to and directly after touchdown still poses many open questions. The dynamics as well as the numerical treatment of the wake flow are very challenging, as multiple scales determine the flow related to the complex geometry of an aircraft, the interaction with the ground surface, and the environmental conditions. The evolution of the aircraft's wake is an example of a complex turbulent flow challenging modern physics, because it is composed of strong coherent flow structures that exhibit a range of length scales spanning several orders of magnitude all interacting with one another. Fully rolled-up, two counter rotating wake vortices emerge, possessing a high amount of kinetic energy and therefore posing a potential hazard to following aircraft. To avoid wake-vortex encounters, aircraft regulatory separation distances have been introduced. In a growing economy the capacity problems of congested airports also get worse. Therefore, a process has been initiated by aviation authorities aiming at the recategorization of the static wake-vortex separations. Obviously, the safety of the passengers must not be compromised by any capacity increasing measures. Artificial devices for the alleviation of wake vortices could not be established so far.

A novel method for artificial wake-vortex decay enhancement, consisting of obstacles installed at the runway tails, is investigated in detail, with temporal large-eddy simulations (LES). First the mechanisms of wake-vortex decay of fully rolled-up vortices, interacting with a flat ground surface subjected to a turbulent crosswind, are studied. The simulations reveal that so-called crosswind streaks perturb the secondary vorticity layer at the ground surface, such that hairpin-shaped secondary vortices detach from the ground and trigger turbulent vortex decay. Obstacles at the ground surface trigger the rapid generation of powerful secondary vortices that interact vigorously with the primary vortices. Analyzing the vortex dynamics, it is found, that the obstacles trigger both, pressure disturbances propagating within the vortex cores and helical secondary vortex structures, propagating exteriorly along the primary vortices. A model for the propagation speed of the disturbances is elaborated. Plate lines are introduced as efficient alternative to massive obstacles that could not be installed in the vicinity of runways. Simulation results are compared with particle image velocimetry measurements accomplished in a water towing tank. Qualitatively the evolutions of vortex position and decay agree well.

In this thesis a method is developed to investigate the wake evolution during the complete landing phase, including final approach, flare, touchdown, and deceleration. Therefore a recently developed method to investigate the entire wake evolution from roll-up to decay is extended for downward sloping trajectories. For this purpose, the flow around an aircraft model in high-lift configuration, with deployed flaps and slats, obtained from a high-fidelity

Reynolds-averaged Navier-Stokes (RANS) simulation, is swept through the ground fixed LES domain. This way the peculiarities of the flow details around the complex aircraft geometry can be transferred to the vortex characteristics, developing during and after roll-up. The simulations reveal that so-called end effects, appearing shortly after touchdown, propagate along the wake vortices, leading to rapid decay. Disturbances generated by a plate line interact with the end effects and further accelerate vortex decay. During the decay phase, the vortices are subjected to complex deformations, strong divergence as well as ground linking. Flight measurement data gathered during the WakeMUC campaign at Munich airport are used to compare flow characteristics. Good agreement is found concerning the surprisingly complex vortex trajectories. Deviations from the observed decay rates can be attributed to the lack of wake turbulence initiation during the RANS-LES transition step, motivating further work.

Zusammenfassung

Als Folge des Auftriebs entsteht bei einem fliegenden Flugzeug eine komplexe turbulente Nachlaufströmung bestehend aus energiereichen kohärenten Strukturen. Die Entwicklung der Nachlaufwirbel vor und unmittelbar nach der Landung wirft viele ungeklärte Fragen auf. Sowohl die Dynamik, als auch die numerische Behandlung der Nachlaufströmung stellen eine große Herausforderung dar. Aufgrund der komplexen Flugzeuggeometrie, des Einflusses des Bodens und der meteorologischen Bedingungen bestimmen sehr unterschiedliche Skalen die Strömung. Somit stellt die Nachlaufentwicklung von Flugzeugen ein hervorragendes Beispiel für komplexe turbulente Strömungen und damit eine große Herausforderung der modernen Physik dar. Die entstehenden Wirbelströmungen sind besonders gekennzeichnet durch kohärente Strukturen, die mehrere Größenordnungen an Längenskalen überspannen und nichtlinear miteinander interagieren. Voll aufgerollt bilden sich zwei energiereiche, gegensinnig rotierende Nachlaufwirbel, die sogenannte Wirbelschleppe, die ein Risiko für nachfolgende Flugzeuge darstellt. Um Wirbelschleppenbegegnungen zu vermeiden, wurden an Flughäfen Staffelungsabstände zwischen aufeinander folgenden Flugzeugen eingeführt. In einer prosperierenden Wirtschaft werden Kapazitätsprobleme verkehrsreicher Flughäfen über die Jahre verschärft. Daraufhin haben Luftfahrtbehörden eine Überprüfung in die Wege geleitet, der die statische Flugzeugstaffelung neu gestalten soll. Dabei darf die Sicherheit der Fluggäste nicht durch kapazitätserweiternde Maßnahmen eingeschränkt werden. Effektive technische Vorrichtungen, die den Wirbelzerfall beschleunigen, wurden bisher noch nicht etabliert.

Eine neuartige Methode zur künstlichen Beschleunigung des Wirbelschleppenzerfalls, bestehend aus vor der Rollbahn aufgestellten Hindernissen, wird in dieser Arbeit weiter entwickelt und detailliert mit Large Eddy Simulationen (LES) untersucht. Dazu werden zunächst die Zerfallsmechanismen von voll-aufgerollten, mit dem Boden interagierenden Wirbeln, unter dem Einfluss eines Seitenwindes, betrachtet. Die Simulationen zeigen, dass streifenförmige Wirbel (Streaks) die induzierte Wirbelschicht am Boden stören, so dass sich Haarnadelwirbel vom Boden ablösen und turbulente Zerfallsprozesse der Wirbel auslösen. Die Hindernisse lösen gezielt die Entstehung von starken Sekundärwirbeln aus, die aktiv mit den Primärwirbeln interagieren. Es zeigt sich, dass die Hindernisse sowohl Druckstörungen im Wirbelkern, als auch Helix-artige Sekundärwirbel auslösen, die sich beide schnell entlang der Wirbel ausbreiten. Ein Modell für die Ausbreitungsgeschwindigkeit der Wirbel wird entwickelt. Plattenreihen (plate lines) stellen eine praktikable Alternative für massive Hindernisse in Landebahnnähe dar. Die Simulationen werden mit Messergebnissen von Strömungsfeldern (Particle Image Velocimetry) in Wasserschleppkanalexperimenten verglichen. Qualitativ stimmen die Entwicklung der Wirbelposition und des -zerfalls in Simulation und Experiment gut überein.

Ferner wird eine Methode entwickelt, die die Untersuchung der Nachlaufentwicklung während der kompletten Landung, einschließlich Anflug, Abfangen, Aufsetzen und Abbremsen, ermöglicht. Dafür wird eine kürzlich entwickelte Methode, die die vollständige Nachlaufentwicklung, vom Aufrollen bis zum Zerfall der Wirbel abdeckt, auf geneigte Trajektorien erweitert. Dazu wird die Umströmung eines Flugzeugmodells in Hochauftriebskonfiguration, mit ausgefahrenen Klappen und Vorflügeln, die vorab mit einer Reynoldsgemittelten Navier-Stokes (RANS) Simulation berechnet wurde, durch ein LES Rechengebiet gezogen. Dadurch werden Besonderheiten und Strömungsdetails der komplexen Flugzeugumströmung über den Aufrollvorgang auf die Wirbeleigenschaften übertragen. Die Simulationen zeigen, dass sogenannte Endeffekte, die kurz nach dem Aufsetzen entstehen, sich entlang der Wirbel ausbreiten und zu schnellem Zerfall führen. Die Störungen der Plattenreihen kollabieren mit den Endeffekten und verstärken den Zerfall zusätzlich. Während der Zerfallsphase werden die Wirbel auf komplexe Weise stark deformiert, sie divergieren und verbinden sich mit dem Boden. Simulationsergebnisse werden mit Messdaten verglichen, die während der WakeMUC Kampagne am Flughafen München gesammelt wurden. Gute Übereinstimmung kann bei den überraschend komplexen Wirbeltrajektorien beobachtet werden. Abweichungen bezüglich der Zerfallsraten können auf eine unvollständige Initialisierung der Turbulenz während der Assimilierung der RANS Strömungsfelder zurückgeführt werden und motivieren zukünftige Arbeiten.

Inhaltsverzeichnis

1. Introduction

1.1. Motivation

This dissertation is motivated by both, open questions in the fluid dynamics and simulation techniques of an aircraft's wake, as well as practical interests of airports, authorities, and passengers in the complex structure of growing economy and safety requirements. Aircraft generated trailing vortices pose a potential risk for following aircraft, due to strong coherent flow structures (Gerz et al., 2002). In cruise altitudes the evolution of the aircraft's wake is strongly dependent on the prevailing meteorological conditions (Misaka et al., 2012b). In ground proximity additionally the geometry and roughness of the ground surface influences the flow. The probability of encountering wake vortices increases significantly during final approach in ground proximity since the vortices may not descend below the glide path, to leave the flight corridor vertically. Instead they rebound, due to the interaction with the ground surface (Holzäpfel & Steen, 2007). Moreover, the advection by weak crosswinds may compensate the self-induced lateral vortex transport. Therefore the clearance of the flight corridor, by descent and advection of the vortices, is strongly restricted. Due to the low height of the aircraft above the ground, the possibility of the pilot being able to counteract the imposed rolling moment is limited. Consequently, the incident reporting scheme, compiled by the British National Air Traffic Services (NATS), lists most encounters at flight altitudes below 300 feet (Critchley & Foot, 1991).

The airport capacity problem is "as strong as ever". This is concluded by Eurocontrol in the recent summary report "Challenges of grows 2013" (Eurocontrol, 2013). Several scenarios for the future European airport demands are analyzed in this report, realizing that there will be unaccommodated flights in each case, see Fig.1.1. In the most-likely scenario C "Regulated Growth", around 1.9 million flights will not be accommodated, constituting approximately 12% of the demand in 2035.

For an optimal airport capacity, the aircraft separation of two following aircraft should be as small as possible. Still, the passenger and aircraft safety has to be ensured. As an operational minimum aircraft separation, used by the air traffic control (ATC), the minimum radar separation (MRS) corresponding mostly to 2.5 nautical miles (NM) is employed, not including wake-vortex separation. Wake vortex separations for arrivals were introduced by the International Civil Aviation Organization (ICAO) in the 1970's, distinguishing three different aircraft weight classes: small up to 7,000 kg, medium up to 136,000 kg and heavy for larger aircraft. The separation distances between the different weight class configurations vary from 2.5 NM to 6 NM (Gerz et al., 2002). In a rapidly growing aeronautical environment, the ICAO launched an initiative to increase airport capacity, aiming at dy-

	Unaccom-modated IFR Flights (million)	Unaccommodated demand (%)	
	2035	2035	2050
A: Global Growth	4.4	20%	36%
C: Regulated Growth	1.9	12%	19%
C': Happy Localism	1.0	7%	15%
D: Fragmenting World	0.2	2%	5%

Abbildung 1.1.: Scenarios of future airport demands. In the most-likely scenario C 1.9 million flights will not be accommodated (Eurocontrol, 2013).

namic pairwise aircraft separations. This means that depending on the local environmental conditions, like prevailing weather, runway constellation, and the involved aircraft, the separation is determined by a wake-vortex advisory system WVAS. The American Federal Aviation Administration (FAA), together with Eurocontrol, elaborated a three step agenda for the recatigorization (RECAT) of the separations. RECAT phase 1 introduced six different static aircraft classes, see Fig. 1.2 (a), and extended the separation matrix, Fig. 1.2 (b). It has already been successfully implemented at the Memphis International Airport (Lang & Lunsford, 2013). Phase 2 aims at airport independent static pair-wise separations, planned for 2015. Phase 3 shall establish dynamic pairwise separations of aircraft. Clearly, the ambitious goals of dynamic pairwise aircraft separations by RECAT will not be reached without an appropriate, optimally designed WVAS. Therefore a deep understanding of the wake-vortex physics is inevitable, in particular in ground proximity.

1.2. Aims of the Thesis

A lot of questions arise in the wide field of wake-vortex research. This thesis shall provide insights particularly into the wake flow field of landing aircraft, and explain the vortex dynamics that lead to vortex decay in ground proximity. It is focused on the following three questions:

- How can the flow field, generated by a landing aircraft, be simulated accurately?

It is known from numerical simulations, as well as from Light Detection And Ranging (LIDAR) measurements, that wake vortices may possess a critical strength, much longer than 2 minutes, corresponding to a 5 nautical miles (NM) separation for approach and

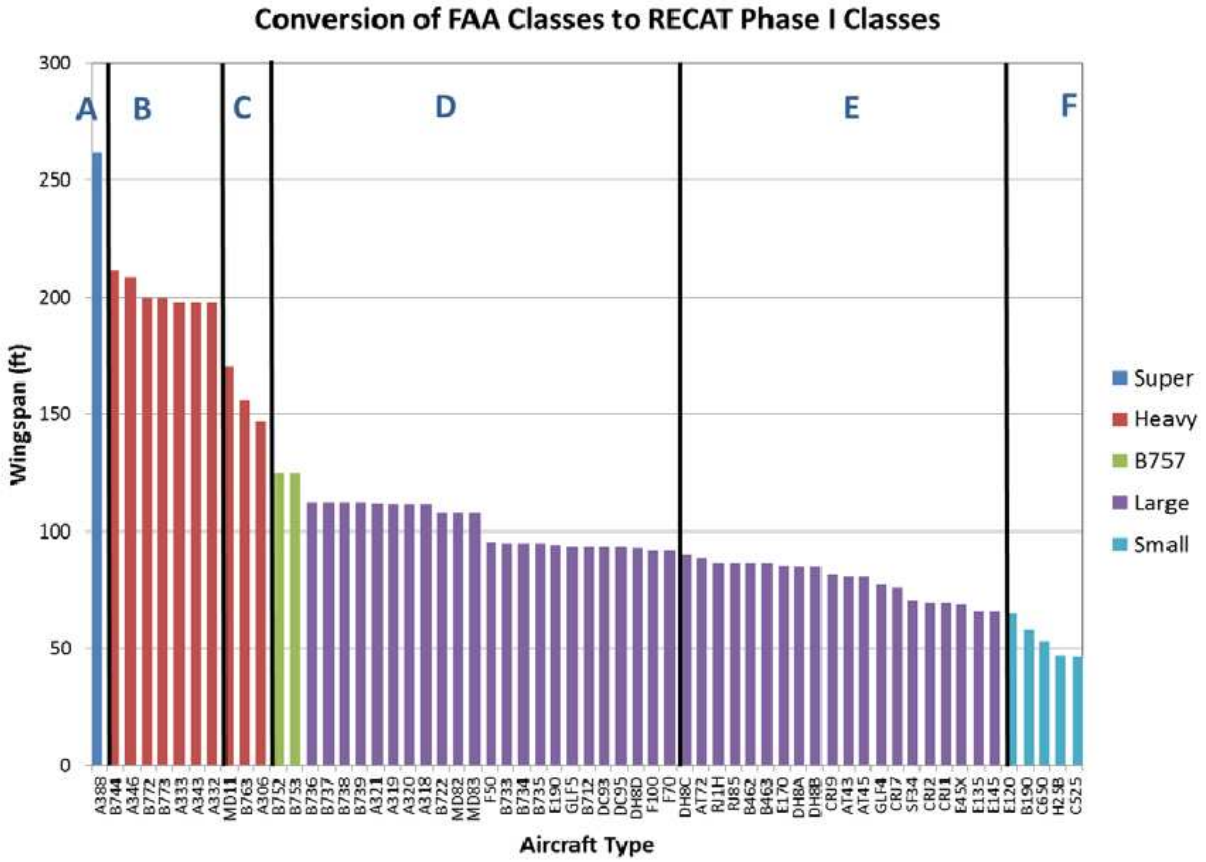

(a)

RECAT Separation Matrix

Leader \ Follower	A	B	C	D	E	F
A	MRS	5.0	6.0	7.0	7.0	8.0
B	MRS	3.0	4.0	5.0	5.0	7.0
C	MRS	MRS	MRS	3.5	3.5	6.0
D	MRS	MRS	MRS	MRS	MRS	5.0
E	MRS	MRS	MRS	MRS	MRS	4.0
F	MRS	MRS	MRS	MRS	MRS	MRS

(b)

Abbildung 1.2.: (a) Six new aircraft type dependent wake categories, (b) RECAT 1 separation standards, increased (green), remained (white) and decreased (blue) separations in nautical miles (Lang & Lunsford, 2013).

landing. In addition, long-term LIDAR measurements at Charles de Gaulle airport show that wake vortices frequently remain close to the runway, in 3% of the landings wake vortices get even closer than 25 m to the following aircraft (Holzäpfel et al., 2011). However, much less critical encounters are observed than one should expect from these measurements, as well as from predictions of WVAS. The state of knowledge in wake vortex physics and simulations does not explain the observations at airports. This mismatch may be resolved by a thorough investigation of the landing phase as well as the touchdown process. So called end effects, occurring at touchdown, have to be studied, in particular their evolution and contribution to wake-vortex decay has to be quantified. For this purpose a new numerical approach has to be developed. Recent developments, coupling Reynolds-averaged Navier-Stokes (RANS) and large-eddy simulations (LES) provide an innovative methodology to simulate an aircraft, flying through a ground fixed domain, generating a realistic wake (Misaka et al., 2013). For this purpose a high-fidelity RANS flow field is swept through a LES domain. This way a spatial development of the aircraft wake is integrated in a large-eddy simulation. The approach is extended to simulate the aircraft landing and study the physics of the related wake-vortex decay, see Fig. 1.3 (a). End effects are indeed identified as a potential reason for the surprisingly save aircraft landings. End effect is a term that originated in towing tank facilities denoting the vortex bursting phenomenon when a model aircraft stops (Bao & Vollmers, 2005; Ortega et al., 2002). The vortex characteristics change abruptly, disturbances occur and propagate against the towing direction (Moet et al., 2005). Similar effects occur when an aircraft touches down at the runway[1]. The vortex circulation is rapidly reduced leading to a similar disturbance of the vortex, this is why we call these effects also end effects. End effects should be included in an optimal WVAS.

- Can the wake-vortex decay in ground proximity be artificially enhanced?

There is a strong appeal for artificial devices for destruction of wake vortices, or at least for weakening them to an uncritical level. There have been numerous attempts to accelerate vortex decay deliberately out of ground proximity (Breitsamter, 2011). However, much less work has been done for acceleration of wake-vortex decay in ground proximity. A device for active wake-vortex decay acceleration should be reasonably priced, save, and effective, ideally permitting an aircraft separation reduction to radar separation, provided that a WVAS guarantees that the glide path is void of wake vortices. A patent entitled "Surface Structure on a Ground Surface for Accelerating Decay of Wake Turbulence in the Short Final of an Approach to a Runway" has been filed by Frank Holzäpfel[2], aiming at wake-vortex decay enhancement. This novel method to accelerate vortex decay, exploiting fundamental properties of vortex dynamics, is investigated in this thesis. Vortex decay can be initiated locally and accelerated in the vicinity with dedicated obstacles, like plate lines, installed at the ground, see Fig.1.3 (c), (d). To put it simply, the obstacle causes the flow to redirect the force, that normally causes the wake vortices above the obstacle to rebound, into early turbulent vortex decay. It is found that a plate line may enforce the wake-vortex

[1] http://www.youtube.com/watch?v=PpUftG_mxg8
[2] patent number DE 10 2011 010 147 (2011)

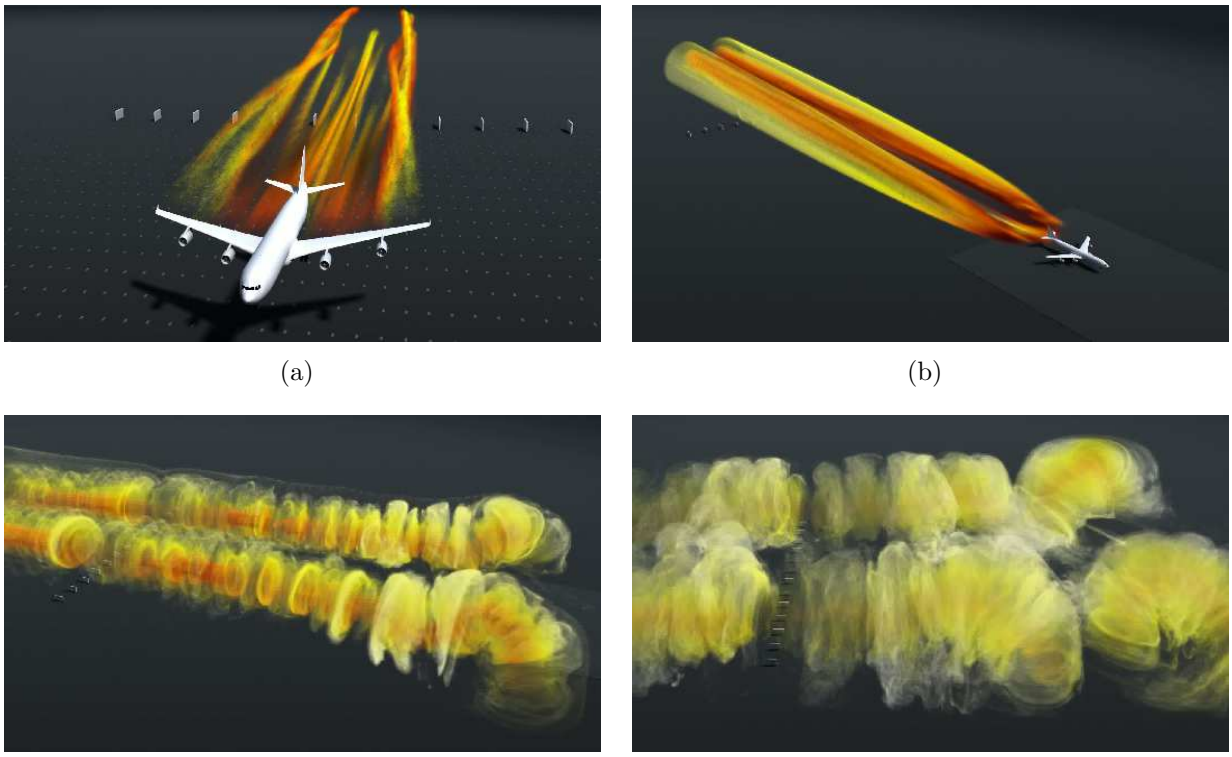

(a) (b)

(c) (d)

Abbildung 1.3.: Spatial LES of landing, plate line effect (a) final approach, tracer initialized inside the wake vortex (b)-(d) touchdown and vortex decay, tracer initialized behind the aircraft wing, velocity of the tracer color coded, high velocities red, low velocities white.

Abbildung 1.4.: Plate line consisting of six plates with dimensions 2.2 m ×4 m displaced by 10 m designed for the dimensions of the HALO research aircraft (G550, photo Marc Malycha, DLR).

decay by more than 20% of the initial circulation, at separationally relevant vortex ages. The suggested ground-based and passive method requires relatively small technical effort to be tested and be introduced at airports.

- Can the numerical findings be confirmed by measurement data?

The numerical investigations have been complemented by experiments in the DLR water towing tank in Göttingen, termed Wasser Schleppkanal Göttingen (WSG). These results are used to confirm the effect of obstacles at the ground. The experimental setting is modeled in the simulations to enable comparability. The experimentally obtained trajectories and decay characteristics are qualitatively reproduced by the simulations. Field measurement campaigns have been conducted at Munich airport during the WakeMUC campaign between 11 March and 12 May 2011, where 779 aircraft landings have been investigated, as well as at special airport Oberpfaffenhofen during the WakeOP campaign, on 29 and 30 of April 2013. At Oberpfaffenhofen the DLR research aircraft HALO, a Gulfstream G550, demonstrated during 72 overflights the functionality of the plate line, see Fig. 1.4. WakeMUC results are used for an assessment of the LES of wake-vortex evolution after landing without dedicated obstacles.

1.3. State-of-the-art - Recent Developments

Various review articles reflect the earlier and recent research work and list important questions in the area of the wake vortex issue (Spalart, 1998; Rossow, 1999; Gerz et al., 2002; Breitsamter, 2011). Fundamental physics is addressed therein, regarding vortex modeling, instabilities and non-linear effects. This thesis contributes to two major directions of research, aiming at reducing aircraft separations and increasing safety.

1. **Wake-vortex prediction.** For a given aircraft type, the atmospheric parameters. predictions of the wake vortex positions and strengths can be done in WVAS ideally in a probabilistic sense (Proctor, 1998; Robins et al., 2001; Rossow, 2002; Holzäpfel, 2003; Holzäpfel & Robins, 2004).

2. **Wake-vortex alleviation and decay enhancement.** Active or passive modifications at the aircraft have been tested in wind tunnel or towing tank facilities (Coustols et al., 2003; Breitsamter, 2011), in numerical simulations (Stumpf, 2005), and in real flight in the European project AWIATOR. Early ideas to promote wake-vortex decay in ground proximity applying jet blast, water fountains or trees have not been further pursued. Respective patents have been filed by F. Bao[3] and A. Schröder and R. Konrath[4].

A large variety of wake-vortex studies is based on numerical simulations of the flow field. A landing aircraft generates a flow field, which is highly complex in terms of structure and relevant scales. This includes the flow around an aircraft's main wing, fuselage, slat, flap, landing gear, jet engine, and tail plain, as well as the interaction with the approaching ground, and the crucial final lift reduction during touchdown that controls the strength of the generated wake vortices. An accurate computation of the complete wake of an aircraft configuration, from generation to decay, at realistic Reynolds numbers ($\mathrm{Re}_c \approx 10^7$), with either LES or RANS exceeds the available capabilities of supercomputers by far. The flow around the aircraft, the roll-up process, the development in the far-field, and the decay are mostly treated as separate problems. Today's challenge is to find appropriate models to bridge near-field and far-field without loss of important flow details.

Usually RANS simulations are used for the flow around the aircraft and the subsequent roll-up process of the wake in the jet regime (Labbe et al., 2001; Stumpf, 2005). On the other hand the dynamics of rolled-up wake vortices until decay have been studied by large-eddy simulations (LES), considering various atmospheric conditions, turbulence, thermal stability, and wind shear (Marshall & Beninati, 2005; Holzäpfel et al., 2001; Misaka et al., 2012b). Those studies, out of ground proximity, initialize a vortex pair with a longitudinally constant velocity profile (temporal LES), optionally superimposed by ambient turbulence. Misaka et al. (2012a, 2013) demonstrates the feasibility of a wake initialization approach where a realistic aircraft wake was generated in a LES domain (spatial LES). The wake evolution was studied from roll-up to decay bridging the near-field to the far-field. Using

[3]patent number DE 10 2005 025 004 A1 (2005)
[4]patent number DE 10 2008 054 107 B3 (2008)

this method it is possible to study the complete vortex development at cruise altitudes. The present thesis further develops the technique from Misaka et al. (2013) applying it to aircraft landings.

In contrast to the flow field close to the touch down zone, the interaction of fully rolled-up vortices with the ground is quite well understood. When counter-rotating vortices approach a flat surface or are generated at low altitude they diverge. An outboard directed flow is induced by the vortices on the surface and vorticity of opposite sign is produced in a boundary layer (Harvey & Perry, 1971). The induced flow near the surface experiences an adverse pressure gradient, which is strong enough to cause flow separation, leading to the formation of a separation bubble at the ground. Flow simulations have shown how pairs of secondary vortices are produced from the separation region, detach and interact with the primary vortices (Proctor et al., 2000; Spalart et al., 2001; Dufresne et al., 2005). The presence of an ambient crosswind induces another boundary layer corresponding to a vorticity layer at the ground. In contrast to considerations without crosswind, this causes an asymmetric situation. The sudden eruption of wake vortex induced wall vorticity is faster and more intense for the downwind vortex, where the crosswind shear generated vorticity and the secondary vorticity have the same sign, but is attenuated for the upwind vortex.

The interaction of a counter-rotating two-vortex system with a flat surface, using numerical simulations, has been investigated so far with different approaches, which either resolve or model the wall, i.e. wall-resolved direct numerical simulations (DNS) (Duponcheel et al., 2006) or LES (Georges et al., 2005). However, the resolution requirements for the boundary layer flow limit the Reynolds number, not only in DNS but also in LES. In LES the subgrid-scale model only works properly, if the modeled part of the flow contributes to a relatively small extent of the turbulent kinetic energy (TKE). Close to walls, small structures mainly account for the TKE, such that the resolution close to walls has to be refined in LES as well as in DNS. Up to now, values of $\mathrm{Re}_\Gamma = \Gamma/\nu$ on the order of 20 000 have been realized for wall resolved LES for vortex flow (Georges et al., 2005). This approach allows the investigation of coherent structures close to the wall at the expense of a relatively low Re_Γ.

Methods for wake vortex decay enhancement can be divided into passive or active methods, airborne or ground based. In projects funded by the European Commission such as C-Wake, FAR-Wake and AWIATOR, methods have been presented that modify the wing loading to trigger inherent vortex instabilities (Coustols et al., 2003; Stumpf, 2005). The development of suitable devices requires comprehensive theoretical, numerical and experimental effort to prove the efficiency. Suitable methods shall not degrade the flight properties and performance. In addition they shall not decrease safety. The airborne methods aim at triggering intrinsic instabilities like Crow or Crouch instabilities to accelerate the natural decay process. Several passive modifications of the wing configuration have been proposed by Ortega et al. (2002); Coustols et al. (2003) but also active ones like Crouch et al. (2001). Special four-vortex system topologies to trigger instabilities have been studied numerically (Fabre et al., 2002). There, decay acceleration is achieved by introducing obstacles at the ground, to trigger the turbulent interaction of primary and secondary vortices. This ap-

proach falls into the category of a passive ground-based method. A theoretical investigation of the interaction of anti-parallel vortices of different strength was performed by Marshall et al. (2001). Aircraft landing has been tackled with different approaches. Early theoretical investigations of Wieselsberger (1922) capture the steady wing-in-ground effect[5] (WIG), describing the phenomena very close to ground. More detailed, Daeninck et al. (2006) investigate the ground effect for different wing configurations. From the flight system identification approach, Fischenberg (1999) incorporates real flight data and models relevant quantities. However, many questions related to the touchdown still have to be investigated. Bao & Vollmers (2005) investigated end effects occurring as unintended artifacts when an aircraft model in a towing tank stops.

Different experimental methods are used to study wake vortex behavior. With wind tunnels, catapult facilities and water towing tanks deep insights into the the near field and extended near field have been obtained. A large number of purely experimental or numerical investigations of wake vortices was published, however combinations and comparisons of experimental and simulation results are quite rare. Towing tank experiments are widely used for the investigation of spatially evolving wakes (Hünecke, 2001; De Gregorio & Ragni, 2003). Turbulent vortex decay has been investigated in Delisi (2006). The ground effect has been studied in Cottin et al. (2007); Konrath et al. (2008). Various visualization and analysis techniques are developed like Laser Induced Fluorescence or Particle Image Velocimetry (PIV), respectively. Especially the development of three-dimensional tomographic PIV methods presented in Konrath et al. (2013) introduces a wide range of applications in experimental fluid dynamics. The combination of LES and towing tank experiments provides an assessment of both, the experimental and numerical methods. However, this approach is particularly limited by the Reynolds number. The applicability of the described effects to reality has to be proven by field experiments. Mostly wake vortex measurements are performed using a LIDAR technology (Harris et al., 2000). Measurements for real aircraft landings have also been performed in (Holzäpfel & Steen, 2007). Though comparisons of flight experiments and simulations in cruise altitudes have shown good agreement (Lewellen et al., 1998), comparisons in ground proximity still have to be performed.

Beside general theoretical considerations and the investigation of flight measurement data, the main instruments of wake vortex investigation in this thesis are LES and hybrid RANS/LES simulations. These simulation methods are appropriate models for solving the Navier-Stokes equations with large areas of locally homogeneous space. The LES enables to treat flow separations at the ground surface in a straight forward way, compared to other methods like so-called *vortex methods* (Winckelmans et al., 2005; De Visscher et al., 2013). LES investigations of vortices in ground proximity (Proctor et al., 2000; Dufresne et al., 2005) did not capture the effects of flare, touchdown and an angle of approach so far, as they assume fully rolled-up vortices interacting with the ground. With the hybrid RANS/LES approach we are able to resolve these shortcomings. The whole landing phase

[5]The term "wing-in-ground effect" captures all effects that a wing experiences in the proximity of a ground surface.

is investigated in this thesis with a set of LES of different levels of complexity. This way we try to separate and highlight the physical effects, that are important in vortex evolution. Generally speaking, the effects of flare, touchdown and angle of approach requires more complexity in numerical treatment, than the simulation apart from the touchdown zone, where several assumptions on the vortices are valid. The proposed method of wake-vortex decay enhancement with obstacles like plate lines at the ground is mainly investigated with wall-resolved LES and fully rolled-up vortices. This way we can elaborate and elucidate the vortex dynamics excluding effects like turbulence, angel of approach, etc. The direct comparison of simulation methods with experimental methods like towing tank experiments and field measurement campaigns is very rare in the wake vortex field. Towing tank experiments present a completely different method with a Reynolds number comparable to wall-resolved LES. However, the initialization technique of the wake is different, therefore we can better understand the sensitivity of the vortex roll-up. Field measurements are as close to reality as possible in terms of Reynolds number and setup. However, the measuring technique is quite expensive and processing algorithms are relatively new and still developing.

Results of the thesis have partly been published in conference proceedings or peer reviewed journals. The method of artificial enhancement of wake-vortex decay in ground proximity was firstly presented in Stephan et al. (2012). This work includes an investigation of aircraft wake-vortex decay mechanisms in ground proximity employing wall-resolved LES. The temporal approach for modeling the landing phase was used there. Most of these results have then been published in Stephan et al. (2013a). A comparison of experiments and simulations dealing with the effect of ground obstacles on wake-vortex decay was published in (Stephan et al., 2013c). An approach towards realistic simulation of wake-vortex evolution during landing extending the methodology of Misaka et al. (2013) was presented in Stephan et al. (2013b) and is submitted to a journal in more detail (Stephan et al., 2014). The master thesis "Numerical Simulation of Wind Impact on Transport and Decay of Wake Vortices of Landing Aircraft" (Tchipev, 2013), closely related to this thesis, was supervised in the course of the work.

1.4. Overview over the Thesis

Chapter 2 describes the analytical, numerical, and experimental methods, relevant for the investigation of the landing aircraft's wake. First, wake-vortex physics and flight physics in the proximity of ground are introduced. The origin of wake vortices is described and phases of wake-vortex decay, during the different phases of landing, are characterized. Flight test data is presented, complementing the theoretical concepts. Basic properties of ambient turbulence, relevant for the thesis, is recapitulated. The LES code MGLET is introduced, covering the most important numerical features. Models for the treatment of the wall and obstacles, that are employed in the present study, are described and the RANS/LES coupling is introduced. Particular developments necessary for the landing phase are highlighted. Finally the numerical settings, the pre-simulations of ambient turbulence, and the applied

post-processing algorithms are detailed.

Chapter 3 presents the LES results. First, an overview over all simulations, included in the thesis, are listed. Then, we start with general features of the flow field of the complete landing process, later the effects of crosswind and obstacles are discussed. We proceed with a detailed investigation of wake vortex evolution and decay above flat ground, sufficiently separated from the touchdown zone. The effect of obstacles is quantified and the related vortex physics is analyzed. The concept of a plate line, as a particularly effective obstacle configuration, is presented including a discussion of headwind effects. The wing-in-ground effect, occurring during flare, is analyzed from the viewpoint of LES. Touchdown effects are described and the complex vortex topology, during the decay phase, is presented. Finally we quantify vortex decay and the development of core radii, depending on the distance to the touchdown point, and how this is affected by the plate lines.

Chapter 4 serves as a comparison with various measurements. The experiments serve as an assessment for numerical simulations, whereas the simulations provide a complementary view at wake vortex phenomena. First, we compare LES with water towing tank experiments. The general flow field obtained by LES and vortex visualizations are compared, complemented by qualitative and quantitative comparisons of vortex trajectories and decay. Finally, the propagation of obstacle disturbances, as well as the effect of two obstacles, are discussed. A detailed comparison with data from the field measurement campaign WakeMUC is performed.

Chapter 5 sums up the results, highlighting the answered and newly emerged questions, followed by a short outlook to possible future work.

2. Methods

2.1. Wake-Vortex Principles

The mathematical treatment of incompressible fluid dynamics is based on conservation laws for momentum and mass (e.g. Kundu & Cohen, 1990)

$$\frac{\partial u_i}{\partial t} + \frac{\partial (u_i u_j)}{\partial x_j} = -\frac{1}{\rho}\frac{\partial p}{\partial x_i} + \nu_{\mathrm{mol}}\frac{\partial^2 u_i}{\partial x_j^2} \tag{2.1}$$

$$\frac{\partial u_j}{\partial x_j} = 0 \tag{2.2}$$

Here u_i represent the cell averaged velocity components in three spatial directions ($i, j = 1, 2,$ or 3). The summation convention is used for the velocity components. p denotes the pressure and ρ the density of the fluid. A density of $\rho = 1.2\,\mathrm{kg}\,/\,\mathrm{m}^3$ is employed all over the thesis. The coordinates x_1, x_2, x_3 also denoted by x, y, z correspond to axial, lateral and vertical directions, respectively. Buoyancy effects of temperature in the boundary layer are not taken into account.

The curl of the velocity is called the vorticity $\vec{\omega} = \nabla \times \vec{u}$. Under favorable conditions, that we can assume to be valid in our applications, the inversion is possible and $\vec{u}$ is determined uniquely by $\vec{\omega}$ (Saffman, 1992). By the Helmholtz decomposition theorem $\vec{u}$ can be uniquely expressed by the sum of a solenoidal an irrotational potential component:

$$\vec{u}(\vec{x}, t) = \vec{u}_v(\vec{x}, t) + \nabla\Phi, \tag{2.3}$$

where

$$\vec{u}_v(\vec{x}, t) = \frac{1}{4\pi}\int \vec{\omega}(\vec{x}', t) \times \nabla\frac{1}{|\vec{x}' - \vec{x}|}d\vec{x}'. \tag{2.4}$$

The irrotational, solenoidal field $\nabla\Phi$ can be added to satisfy a single boundary condition. Hence, for a given vorticity distribution and boundary conditions the velocity field is determined uniquely. Therefore we will speak of a velocity field "induced by" a certain vorticity distribution all over the thesis, though it might conflict with the understanding that only pressure and shear forces act upon the fluid.

2.1.1. Wake-vortex and lift generation of an aircraft

As an unavoidable consequence of lift generation by aircraft wings of finite span, vortex sheets shed off the wings, roll up and form a pair of counter-rotating vortices. They are

(a) $\Gamma = 0$ (b) $\Gamma = \Gamma_{\text{Kutta}}$

Abbildung 2.1.: Flow around an airfoil of an ideal fluid (a) no circulation and (b) flow separation at the trailing edge and resulting circulation (Kundu & Cohen, 1990).

called wing-tip vortices, trailing vortices or wake vortices. The first investigations of wake-vortex generation and the fundamental relation to the aircraft's lift have been performed in the early 20th century by Lanchester (1907) and Prandtl (1918, 1919).

The lift force acts on a flying aircraft due to the circulation of air around the wings[1], which is defined by

$$\Gamma \equiv \oint_{\partial A} \vec{u} \cdot d\vec{s} = \int_A \vec{\omega} \cdot d\vec{A} \qquad \text{(Stokes-Theorem)}. \tag{2.5}$$

The flow pattern around an aircraft's wing for two different values of clockwise circulation, as possible solutions for an ideal fluid, are depicted schematically in Fig. 2.1. For $\Gamma = 0$, Fig. 2.1 (a), the stagnation points at the leading edge and trailing edge are located such that the circulation around the wing is zero. No lift is generated in that case. Practically fluid may not flow around the sharp trailing edge against the direction of the incoming flow, see Fig. 2.1 (b). The flow separates at the trailing edge leading to a circulation around the aircraft wing called *Kutta condition*. The lift force L experienced by a wing with circulation Γ moving with the speed U can be computed by the famous Kutta-Joukovsky lift theorem, see Eq. (2.7). Hypothetically the circulation around the wing is represented by a vortex filament, the so-called bound vortex.

The wing develops a pressure difference between the lower pressure side and the upper suction side. A wing of finite wing span accelerates fluid in spanwise directions which sheds off and rolls up. As a consequence a vorticity sheet continuously detaches from the wing and rolls up to generate the trailing vortices, see Fig. 2.2. The circulation around the wing $\Gamma(y)$ at a spanwise position y decreases from the center (root) towards the tips, due to vortex shedding, from Γ_0 to zero. The effect of an airfoil on a uniform stream is similar to that created by a vortex. Therefore the wing is modeled by a vortex, the co-called bound vortex. Prandtl (1919) introduces the notion of a lifting line as the vortex filament center line describing the bound vortex strength by a circulation distribution $\Gamma(y)$ decreasing from the wing's root towards the tips.[2]

[1]The definition of a vortex force can be found in Saffman (1992).

[2]All over the thesis the term vortex strength is synonymously used for vortex circulation.

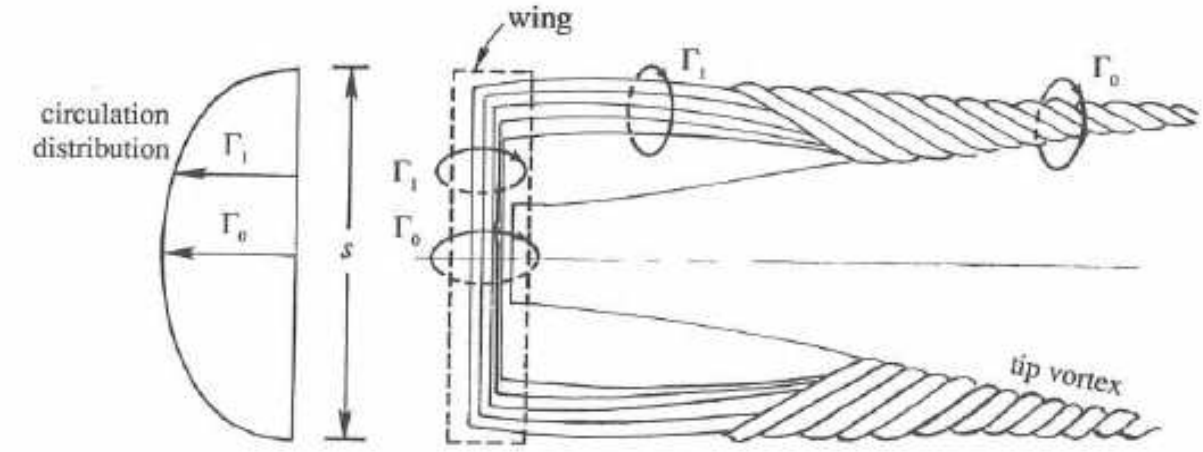

Abbildung 2.2.: Circulation distribution on a wing and roll-up of trailling vortices. The flow around the airfoil is modeled by a bound vortex with a circulation distribution $\Gamma(y)$, the so-called lifting line (Kundu & Cohen, 1990).

The near-field as well as the far-field of the aircraft's wake strongly depend on the strength of the shedding vortex sheets, and thus on the circulation distribution along the lifting line. The downward velocity induced by the entire vortex sheet on the lifting line $w(y)$ is called *downwash*. In theory an elliptical circulation distribution of the form

$$\Gamma(y) = \Gamma_0 \left[1 - \left(\frac{2y}{b}\right)^2\right]^{1/2} \tag{2.6}$$

is frequently used, where Γ_0 denotes the root circulation and b the wingspan. However, the high lift wing configuration of a landing aircraft deviates substantially from the theoretical distribution (Breitsamter, 2007, p.15). Particularly the deployed flaps lead to a shedding of a large part of the circulation along the wing. See Daeninck et al. (2006) for span loading distributions modeling high lift configurations. Two main vortices, the flap-tip and the wing-tip vortex constitute, rotating around each other and merging in the far-field.

A vortex like an airfoil placed in a uniform stream experiences a so-called vortex force (Saffman, 1992). This differential and total lift force on a wing can be computed from the circulation distribution and the aircraft speed U by the Kutta-Joukovsky lift theorem (Kundu & Cohen, 1990)

$$dL = \rho U \Gamma(y) dy, \quad L = \int_{-b/2}^{b/2} \rho U \Gamma dy. \tag{2.7}$$

Assuming a balance of the lift and weight force $L = Mg$, we obtain an expression for Γ_0

$$\Gamma_0 = \frac{Mg}{\rho b_0 U}, \quad \text{with} \quad b_0 = \int_{-b/2}^{b/2} \frac{\Gamma(y)}{\Gamma_0} dy, \tag{2.8}$$

where M denotes the aircraft mass. The ratio $s = b_0/b$ is called the load factor. For an elliptic circulation distribution the load factor can be computed to $s = \pi/4$. (A constant $\Gamma(y) = \Gamma_0$ and a triangular circulation distribution $\Gamma(y) = \Gamma_0(1 - 2|y|/b)$ yield $s = 1$ and $s = 1/2$, respectively.) According to Kelvin's circulation theorem, stating that the circulation around a material circuit in an ideal fluid is an invariant of the motion, the circulation of the completely rolled-up wake vortices equals approximately Γ_0. The vortex separation turns out to be exactly b_0. The complete flow consisting of the bound vortex and the free wake-vortices is sometimes called horse shoe vortex (Schlichting & Truckenbrodt, 1967). The vortex Reynolds number Re_Γ is defined as $\mathrm{Re}_\Gamma = \Gamma_0/\nu$.

The total lift coefficient is defined as

$$C_L = \frac{L}{\frac{1}{2}\rho U^2 A} = \frac{L}{\frac{1}{2}\rho U^2}\frac{\Lambda}{b^2}, \tag{2.9}$$

where A denotes the wing plan-form area, and $\Lambda = b^2/A$ the aspect ratio. With Eq. (2.8) this yields

$$C_L = \frac{2\Gamma_0 s\Lambda}{Ub}, \tag{2.10}$$

as an expression connecting the wake-vortex strength, flight speed and lift coefficient. The drag force D induced by the wake vortices is called *induced drag*, see Kundu & Cohen (1990). The rate of generation of kinetic energy of the wake vortices equals the rate of work done against the induced drag DU. The induced drag is also called the *vortex drag* analogously to the *wave drag* experienced by a ship. The drag coefficient C_D is defined by

$$C_D = \frac{D}{\frac{1}{2}\rho U^2 A}. \tag{2.11}$$

2.1.2. Wing in ground effect

In ground proximity the presence of a fixed surface significantly modifies the aerodynamics. The first investigations on ground effect have been performed by Wieselsberger (1922); Prandtl (1923) employing a simple model based on Prandtl's lifting line theory. Here the steady case is investigated, assuming a fixed wing speed as well as angle of attack.

Close to the ground the downward flow is limited by the rigid ground surface. This results in a number of physical phenomena arising at moving aircraft in proximity of the ground summarized as ground effect. The effect appears, in general, for wing altitudes lower than a wing span above ground. It has a crucial impact on the aircraft landing. The main phenomena resulting from the ground effect are (Etkin, 1972).

1. the pressure below the wings increases as the aircraft approaches
2. the sink rate is reduced
3. reduced downwash angle at the tail

4. increase in the lift curve

5. reduction in the induced drag

An overview over various analytical approaches to quantify the wing-in-ground effect (WIG) can be found in Pistolesi (1937). Solutions for two- and three-dimensional wings in ground effect may be found in Widnall & Barrows (1970). An overview of the ground effect from the system identification approach can be found in Jategaonkar (2006). In the systemic approach analytical models for lift and drag coefficients in ground effect are considered (Fischenberg, 1999). Parameters in the models are identified using flight test data and validated in simulations.

Daeninck et al. (2006) investigate wake vortex roll-up in ground effect for different wing aspect ratios and span loading at different altitudes above the ground. A double elliptical chord distribution as a model for high lift configuration is also studied. The steady wing in ground effect is modeled using Prandtl's lifting line theory. A mirror lifting line of opposite strength is positioned below the ground. This way a free-slip condition is realized at the ground surface. The local circulation is then related to the local downwash, which is modified by the mirror lifting line. Depending on the altitude local circulation distributions are derived. Daeninck et al. (2006) conclude that the ground proximity has a minor effect on the span loading, even negligible for $h/b > 1$, where h denotes the wing altitude. It becomes important at $h/b < 0.25$. The total lift increases slightly. The root circulation Γ_0 and consequently the circulation of the wake vortex increases by 10% at $h/b < 0.125$. The strongest effect relates to the reduction of the induced drag. Overall the wake-vortex circulation moderately increases in ground proximity.

Note that these investigations assume a fixed angle of attack, flight speed and position above the ground. However, during landing all these parameters change, as we will see in the sequel. The interesting question, how the wake vortex strength changes in ground proximity can therefore not be fully addressed by stationary considerations.

2.1.3. Phases of wake-vortex evolution

Typically the evolution of the commercial aircraft's wake is divided into several phases, see Breitsamter (2007). In cruise flight these phases depend on the distance to the aircraft or equivalently on the time after the aircraft passage. Four evolution phases are commonly distinguished, see Fig. 2.3

i) Near field. This phase includes the shedding of the vorticity sheet and roll-up of the main vortex structures and extends from the aircraft wings to the rear fuselage. Particularly in high lift configuration it constitutes highly complex vorticity structures. In addition to the wing-tip vortices, strong flap-tip vortices roll up at the outer edge of the flap, see Misaka et al. (2013). Other vortices from the engine pylons and the wing-fuselage junction are clearly separated.

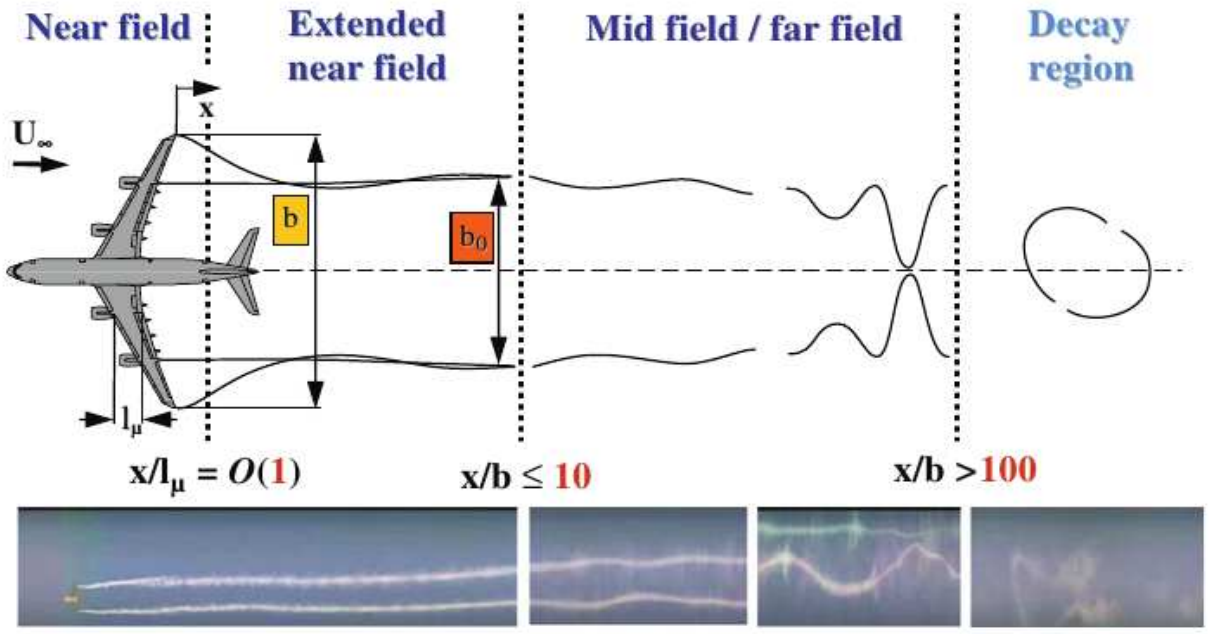

Abbildung 2.3.: Phases of wake-vortex evolution in cruise flight, Breitsamter (2011).

ii) Roll-up phase, extended near field. In clean configuration the roll-up is finished very fast (Misaka et al., 2012a). However, in high lift configuration this phase can be much extended. Here the strong co-rotating wing-tip and flap-tip vortices merge. At the end, the complete circulation, equal to the maximum circulation of the bound vortex, has concentrated in a pair of counter rotating vortices. This phase is extended up to ten aircraft wingspans.

iii) Vortex phase, mid field/far field. The rolled-up vortex pair mutually induces a descent velocity. Depending on the atmospheric conditions and true airspeed this phase can extend up to more than 100 wingspans during cruise. In ground proximity the vortices are subjected to a complex interaction with the ground surface.

iv) Decay phase. Due to atmospheric influences instabilities appear. Initial perturbations result in sinusoidal vortex center lines with increasing amplitude in time, the so-called Crow instability (Crow, 1970). In cruise conditions the vortices link. Additionally a turbulent environment accelerates the vortex decay which has been investigated in Lewellen et al. (1998).

In cruise flight, the flow around the aircraft can be considered as approximately stationary. Under approximately constant environmental conditions, these four phases develop in time and space at every distinct distance behind the aircraft uniformly shifted by the aircraft flight speed. During landing this significantly changes. Depending on the altitude

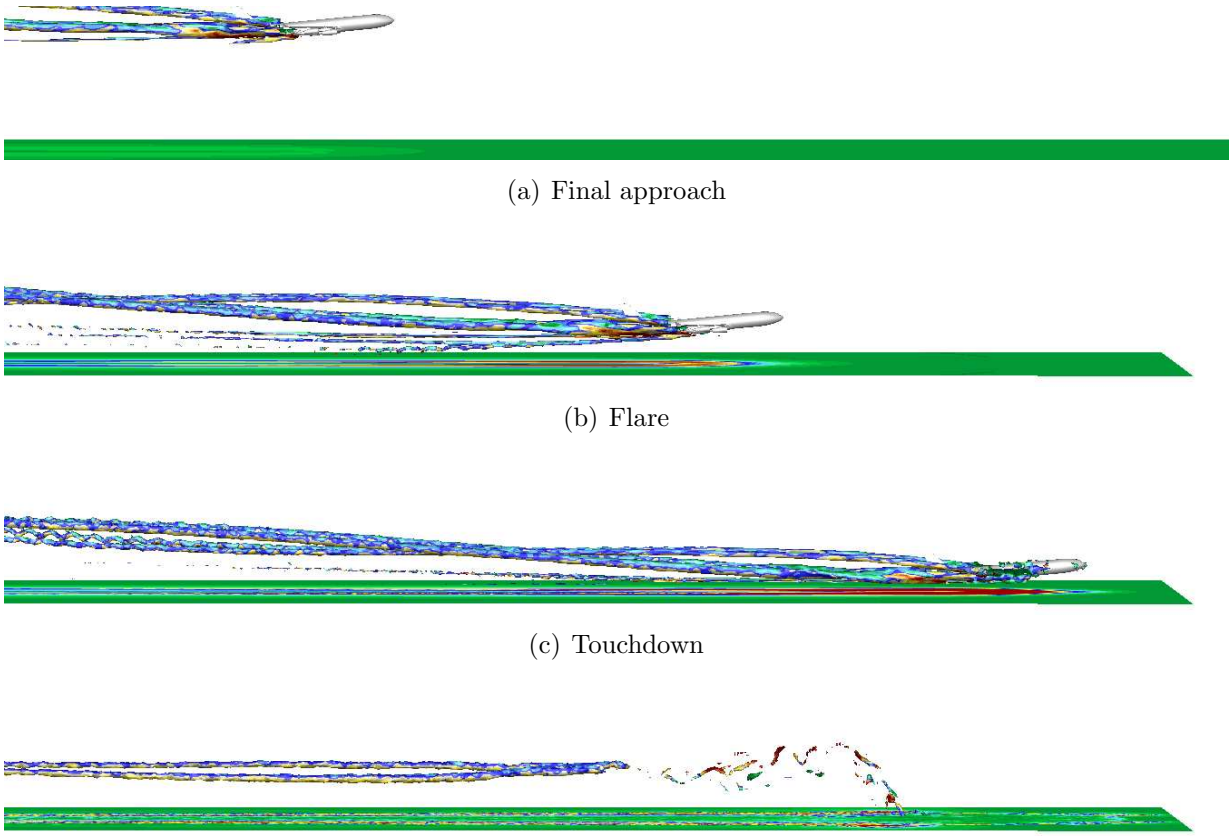

(a) Final approach

(b) Flare

(c) Touchdown

(d) Roll out

Abbildung 2.4.: Schematic of landing phases.

above ground the decay phases are accelerated.

2.1.4. Landing phases

During landing four different phases of the aircraft state are distinguished in practice [3] which are used in the thesis to characterize the aircraft landing.

i) Final approach. During the final approach the wings are in high-lift configuration, the flaps and slats are deployed. The aircraft has a constant sink rate as well as speed. The wing-in-ground effect can be neglected due to a relatively high altitude above the ground. Fig. 2.4 (a) depicts the final approach. The shear layer at the ground is relatively weak.

[3] http://www.skybrary.aero/index.php/Landing_Flare?utm_source=SKYbrary&utm_campaign=47ff8e1e92-SKYbrary_Highlight_04_07_2013&utm_medium=email&utm_term=0_e405169b04-47ff8e1e92-264071565 date:13. März 2014

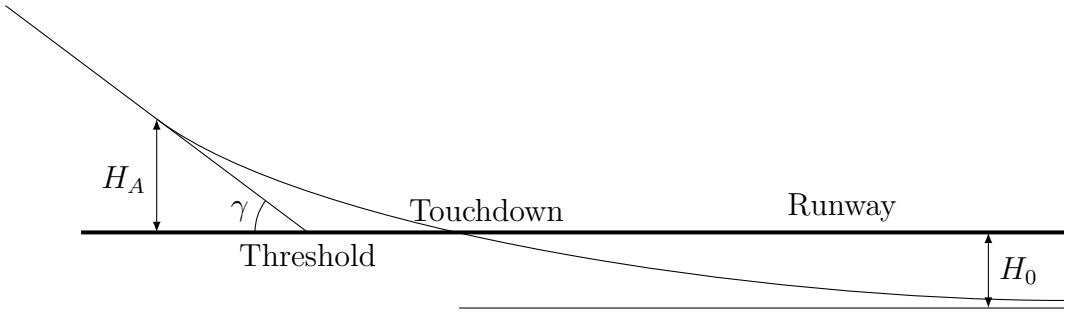

Abbildung 2.5.: Schematic of the flare trajectory of a aircraft landing, not in scale.

ii) Flare. The landing flare is a transition phase between the final approach and touchdown at the runway. The wing-in-ground effect increases. Normally this phase includes a simultaneous increase in the aircraft pitch angle and a reduction in engine thrust. The sink rate reduces as well as the aircraft speed. The flare phase starts at a height of approximately b_0. The shear layer at the ground surface is shown in Fig. 2.4 (b). During the flare the descent angle is reduced. The flare trajectory during *Cat.III* landings of commercial aircraft is determined by the autopilot (Hecker, 2006). The flare out starts at an altitude $H_A \approx 25\,\mathrm{m}$, see Fig. 2.5. The flare trajectory is described by an exponential function starting at H_A. The virtual touchdown level with $\dot{H} = 0\,\mathrm{m/s}$ lies $H_0 \approx 2\,\mathrm{m}$ below the runway. At the point of touchdown a descent speed of $-0.6\,\mathrm{m/s}$ is achieved. The flight trajectory can be expressed as

$$H = (H_A + H_0) \cdot e^{-\frac{t}{T}} - H_0 \tag{2.12}$$

$$\dot{H} = -(H_A + H_0) \cdot \frac{1}{T} \cdot e^{-\frac{t}{T}}, \tag{2.13}$$

with $T = (H_A + H_0)/U$. In the phase space the autopilot trajectory is depicted in Fig. 2.6. During flare the ratio of $\dot{H}$ and H equals

$$\frac{\dot{H}}{H} = -\frac{1}{T}. \tag{2.14}$$

In reality the flare trajectory strongly depends on the aircraft type. Huge aircraft like aircraft carriers do not vary the rate of descent until touchdown (red line in Fig. 2.6), the landing gear design must be robust enough. At the other end of the spectrum are landings of light aircraft, the flare trajectory of the *Royal Aircraft Establishment* (REA) proposed a constantly lower sink rate (green line in Fig. 2.6).

iii) Touchdown. The touchdown starts with the first contact of the main landing gear with the runway followed by immediate de-rotation of the aircraft and the attachment of the front landing gear. During this time interval the total lift is strongly reduced. Figure 2.4 (c) shows schematically the instant of contact of the main landing gear with the runway from LES simulation.

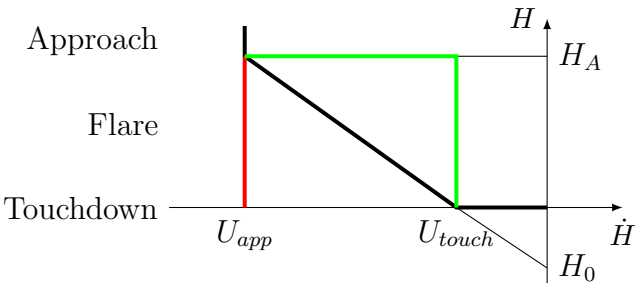

Abbildung 2.6.: Altitude during aircraft landing in phase space, autopilot (black), RAE (green), LES (red).

iv) Roll out and deceleration. After touchdown the reverse thrust sets in, ground spoilers are deflected, wheel brakes are applied, and the aircraft decelerates. Though a very weak wake vortex can be assumed in this phase of the landing due to a non-zero lift force acting on a horizontal wing we can neglect it and assume zero mean vertical velocities in the aircraft wake.

As a result of this thesis, the dependency of the wake vortex evolution phases on the landing phases can be analyzed. Schematically the temporal evolution phases against the spatial landing phases are depicted in Fig. 2.7 (a). The ground effect and end effect accelerate the vortex aging. The effect of a plate line is schematically depicted in Fig. 2.7 (b). The obstacle additionally accelerates the vortex aging.

2.1.5. Flight test data

To study the flare and touchdown phases, we employ flight test data. These flight tests have been performed at the *Institute of Aerodynamics and Flow Technology (DLR)* as validation experiments for the simulation model A320-ATRA on behalf of Airbus. The present flight test data of a landing (test No.12) was kindly provided by Christian Raab. Various parameters have been evaluated. The flight altitude is calculated by the static ambient pressure or by GPS sensors. The angle of attack is measured by a wind vane. True air speed is measured using a pitot tube from static and total pressure (Trenkle, 1999). Lift and drag are calculated from the measured accelerations, torsional moments of the aircraft, as well as engine forces and moments (Jategaonkar, 2006, chapter 6). Though the data are fairly fluctuating, the overall behavior can be interpreted.

The aircraft trajectory during landing is depicted in Fig. 2.8. In plot 1 the altitude, showing flare and touchdown, is plotted against the time. Note that a constant angle of approach which we use in the LES turns out to be a good approximation of the flight path. The angle of attack is shown in the second plot. Being nearly constant during approach and flare it decreases rapidly two seconds after the landing gear at 21 s has touched the ground. Note that this flight test landing is initiated with an improper angle of approach, which is corrected by the pilot at around 10 s. This results in a drop of the angle of attack and should not confuse the reader. In the simulations, a constant angle of attack is applied being a good

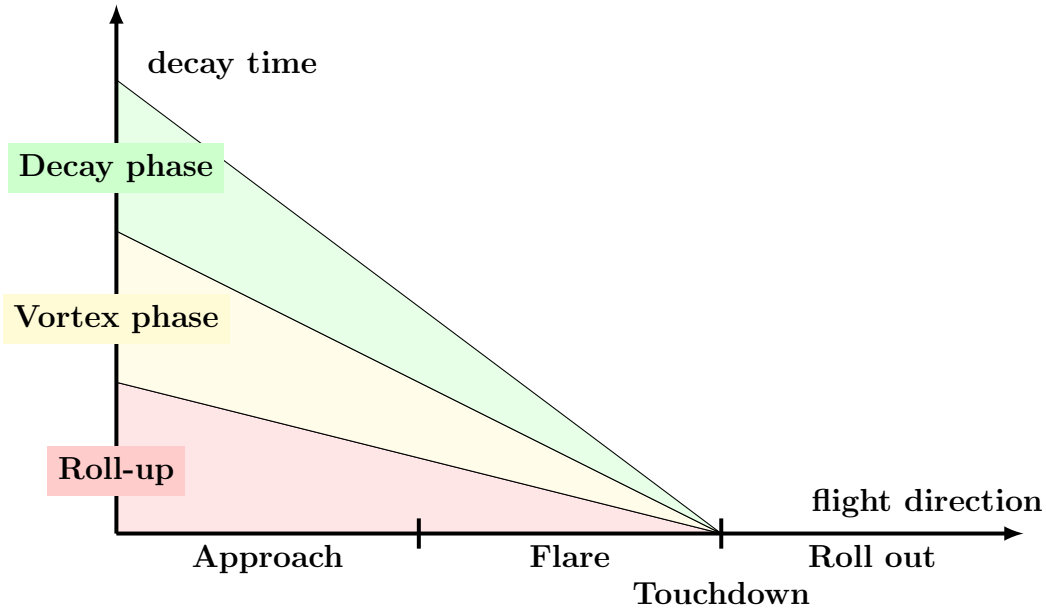

(a)

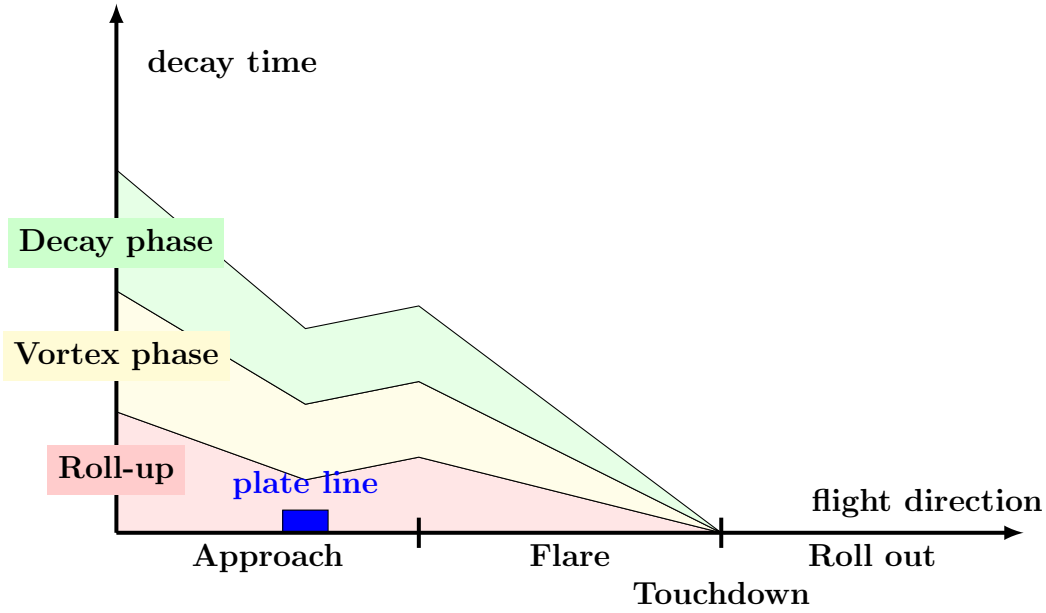

(b)

Abbildung 2.7.: Schematic of wake-vortex evolution phases in terms of the decay time plotted against landing phases represented in flight direction (a) without obstacles (b) with plate line.

approximation of the real angle of attack development. The third plot of Fig. 2.8 shows the true airspeed that slightly decreases during approach, moderately decreases during the flare and strongly decreases after touchdown. The evolutions of lift and drag coefficients are depicted in the lower two plots of Fig. 2.8. The lift coefficient slightly increases during approach and flare, and strongly increases at the instant of touchdown, where the aircraft experiences a strong vertical force. The drag coefficient stays nearly constant during most of the time and only increases drastically after touchdown.

From Eq. (2.9) the lift force L is proportional to $C_L \cdot U^2$. Fig. 2.9 (plot 2) We observe in the flight data that the increase in the lift force L is negligible, Fig. 2.9 (plot 2). Instead it fluctuates around one single level, which corresponds to the weight force generated by the aircraft. To derive a relation for the vortex strength Γ_0, note that by Eq. 2.7 the lift force L is proportional to the integral circulation $I = \int \Gamma dy$, that is $I \sim L/U$. The results from Daeninck et al. (2006) suggest that the increase of the circulation distribution by the wing-in-ground effect is approximately uniform along the wings. Hence, we may conclude

$$\Gamma_0 \sim L/U \sim C_L \cdot U, \tag{2.15}$$

by the virtue of Eq. (2.10). Beside strong fluctuations we conclude from Fig. 2.9 (plot 1) that $C_L \cdot U$ and hence the vortex strength slightly increases during approach and flare. Note that substantial fluctuations of Γ during approach and landing may, besides ambient turbulence, also contribute to the observed rapid deformation of wake vortices. We may conclude: If we assume a nearly constant lift force L balancing the weight forces, then Γ_0 increases corresponding to the decrease of U, by Eq. (2.15). However, this effect is moderate. The lift to drag ratio changes substantially more, see third plot in Fig. 2.9. It suggests an increasing of lift forces with respect to drag forces, down to an aircraft altitude of $b_0/4$ similar to the results from stationary theory. Very close to the ground this effect seems to invert, which is actually not consistent with theory. After touchdown flight data may not be correct. We assume a strong reduction of the wake-vortex circulation directly after touchdown.

2.1.6. Vortex models and parameters

The evolving two-vortex system persists for a long period of time, possessing a high amount of kinetic energy and thereby posing a potential hazard to following aircraft. After the roll-up the vortices are frequently described by vortex models in theoretical considerations. Constant vortices in flight direction are also used as initial conditions in so-called temporal numerical simulations.

Line vortex. The most simple vortex model is the line vortex in which infinite vorticity is concentrated on a line in space, see Saffman (1992). The strength Γ_0 along a closed circuit around the vortex line is finite and independent of the radius of the circuit. Line vortices are the result of a limiting process in which a vortex filament of a finite strength is concentrated to a curve. It can be considered as a weak solution to potential flows without

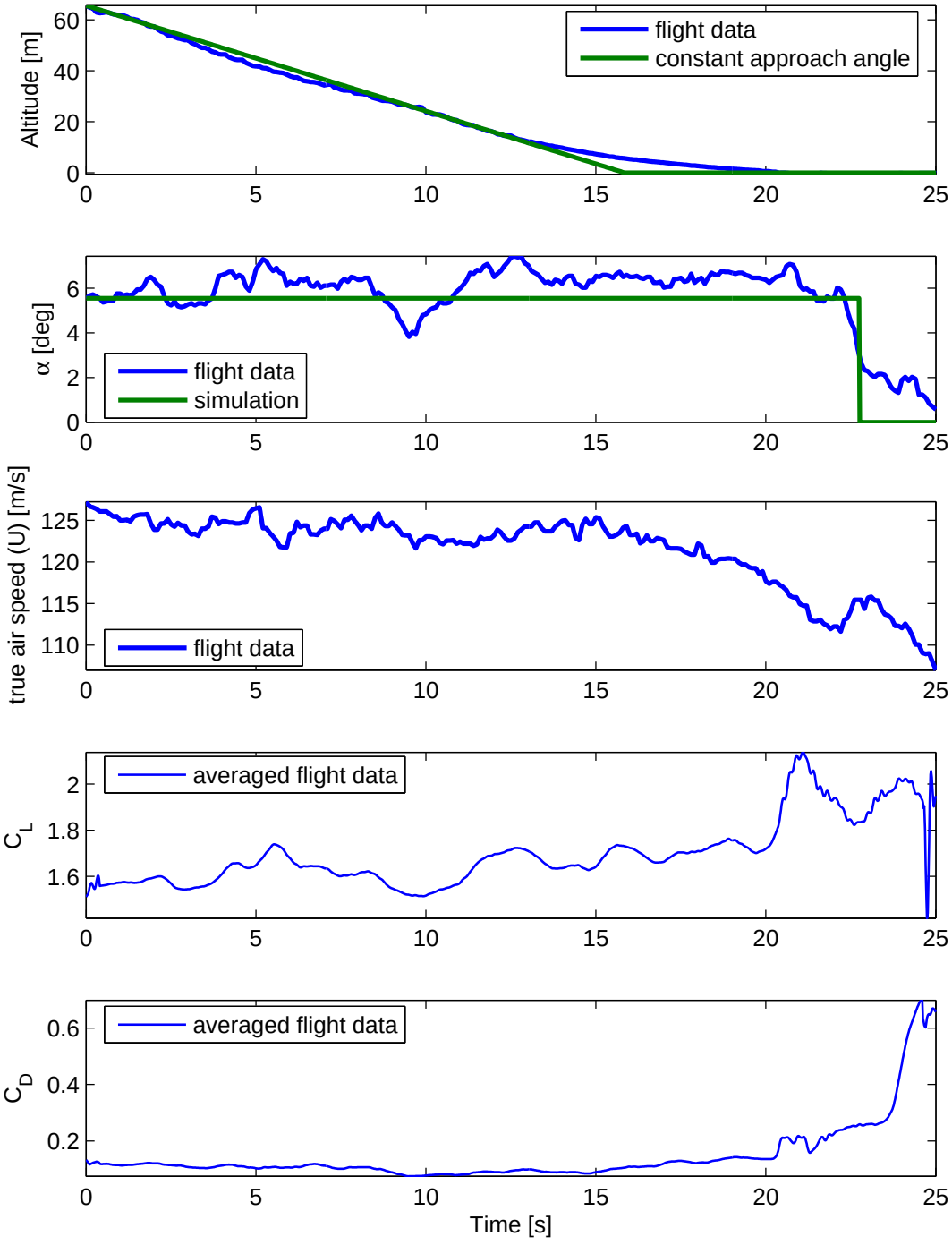

Abbildung 2.8.: Aircraft altitude, angle of attack, true air speed, lift- and drag coefficients during landing from flight measurements with ATRA research aircraft.

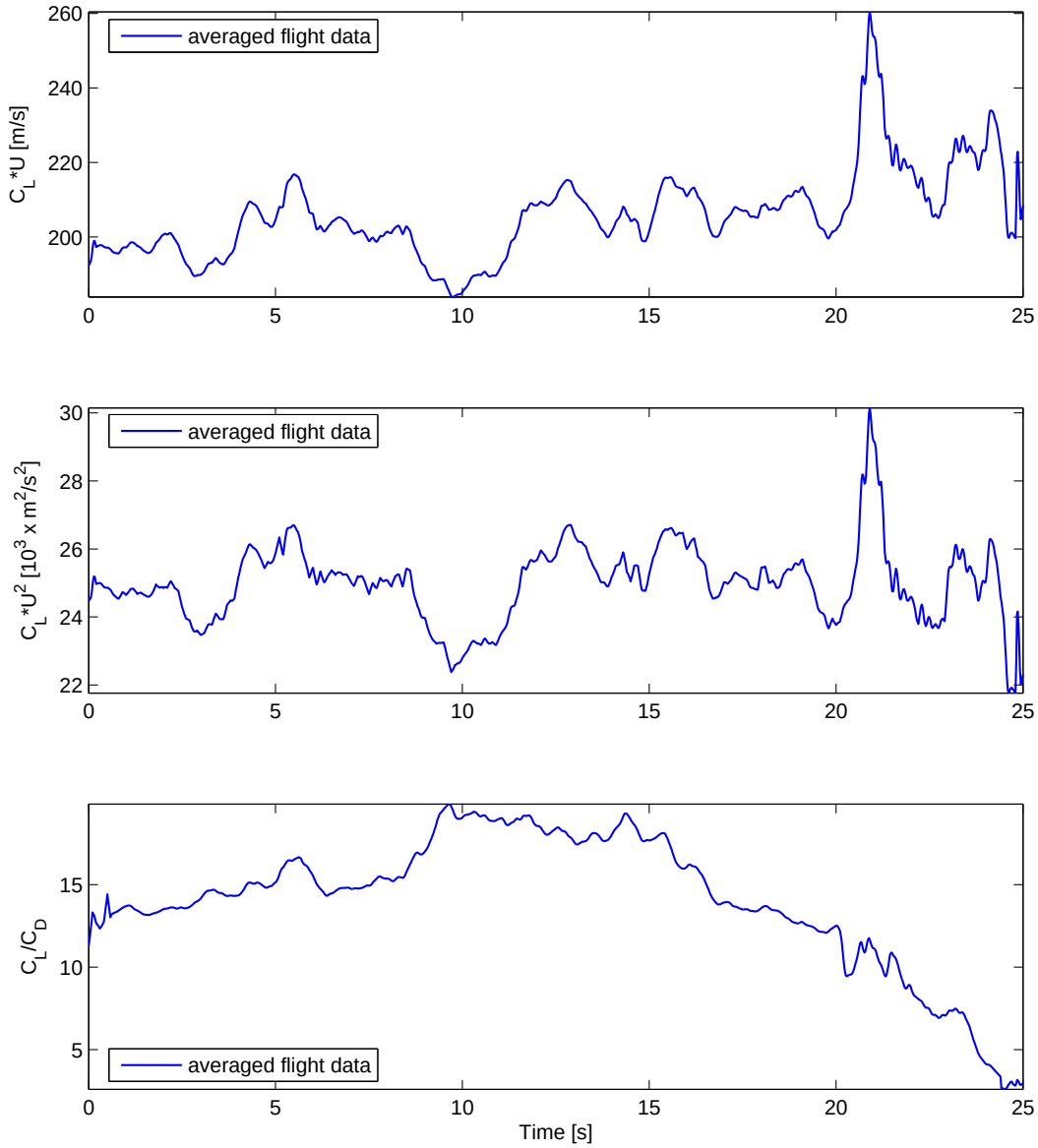

Abbildung 2.9.: Lift force, wake-vortex circulation tendencies as well as lift to drag ratio deduced from flight measurements with ATRA research aircraft.

friction and vorticity and formally expressed as

$$\vec{\omega} = \Gamma_0 \delta(n)\delta(b)\vec{s}, \tag{2.16}$$

where δ is the Dirac delta function, $\vec{s}$ is the tangent vector and n and b are the normal and bi-normal co-ordinates, respectively. For a straight line vortex in x direction the velocities in cylindrical co-ordinates are

$$V_x = 0, \quad V_r = 0, \quad V_\theta = \frac{\Gamma_0}{2\pi r}. \tag{2.17}$$

A line vortex induces a velocity to any fluid particle in space that can be computed by the Biot-Savart integral

$$\vec{u}(\vec{x}) = \frac{\Gamma_0}{4\pi} \int \frac{d\vec{s} \times \vec{r}}{|\vec{r}|^3}, \tag{2.18}$$

where $d\vec{s}$ denotes an infinitesimal line segment and $\vec{r}$ denotes the vector pointing from x to the considered point. Parallel line vortices of equal strength mutually induce a descent speed (Lamb, 1932)

$$w_0 = \frac{\Gamma_0}{2\pi b_0}. \tag{2.19}$$

The reference time in wake-vortex flows is defined by

$$t_0 = \frac{b_0}{w_0}, \tag{2.20}$$

and corresponds to the time the vortices need to descend by one vortex separation.

Lamb-Oseen vortex. The Lamb-Oseen vortex is an exact solution to the Navier-Stokes equation describing the dissipation of concentrated vorticity of a straight vortex line, which reduces to a quasi two dimensional equation

$$\frac{\partial \omega_x}{\partial t} = \nu \Delta \omega_x, \tag{2.21}$$

with the initial condition

$$\omega_x(r, t = 0) = \Gamma_0 \delta(y)\delta(z). \tag{2.22}$$

Analogously to the heat equation the solution (Saffman, 1992) can be expressed by a diffluent Gaussian heat kernel

$$\omega_x = \frac{\Gamma_0}{4\pi\nu t} e^{-r^2/4\nu t}, \quad V_\theta = \frac{\Gamma_0}{2\pi r}(1 - e^{-r^2/4\nu t}), \quad \Gamma = \Gamma_0(1 - e^{-r^2/4\nu t}). \tag{2.23}$$

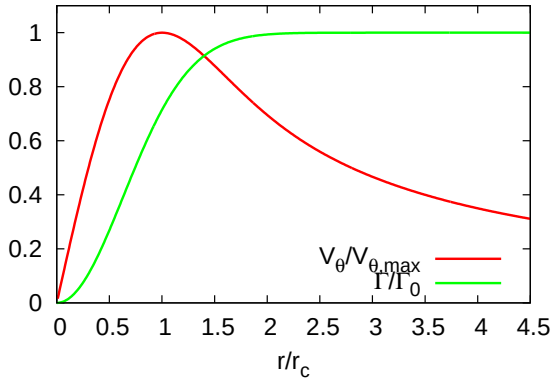

Abbildung 2.10.: Normalized tangential velocity profile of one Lamb-Oseen Vortex.

The tangential velocity profile can be rewritten as

$$V_\theta = \frac{\Gamma_0}{2\pi r}(1 - e^{-1.2526\left(\frac{r}{r_c}\right)^2}), \tag{2.24}$$

where $r_c = 2.24\sqrt{\nu t}$ denotes the core radius, defined as the distance between the vortex center and the point of maximal tangential velocity $V_{\theta,\max}$, which can be computed by some Newton iterations. The tangential velocity profile is depicted in Fig. 2.10.

A listing of other frequently used analytical and empirical vortex models can be found in Gerz et al. (2002); Breitsamter (2007).

Radial circulation distribution. For a single axisymmetric vortex the circulation is obtained from V_θ by

$$\Gamma(r) = \oint \vec{u} \cdot d\vec{s} = 2\pi r V_\theta(r). \tag{2.25}$$

In the case of a vortex pair, with $b_0 >> r_c$ as we use for modelling the wake vortices, by the limit $r \to b_0/2$ the whole vorticity field is captured and $\Gamma(r) \to \Gamma_0$. For $r > b_0/2$ $\Gamma(r)$ decreases as parts of the vorticity field of the conterrotating vortex are integrated. Therefore the maximal circulation $\Gamma_{\max}$ depending on r is a possible measure for vortex intensity. It is used in this thesis for comparisons with water towing tank experiments.

As another common measure of the vortex intensity for aircraft with sufficiently large wingspan, $\Gamma_{5-15} = 0.1 \int_{5\,\mathrm{m}}^{15\,\mathrm{m}} \Gamma(r)dr$ has established (Holzäpfel et al., 2003b). This averaging of circulations around circuits of 5 m to 15 m is used in LIDAR measurements as a smoothing of scattered data. In addition, measurement errors due to the neighboring vortex are less sensitive to the viewing angle (Campbell et al., 1997). Finally, Γ_{5-15} correlates well with the effect of wake encounters (Hinton & Tatnall, 1997). For the secondary vortices $\Gamma_{r=5\,\mathrm{m}}$ is used, see Stephan et al. (2013a).

Vortex position. The vortex core position is computed by the centroids y_c, z_c in half-planes perpendicular to the wake Gerz et al. (2002)

$$y_c = \frac{1}{\Gamma_0} \int_{-\infty}^{\infty} \int_{0}^{\infty} y \omega_x dy dz \tag{2.26}$$

$$z_c = \frac{1}{\Gamma_0} \int_{-\infty}^{\infty} \int_{0}^{\infty} z \omega_x dy dz. \tag{2.27}$$

The vortex separation is the difference of the two centroids of lateral position. Assuming that the centroids are constant during the roll-up the vortex separation equals b_0.

Normalization. Velocities, lengths, and time are normalized by w_0, b_0, t_0, respectively, vorticity ω is normalized by t_0^{-1} and Γ_{5-15} by Γ_0.

2.2. Ambient Turbulence Field

2.2.1. Ambient wind

In order to investigate a realistic environment, a turbulent wind is established in a pre-simulation. This way time dependent velocity fluctuations are introduced, modeling the atmospheric boundary layer physically. A turbulent half-channel flow is simulated with wall-resolved LES with smooth top and bottom walls. A free-slip condition is applied at the top of the domain and a no-slip condition at the bottom (Moser et al., 1999). Prescribing initially a vertical wind profile, following the universal logarithmic law and imposing a stream-wise pressure gradient, the wind flow is driven through the computational domain.

A recapitulation of the basic properties, as velocity profiles, fluctuations and normalization of the turbulent channel flow (Schlichting & Gersten, 1997; Fröhlich, 2006; Kundu & Cohen, 1990) is as follows: Following the idea of Reynolds (1895) variables are averaged in time. For any quantity q let the mean value $\overline{q}$ and the fluctuation q' be defined by

$$\overline{q} = \frac{1}{T} \int_{t_0}^{t_0+T} q dt, \quad q = \overline{q} + q'.$$

The statistical Reynolds-averaged equations, see Schlichting & Gersten (1997), reduce such that $\overline{u}$ as well as other turbulence quantities depend only on z, and $\overline{v} = \overline{w} = 0$. With Reynolds-Approximation for boundary layer flow ($\mathrm{Re} \to \infty$, $\partial/\partial x \ll \partial/\partial z$) Eq. (2.1) reduce to

$$\frac{d\overline{p}_\mathrm{w}}{dx} = \frac{\partial \overline{\tau}}{\partial z}$$

where

$$\overline{\tau} = \mu \frac{\partial \overline{u}}{\partial z} - \rho \overline{u'w'},$$

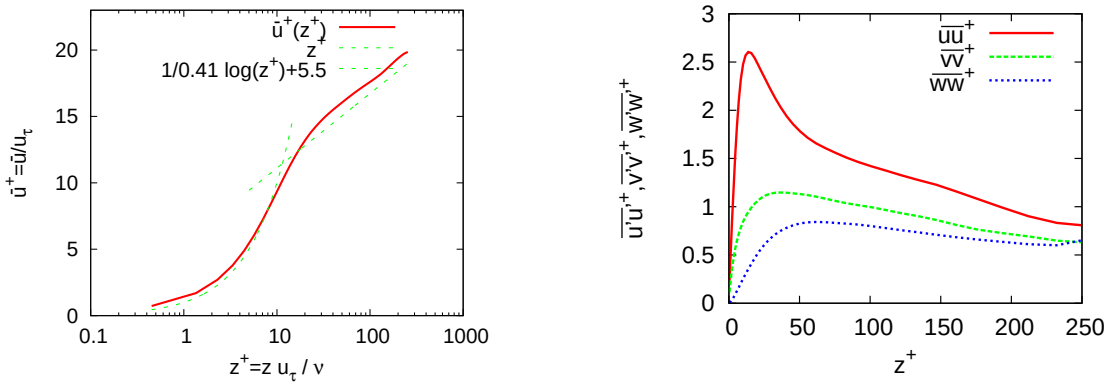

Abbildung 2.11.: Mean velocity profile and velocity fluctuations characterizing the turbulent wind (Stephan et al., 2013a).

and $\overline{p}_{\mathrm{w}}$ equals the averaged pressure at the wall. After integrating we get

$$\overline{\tau} = \overline{\tau}_{\mathrm{w}} + \frac{d\overline{p}_{\mathrm{w}}}{dx} z, \tag{2.28}$$

where τ_{w} denotes the wall shear stress. For reasons of symmetry the integration of Eq. (2.28) yields

$$0 = \overline{\tau}_{\mathrm{w}} + \frac{d\overline{p}_{\mathrm{w}}}{dx}\delta, \quad \Rightarrow \quad \overline{\tau}_{\mathrm{w}} = -\frac{d\overline{p}_{\mathrm{w}}}{dx}\delta \tag{2.29}$$

The wall friction velocity is defined by $u_\tau = (\overline{\tau}_w/\rho)^{1/2}$ and we can introduce the non-dimensional values

$$u^+ = \frac{\overline{u}}{u_\tau}, \quad \mathrm{Re}_\tau = \frac{u_\tau \delta}{\nu}, \quad z^+ = \frac{z u_\tau}{\nu} = \mathrm{Re}_\tau \frac{z}{\delta} \tag{2.30}$$

where δ equals the channel half height.
Eq. (2.30) and (2.29) yield a relation between the Reynolds number Re_τ and the pressure gradient $\frac{d\overline{p}_{\mathrm{w}}}{dx}$

$$\frac{d\overline{p}_{\mathrm{w}}}{dx} = -\frac{\rho\nu^2\,\mathrm{Re}_\tau^2}{\delta^3}. \tag{2.31}$$

The boundary layer of a turbulent flow over a smooth surface has now three characteristic parts, the viscous sublayer, the transition layer and the logarithmic layer, see Fig. 2.11. In normalized coordinates the mean wall profile is independent of the Reynolds number. Following the above mentioned books the averaged vertical velocity profile in the outer region ($z^+ > 30$) equals:

$$u^+(z^+) = \frac{1}{\kappa}\log(z^+) + B, \text{or} \tag{2.32}$$

$$\overline{u}(z) = \frac{\mathrm{Re}_\tau\,\nu}{\delta}\left(\frac{1}{\kappa}\log\left(\frac{z\,\mathrm{Re}_\tau}{\delta}\right) + B\right) \tag{2.33}$$

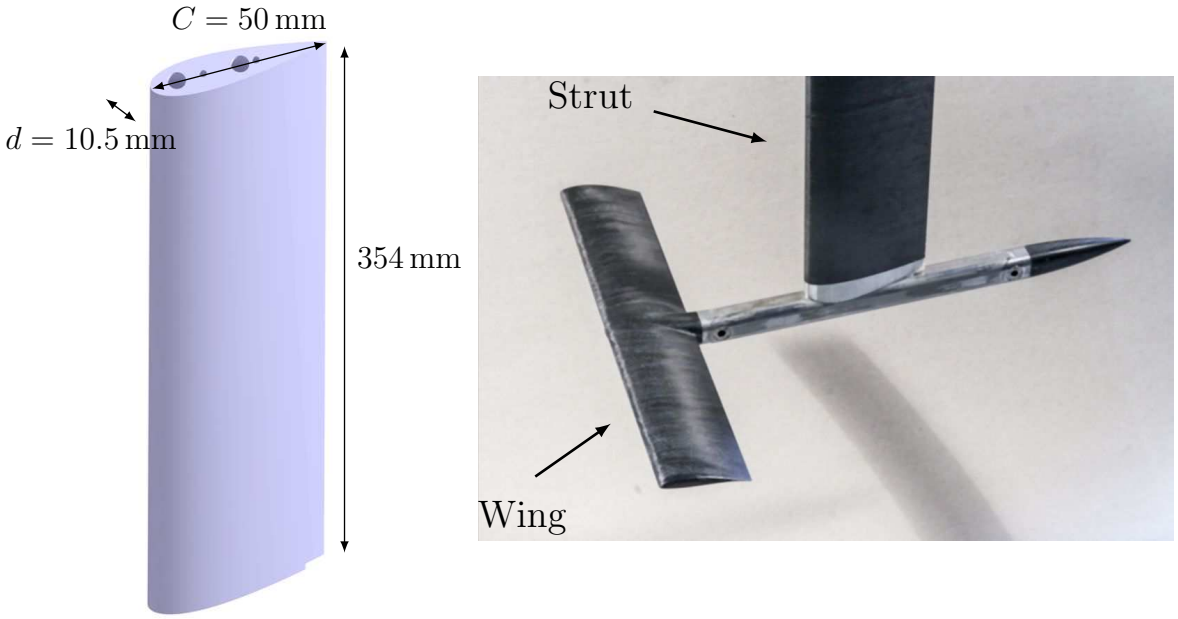

(a) (b)

Abbildung 2.12.: (a) Schematic of the strut. (b)Aircraft model / vortex generator. (Stephan et al., 2013c).

From experiments we employ $\kappa = 0.41$ as the von Karman constant, recently proved analytically to be $1/\sqrt{2\pi} \approx 0.399$ (Baumert, 2012), and $B = 5.5$. In the inner region ($z^+ < 5$) the velocity profile equals

$$u^+(z^+) = z^+, \tag{2.34}$$

see Fröhlich (2006).

In normalized coordinates the mean wall profile is independent of the Reynolds number. Thus, in case of realistic Reynolds numbers, we have a very thin viscous sublayer and no significant changes of the mean flow speed in the region of vortex initialization at $z_0 = b_0$. In a fully developed flow each region has its own flow field characteristics. The viscous sublayer is shaped by coherent structures, so-called near-wall streaks. For Reynolds numbers $\mathrm{Re}_\tau < 1000$ this near-wall streaks are proven to have a spanwise spacing of $\lambda^+ \sim 100$ (Jimenez & Moin, 1991). To resolve the viscous sublayer wall-resolved LES requires a stretched mesh in wall-normal direction, with $z^+_{\mathrm{min}} < 1$, see Sec. 2.4.1. This limits wall-resolved simulations.

2.2.2. Strut wake turbulence

For comparison of the results from LES with water towing tank experiments in the discussion chapter 4 the turbulence occurring in the experiments is modeled. In a water towing

tank an aircraft model is attached to a profiled strut, see Fig. 2.12 (b). The wake of the profiled strut is considered to be the most important source of turbulence generated by the towed aircraft model. Figure 2.12 (a) depicts the geometry and dimensions of the symmetric profile. Other sources of turbulence like strut-body junction vortices as well as the turbulence generated during the vortex roll-up are not taken into account. The airfoil (strut) chord length C is 50 mm, maximal thickness of the airfoil d is 10.5 mm. The chord Reynolds number based on the towing speed is $\mathrm{Re}_c = 1.22 \times 10^5$. The vertically extended turbulence structures behind the strut are transported downwards and stretched in the primary vortex field, see Fig. 2.13. The turbulence structures behind a symmetric airfoil at comparable Reynolds numbers are carefully studied in Hah & Lakshminarayana (1982) and Zhang et al. (2004).

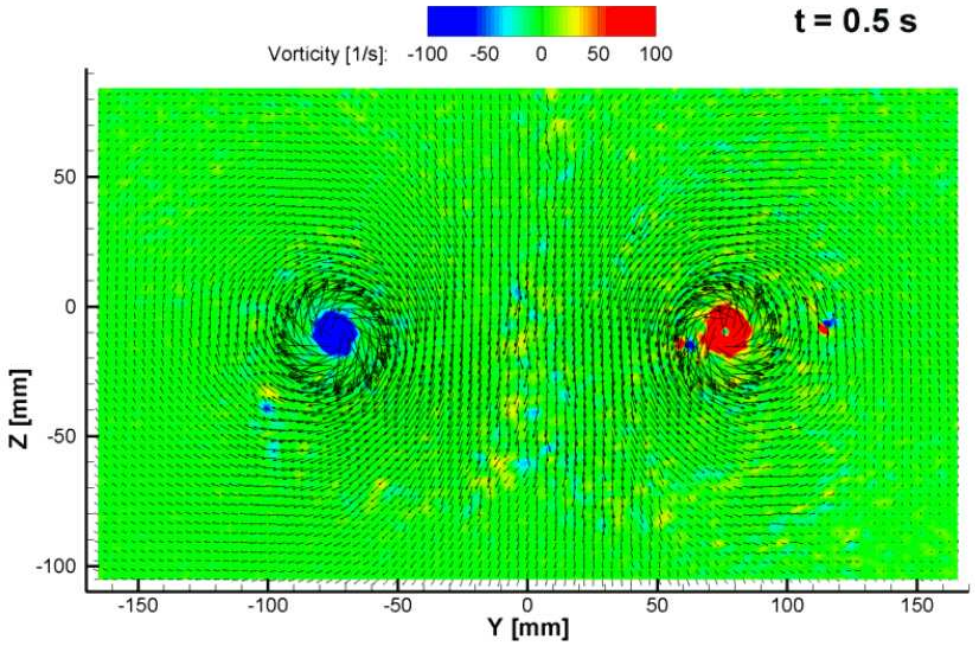

Abbildung 2.13.: Strut wake turbulence, vorticity (color coded) and velocity vectors (tiny vectors) measured at high altitudes above ground by PIV. (Stephan et al., 2013c).

From the results in Hah & Lakshminarayana (1982) the turbulence characteristics in the wake are deduced. From the measured turbulence profiles presented in Hah & Lakshminarayana (1982) diffusion type similarity profiles for the fluctuation velocity u_{rms} are postulated:

$$u_{\mathrm{rms}}(y,t) = \frac{b\nu_t}{\sqrt{4\pi\nu_t t}} \cdot \exp\left(-\frac{1}{2}\left(\frac{y}{\sqrt{2\nu_t t}}\right)^2\right), \tag{2.35}$$

with ν_t representing a turbulent viscosity. If u_{rms} is normalized by the towing speed U,

and axial and lateral coordinates by the chord length C, $x' = \frac{x}{C}$, $y' = \frac{y}{C}$ and it is further assumed that $x \sim t \cdot U$, one has

$$\frac{u_{\mathrm{rms}}}{U} = \frac{a \cdot b}{\sqrt{2\pi}\sigma'(x')} \cdot \exp\left(-\frac{1}{2}\left(\frac{y'}{\sigma'(x')}\right)^2\right), \ \sigma'(x') = \sqrt{2ax'}, \ a = \frac{\nu_t}{UC} \tag{2.36}$$

The data presented in Hah & Lakshminarayana (1982) is fitted, which yields $b = 4.1$ and $a = 0.001$. For simplicity

$$v_{\mathrm{rms}}/U = w_{\mathrm{rms}}/U = u_{\mathrm{rms}}/U \tag{2.37}$$

is scaled which holds well in the far wake. Figure 2.14 depicts the resulting similarity profiles.

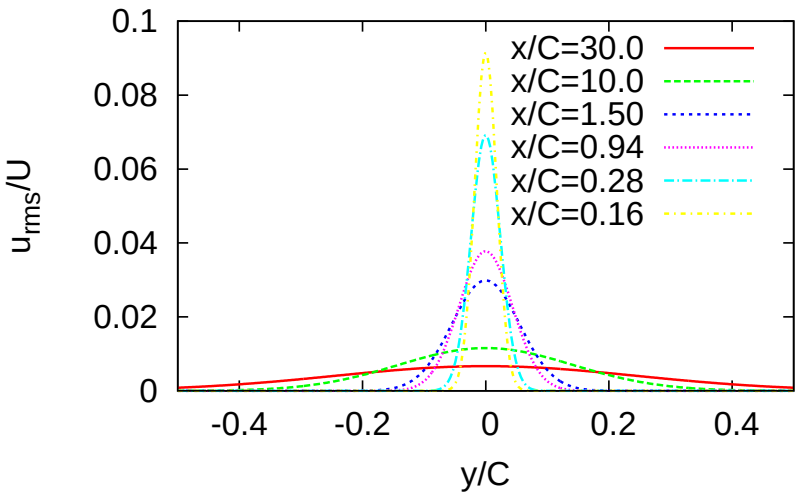

Abbildung 2.14.: Streamwise turbulence intensity distributions for different distances from the strut (Stephan et al., 2013c).

2.3. LES Code

The LES code applied for wake vortex flows all over the thesis is the incompressible Navier-Stokes solver MGLET, developed at Technische Universität München for solving the Navier-Stokes equations and the continuity equation (Manhart, 2004). The second order version of MGLET was developed first and applied to several fluid dynamic problems

(Manhart & Friedrich, 2002; Manhart, 2004; Schwarzer et al., 2006; Schwertfirm et al., 2007). In the original version this code enables to simulate complex computational domains, build by multiple domains with independent Cartesian grids. These grids can be connected in various ways, allowing a well-resolved computation of flows around complex geometries. Multiple dynamic sub-grid scale models are integrated. MGLET was upgraded to fourth order (Hokpunna & Manhart, 2010) and the pressure solver was modified (Misaka et al., 2012b). Recently a method for sweeping RANS flow fields through the LES domain together with a code for preprocessing raw RANS fields was developed (Misaka et al., 2013).

During the last decades two different incompressible flow solvers for investigating wake vortex flows have been used in the Institute of Atmospheric Physics. LESTUF a finite difference code of second order both in time and space with a Fourier pressure solver and a modified Smagorinsky subgrid closure model (Gerz et al., 1989). Secondly, a multi-scale flow solver EULAG constructed on both Eulerian and Lagrangian frameworks, also using a space-time second order scheme (Smolarkiewicz, 2006). EULAG is available with a Smagorinsky, a one-equation turbulent kinetic energy as well as an implicit turbulence closure model (Margolin et al., 2002). The benchmark comparisons of different codes (Dufresne et al., 2005; Misaka et al., 2010) revealed the advantages of MGLET especially in wake vortex flow.

2.3.1. Governing equations

MGLET is a computational fluid dynamics (CFD) simulation code for engineering applications. Navier-Stokes equation and the continuity equation (Manhart, 2004)

$$\frac{\partial u_i}{\partial t} + \frac{\partial (u_i u_j)}{\partial x_j} = -\frac{1}{\rho}\frac{\partial p'}{\partial x_i} + \frac{\partial}{\partial x_j}\left((\nu_{\mathrm{mol}} + \nu_{\mathrm{turb}}) 2 S_{ij}\right) \tag{2.38}$$

$$\frac{\partial u_j}{\partial x_j} = 0\,. \tag{2.39}$$

are solved. Here u_i represent the cell averaged velocity components in three spatial directions ($i, j = 1, 2,$ or 3) and $S_{ij} = (\partial u_i/\partial x_j + \partial u_j/\partial x_i)/2$ denotes the strain rate tensor. The summation convention is used for the velocity components. $p' = p - p_0$ equals the deviation from the reference state p_0.

The kinematic viscosity is given as the sum of molecular viscosity ν_{mol} and eddy viscosity ν_{turb} defined by means of a Lagrangian dynamic subgrid-scale model (Meneveau et al., 1996). Equations (2.38) and (2.39) are solved by a finite-volume approach using a fourth-order finite-volume compact scheme (Kobayashi, 1999; Hokpunna & Manhart, 2010). A split-interface algorithm is used for the parallelization of the tri-diagonal system (Hokpunna, 2009). The pressure field is obtained by the velocity-pressure iteration method by Hirt & Cook (1972). A third-order Runge-Kutta method is used for time integration. The simulations are performed in parallel using a domain decomposition approach.

In addition, an equation for a passive tracer is employed

$$\frac{\partial q}{\partial t} + u_j \frac{\partial q}{\partial x_j} = D\Delta q, \tag{2.40}$$

considering convection induced by local velocity and diffusion modeled by the diffusivity D.

2.3.2. Lagrangian dynamic subgrid-scale model

LES require a subgrid-scale model. The standard Smagorinsky model overestimates the the eddy viscosity in vortex cores as well as at solid walls (Schumann, 1975), where the flow remains mostly laminar. Hence, for vortex flows, where large velocity gradients in the vortex core cause large eddy viscosity, a correction procedure for the Smagorinsky model is required (Holzäpfel, 2004; Shen et al., 1999). To account for the anisotropy close to walls, damping functions for ν_{turb} are frequently used (Fröhlich, 2006).

The dynamic procedure developed by Germano et al. (1991) provides a more accurate turbulent viscosity model by varying the Smagorinsky constant in space. It is calculated using two different filters for the subscales and averaged in certain homogeneous directions. Let $\overline{u}_i$ and $\hat{u}_i$ denote two filtering operations with two different filter widths Δ and 2Δ applied to a certain quantity. The filtered impulse equation reads as follows:

$$\frac{\partial \overline{u}_i}{\partial t} + \frac{\partial(\overline{u}_i\overline{u}_j)}{\partial x_j} = -\frac{1}{\rho}\frac{\partial \overline{p}}{\partial x_i} + \frac{\partial(\nu_{\text{mol}} 2\overline{S}_{ij})}{\partial x_j} - \frac{\partial \tau_{ij}}{\partial x_j}, \tag{2.41}$$

where

$$\tau_{ij} = \overline{u_i u_j} - \overline{u}_i\overline{u}_j \tag{2.42}$$

represents the impact of the unresolved velocity components and has to be modeled. If we define the expressions

$$L_{ij} = \widehat{\overline{u}_i\overline{u}_j} - \hat{\overline{u}}_i\hat{\overline{u}}_j \quad \text{and} \quad T_{ij} = \widehat{\overline{u_i u_j}} - \hat{\overline{u}}_i\hat{\overline{u}}_j \tag{2.43}$$

we obtain the so-called Germano identity

$$L_{ij} = T_{ij} - \hat{\tau}_{ij}. \tag{2.44}$$

This identity is used for a model of the subgrid-scale. The Smagorinsky model is applied

$$\tau_{ij} = -2c_s^2\Delta^2|\overline{S}|\overline{S}_{ij}, \quad T_{ij} = -2c_s^2(2\Delta)^2|\widehat{\overline{S}}|\widehat{\overline{S}}_{ij} \tag{2.45}$$

at scales Δ and 2Δ, respectively, with the variable model coefficient c_s^2. Substituting Eq. (2.45) into Eq. (2.43) yields an overdetermined system of equations for c_s^2, which is determined by minimizing the error

$$e_{ij} = L_{ij} - 2\Delta^2\left[\widehat{c_s^2|\overline{S}|\overline{S}_{ij}} - 4c_s^2|\widehat{\overline{S}}|\widehat{\overline{S}}_{ij}\right]. \tag{2.46}$$

With the assumption of a constant c_s^2 for a certain homogeneous spatial direction the Smagorinsky constant can be computed by a least-square minimization technique.

The Lagrangian dynamic model (Meneveau et al., 1996) does not require directions of statistical homogeneity for the averaging process. Instead the averaging is performed along fluid-particle trajectories. Let a fluid particle be located at position $\boldsymbol{x}$ at time t. It's trajectory for earlier times $t' < t$ is given by

$$z(t') = x - \int_{t'}^{t} \overline{\boldsymbol{u}}[\boldsymbol{z}(t''), t'']dt''. \tag{2.47}$$

Meneveau et al. (1996) assumes that c_s^2 does not strongly vary in space. Hence, it can be removed in Eq. (2.46) from the filter operation. This yields an error at a certain point

$$e_{ij}(\boldsymbol{x}, t) = L_{ij}(\boldsymbol{x}, t) - c_s^2(\boldsymbol{x}, t)M_{ij}(\boldsymbol{x}, t),$$

with

$$M_{ij} = 2\Delta^2 \left[\widehat{|\overline{S}|\overline{S}}_{ij} - 4|\widehat{\overline{S}}|\widehat{\overline{S}}_{ij} \right].$$

In the Lagrangian formulation the error to be minimized reads

$$E = \int_{-\infty}^{t} e_{ij}(\boldsymbol{z}(t'), t')e_{ij}(\boldsymbol{z}(t'), t')W(t - t')dt',$$

with a weighting function $W(t - t')$ controlling the relative importance of the history. A variational minimization with respect to c_s^2 requires $\frac{\partial E}{\partial c_s^2} = 0$ leading to

$$c_s^2(\boldsymbol{x}, t) = \frac{\mathcal{I}_{LM}}{\mathcal{I}_{MM}},$$

with

$$\begin{aligned} \mathcal{I}_{LM} &= \int_{-\infty}^{t} L_{ij}M_{ij}(\boldsymbol{z}(t'), t')W(t - t')dt' \\ \mathcal{I}_{LM} &= \int_{-\infty}^{t} M_{ij}M_{ij}(\boldsymbol{z}(t'), t')W(t - t')dt'. \end{aligned}$$

To choose $W(t - t') = T^{-1}e^{-(t-t')/T}$ has the advantage, that the integrals $\mathcal{I}_{LM}$ and $\mathcal{I}_{MM}$ are solutions for the relaxation-transport equations:

$$\begin{aligned} \frac{D\mathcal{I}_{LM}}{Dt} = \frac{\partial \mathcal{I}_{LM}}{\partial t} + \overline{\boldsymbol{u}} \cdot \nabla \mathcal{I}_{LM} &= \frac{1}{T}(L_{ij}M_{ij} - \mathcal{I}_{LM}), \\ \frac{D\mathcal{I}_{MM}}{Dt} = \frac{\partial \mathcal{I}_{MM}}{\partial t} + \overline{\boldsymbol{u}} \cdot \nabla \mathcal{I}_{MM} &= \frac{1}{T}(M_{ij}M_{ij} - \mathcal{I}_{MM}). \end{aligned}$$

The time scale T is chosen to be

$$T = 1.5\Delta(\mathcal{I}_{LM}\mathcal{I}_{MM})^{-1/8}.$$

Thus, the Lagrangian dynamic model requires two additional transport equations. Numerically these equations are solved by a straight forward discretization:

$$\begin{aligned}\frac{\mathcal{I}_{LM}^{n+1}(\boldsymbol{x}) - \mathcal{I}_{LM}^{n+1}(\boldsymbol{x} - \overline{\boldsymbol{u}}^n \Delta t)}{\Delta t} &= \frac{1}{T^n}\left([L_{ij}M_{ij}]^{n+1}(\boldsymbol{x}) - \mathcal{I}_{LM}^{n+1}(\boldsymbol{x})\right) \\ \frac{\mathcal{I}_{MM}^{n+1}(\boldsymbol{x}) - \mathcal{I}_{MM}^{n+1}(\boldsymbol{x} - \overline{\boldsymbol{u}}^n \Delta t)}{\Delta t} &= \frac{1}{T^n}\left([M_{ij}M_{ij}]^{n+1}(\boldsymbol{x}) - \mathcal{I}_{MM}^{n+1}(\boldsymbol{x})\right),\end{aligned}$$

leading to

$$\begin{aligned}\mathcal{I}_{LM}^{n+1}(\boldsymbol{x}) &= \epsilon[L_{ij}M_{ij}]^{n+1}(\boldsymbol{x}) + (1-\epsilon)\mathcal{I}_{LM}^{n+1}(\boldsymbol{x} - \overline{\boldsymbol{u}}^n \Delta t) \\ \mathcal{I}_{MM}^{n+1}(\boldsymbol{x}) &= \epsilon[M_{ij}M_{ij}]^{n+1}(\boldsymbol{x}) + (1-\epsilon)\mathcal{I}_{MM}^{n+1}(\boldsymbol{x} - \overline{\boldsymbol{u}}^n \Delta t)\end{aligned}$$

where $\epsilon = \Delta t/(T^n + \Delta t)$. The choice of parameters that are implemented in the used code corresponds to that of Meneveau et al. (1996) which are validated in several benchmark simulations there.

2.3.3. Fourth-order finite volume compact scheme

The finite volume method describes the change of volume-averaged quantities by the sum of surface-averaged fluxes on the surface enclosing a control volume where cell-averaged and surface-averaged values are not interchangeable. Let $'$ denote the surface averaged value.

The momentum equation is solved on a staggered grid system, where volume-averaged pressure is located in the cell centers and volume-averaged velocities are located at the cell-surfaces cf. Hokpunna (2009).

The discrete continuity equation is given by

$$0 = (u'_{i+\frac{1}{2},j,k} - u'_{i-\frac{1}{2},j,k})/\Delta x_i + (v'_{i,j+\frac{1}{2},k} - v'_{i,j-\frac{1}{2},k})/\Delta y_i + (w'_{i,j,k+\frac{1}{2}} - w'_{i,j,k-\frac{1}{2}})/\Delta z_i$$

The conservation of momentum per unit mass for $\boldsymbol{u}_{i,j,k} = (u_{i,j,k}, v_{i,j,k}, w_{i,j,k})^T$ reads for the first component as

$$\frac{\partial \boldsymbol{u}_{i,j,k}}{\partial t} = -\boldsymbol{C}_{i,j,k} + \boldsymbol{D}_{i,j,k} - \boldsymbol{P}_{i,j,k}, \tag{2.48}$$

where $\boldsymbol{C}, \boldsymbol{D}, \boldsymbol{P}$ are shorthand notations of net convective, diffusive and pressure fluxes calculated from the surface-averaged quantities.

The surface-averaged fluxes are approximated from the cell-averaged values to fourth-order, called deconvolution, which can be found by Taylor expansion. $\boldsymbol{C}$ as well as $\boldsymbol{D}$ depend on surface-averaged fluxes located at the interfaces between the volume-averaged quantities. In the compact scheme (Lele, 1992) we have an implicit approximation leading to a tri-diagonal linear system of equations. This requires shorter stencils. The convective fluxes are calculated distinguishing *convective* and *convected* velocities. The convective velocities are calculated to be fourth-order divergence-free. The product of *convective* and *convected* velocities is also approximated to fourth-order.

Solid surfaces as a Dirichlet boundary condition as well as free-slip Neumann boundaries require a special treatment, a third-order closure is implemented in the code. This does not degrade the global accuracy (Hokpunna, 2009).

2.3.4. Split-interface algorithm

The compact scheme requires an efficient algorithm to solve tridiagonal systems in parallel. In Hokpunna (2009) the interface-splitting algorithm for diagonal dominant tridiagonal matrices is presented which is implemented in MGLET. It is a modification of the algorithm presented in Sun (1995) integrating the bidirectional communication links of modern computers. The system $\boldsymbol{Ax} = \boldsymbol{b}$, with $\boldsymbol{A} = [l_i, d_i, r_i], |d_i| > |l_i| + |r_i|$ and $l_1 = r_n = 0$ is decomposed into $\boldsymbol{TQx} = \boldsymbol{b}$ with

$$\boldsymbol{Q} = \begin{pmatrix} \boldsymbol{N}^1 & & & \\ & \boldsymbol{N}^2 & & \\ & & \ddots & \\ & & & \boldsymbol{N}^p \end{pmatrix} \quad \text{and} \quad \boldsymbol{N}^k = \left(\begin{array}{cccc|c} d_{c+1} & r_{c+1} & & & \\ l_{c+2} & d_{c+2} & r_{c+2} & & \\ & \ddots & \ddots & \ddots & \\ & & l_{c+m-1} & d_{c+m-1} & r_{c+m-1} \\ \hline & & & & 1 \end{array}\right),$$

where p is the number of processors, $c = (k-1)m$ and $\boldsymbol{T}$ is a transformation matrix. The pre-processing operation $\boldsymbol{v} = \boldsymbol{T}^{-1}\boldsymbol{v}$ can be obtained by manipulating $\boldsymbol{b}$ only at the interface $\boldsymbol{v} = \boldsymbol{b} - \boldsymbol{f}$ using a sparse vector $\boldsymbol{f}$ with non-zero components only in the neighborhood of the interface. Each processor then solves its independent subsystem $\boldsymbol{N}^k\boldsymbol{x}^k = \boldsymbol{v}^k$ using the Thomas algorithm. An accuracy and performance analysis is performed in Hokpunna (2009).

2.3.5. Velocity-pressure iteration method on a multi grid

For the Poisson equations a standard velocity-pressure iteration derived from Newton iteration is used (Hirt & Cook, 1972). In Brandt et al. (1980) it is shown that in case of second order discretization of divergence and the Laplace operator the iteration equations can also be derived from a Gauss Seidel method. Here the Newton approach is presented.

Consider the integration step of Eq. (2.48)

$$\boldsymbol{u}_{i,j,k}^{n+1} = -\Delta t \boldsymbol{P}_{i,j,k} + \boldsymbol{u}_{i,j,k}^{*}, \tag{2.49}$$

with $\boldsymbol{u}_{i,j,k}^{*} = -\boldsymbol{C}_{i,j,k}^{n} + \boldsymbol{D}_{i,j,k}^{n}$. Applying divergence the Poisson equation follows from continuity equation:

$$\Delta p^{n+1} = \frac{\rho}{\Delta t} \operatorname{div} \boldsymbol{u}^{*}. \tag{2.50}$$

Consider $D(p) = \frac{\Delta t}{\rho}\Delta p$. With Newton's method p and $\boldsymbol{u}$ is iterated until the divergence $\operatorname{div} \boldsymbol{u}$ is sufficiently small:

$$p^{(k+1)} = p^{(k)} + \delta p = p^{(k)} - \frac{D(p)}{\frac{\partial D(p)}{\partial p}}. \tag{2.51}$$

A fourth-order discretization is applied (Hokpunna, 2009). The fourth-order Laplacian is given by the composition of the fourth order gradient and divergence:

$$\frac{\partial^2 p_{i,j,k}}{\partial x^2} = \frac{p_{i\pm3,j,k} - 54p_{i\pm2,j,k} + 783p_{i\pm1,j,k} - 1460p_{i,j,k}}{576}.$$

It follows for each cell

$$\frac{\partial D_{i,j,k}}{\partial p_{i,j,k}} = \frac{\Delta t}{\rho}\frac{1460}{576}\left(\frac{1}{\Delta x^2} + \frac{1}{\Delta y^2} + \frac{1}{\Delta z^2}\right),$$

leading to the algorithm:

$$\begin{aligned}
\delta p^{(k)}_{i,j,k} &= \operatorname{div}_{i,j,k} \boldsymbol{u}^{(k)} \Big/ \left(\frac{1460}{576}\frac{\Delta t}{\rho}\left(\frac{1}{\Delta x^2} + \frac{1}{\Delta y^2} + \frac{1}{\Delta z^2}\right)\right) \\
p^{(k+1)}_{i,j,k} &= p^{(k)}_{i,j,k} + \delta p^{(k)}_{i,j,k} \\
u^{(k+1)}_{i-1,j,k} &= u^{(k)}_{i-1,j,k} - \frac{\Delta t}{\rho}\delta p^{(k)}_{i,j,k}/\Delta x, \quad u^{(k+1)}_{i,j,k} = u^{(k)}_{i,j,k} + \frac{\Delta t}{\rho}\delta p^{(k)}_{i,j,k}/\Delta x \\
v^{(k+1)}_{i,j-1,k} &= v^{(k)}_{i,j-1,k} - \frac{\Delta t}{\rho}\delta p^{(k)}_{i,j,k}/\Delta y, \quad v^{(k+1)}_{i,j,k} = v^{(k)}_{i,j,k} + \frac{\Delta t}{\rho}\delta p^{(k)}_{i,j,k}/\Delta y \\
w^{(k+1)}_{i,j,k-1} &= w^{(k)}_{i,j,k-1} - \frac{\Delta t}{\rho}\delta p^{(k)}_{i,j,k}/\Delta z, \quad w^{(k+1)}_{i,j,k} = w^{(k)}_{i,j,k} + \frac{\Delta t}{\rho}\delta p^{(k)}_{i,j,k}/\Delta z
\end{aligned}$$

That algorithm is performed on four grids in a classical multigrid approach (Brandt et al., 1980)

2.3.6. Third-order Runge-Kutta

An explicit third-order Runge-Kutta scheme to integrate a set of differential equations $\dot{u} = f(u)$ over a step Δt is implemented. This low storage algorithm Williamson (1980), is characterized by the coefficients $\alpha_2 = 1/3, \alpha_3 = 3/4, \beta_{32} = 15/16$ and $w_1 = 1/6, w_2 = 3/10, w_3 = 8/15$.

This yields the corresponding algorithm starting from $U^0 = u(t_0)$:

$$\begin{aligned}
Q^1 &= \Delta t f(U^0) & U^1 &= U^0 + \frac{1}{3}\Delta t f(U^0) \\
Q^2 &= -\frac{5}{9}Q^1 + \Delta t f(U^1) & U^2 &= U^1 + \frac{15}{16}\cdot Q^2 \\
Q^3 &= -\frac{153}{128}Q^2 + \Delta t f(U^2) & U^3 &= U^2 + \frac{8}{15}Q^3 = u(t_0 + \Delta t).
\end{aligned}$$

This version of Runge-Kutta iteration requires only three storage arrays and is more accurate than e.g. the Heun algorithm (Williamson, 1980).

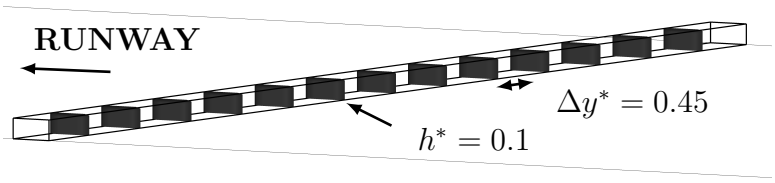

Abbildung 2.15.: Schematic representation of a plate line of $0.2b_0 \times 0.1b_0$ thin plates with $\Delta y^* = 0.45$ separation (Stephan et al., 2013b).

2.3.7. Obstacle modeling

For stability reasons we cannot set the velocity inside the obstacle to zero. Instead the obstacles are modeled by adding a drag force source term $F_{D,i} = C_D|u|u_i$ to the Navier-Stokes equations with a large drag coefficient $C_D = 10/\,\mathrm{m}$. This approach is also used for modeling canopy flows (Shaw & Schumann, 1992), hence we can regard our obstacles as very dense porous media. A possible arrangement of obstacles, a so called plate line which was used in the WakeOP campaign, is depicted in Fig. 2.15.

2.4. LES of Boundary Layer Flow

Wake-vortex flow in ground proximity presents a highly complex turbulent boundary layer flow in terms of structure and relevant scales. The flow around the flying aircraft as well as the fixed ground surface are boundary layer flows at different scales. The use of LES has to be justified on the one hand and applied carefully on the other.

In isotropic space LES present an optimum balance between predictive accuracy and computational cost. The directly resolved motions, the large eddies, constitute the dynamically important parts of the flow, as they possess almost the total kinetic energy. Only motions with small energy at small scales are modeled. For a given flow the increase of Reynolds number changes the flow spectrum mostly at the smallest scales, thus the computational cost is nearly independent of the Reynolds number. This favorable property vanishes when LES is applied to turbulent boundary layer flow, because close to the boundary the large scale motions become less relevant and finally vanish. Consequently the resolution requirements as well as the cost for LES in proximity to no-slip boundaries are close to those for DNS. This is why a simple LES applied on wall-bounded flows at realistically high Reynolds numbers is not feasible in the foreseeable future. However, many engineering problems are high Reynolds number flows, where small turbulent structures originating from rigid walls are dynamically important to the aerodynamics of the vehicle under consideration.

The solution to that kind of multi-scale problem is to model the inner layer rather than to resolve it. This is known for a long time (Schumann, 1975; Deardorff, 1970). A historical overview and recent challenges in modelling wall-bounded turbulence can be found in Smits

& Marusic (2013). Reviews of proposed methods for modeling the inner layer in LES can be found in Piomelli & Balaras (2002); Spalart (2009). These wall-modeling LES methods can be divided into two categories:

- direct models for the wall shear stress τ_w
- methods that switch to a RANS description of the inner layer

The second category includes hybrid LES/RANS and detached eddy simulation (DES). These wall models aim to reproduce certain moments of the flow, like the mean flow or certain predominant scales of the spectrum correctly. In this thesis the inner-layer of the ground surface is either resolved for sufficiently small Reynolds numbers by appropriate mesh refinement close to walls, or a model from the first category is used. The flow around the aircraft is modeled by RANS/LES coupling belonging to the second category.

2.4.1. Resolution requirements and computational complexity

Flow around the aircraft. The resolution requirements of the flow over an airfoil was thoroughly investigated by Chapman (1979). Employing non-equidistant grids he estimates the number of required grid points as $N \sim \mathrm{Re}_c^{1.8}$. This is close to DNS requirements and prevents LES from being used for wall-resolved high Reynolds number airfoil flows. A flying aircraft would require even more grid points as the whole flight path would have to be resolved that way. This problem is tackled with the RANS/LES coupling in this thesis.

Vortex flow with boundary. To define the resolution requirements of the vortex flow, it is approximately considered as a perturbation of an idealized quasi-two-dimensional laminar two vortex flow (case 0) by either turbulent environmental flow i.e. wind or obstacles like plate lines. In the present investigation the resolution requirements strongly depend on the phenomenon that is studied. Wall-resolved LES is used to directly resolve the boundary layer streaks, as they trigger turbulent vortex decay. These investigations are limited by the Reynolds number. Wall-modeled LES can be used in cases, where the turbulent decay is triggered by large structures, like obstacles. This way high Reynolds numbers can be achieved, not compromising the important physics of vortex decay.

The employed mesh spacing equals three-quarters of the spacing used in Misaka et al. (2012a). This mesh resolution guarantees that at least 8 intervals resolve the vortex core and keep it tight in time Stephan et al. (2013a). Secondary vortices generated at the ground are just vertically well-resolved due to mesh stretching. However, they do not require an equivalent resolution as primary vortices, as their lifetime is short and larger vortex core growth rates can be accepted, the emerging velocities are smaller, and we are primarily interested in their interaction with the primary vortices.

The wake vortex evolution and decay in ground proximity depends on the turbulent structures evolving from the ground surface. Thus, the ambient wind flow has to be resolved properly. Following Kolmogorov statistical turbulence theory we can assume for relatively

high Reynolds numbers that small scale turbulent motions are isotropic and the statistics is determined by ν and the eddy dissipation rate

$$\varepsilon = \frac{\nu}{2} \sum_{i,j} \left(\frac{\partial u_i}{\partial x_j} + \frac{\partial u_j}{\partial x_i} \right)^2 .$$

The Kolmogorov length and time scale

$$\eta = \left(\frac{\nu^3}{\varepsilon} \right)^{\frac{1}{4}}, \quad \tau_\eta = \left(\frac{\nu}{\varepsilon} \right)^{\frac{1}{2}}$$

have to be resolved. Near a smooth wall ε reduces to

$$\varepsilon \approx \nu \left(\frac{\partial u}{\partial z}\bigg|_{z=0} \right)^2 = \frac{u_\tau^4}{\nu}.$$

Hence, the resolution requirement for the first grid point z_1 reads as

$$z_1 \approx \eta = \left(\frac{\nu^3}{\varepsilon} \right)^{\frac{1}{4}} \approx \left(\nu^3 \frac{\nu}{u_\tau^4} \right)^{\frac{1}{4}} = \frac{\nu}{u_\tau}, \quad \text{or} \quad z_1^+ = z_1 \frac{u_\tau}{\nu} \approx 1$$

in normalized coordinates. Thus we can conclude from Eq. (2.30) that

$$\frac{\delta}{z_1} = \mathrm{Re}_\tau \, . \tag{2.52}$$

An equidistant mesh resolution would imply that the number of required grid points would go with $N \sim \mathrm{Re}_\tau^3$. The grid employed in the present MGLET version is a Cartesian grid allowing mesh stretching. Since $\Delta x / \Delta z$ should not grow arbitrary large, this reduces the number of grid points by a factor but not the order of Re_τ. In cases where the Reynolds number is too large to perform wall-resolved LES we consequently use a wall model.

2.4.2. Wall model for the ground surface

The aim of this approach is to model the wall shear stress τ_w locally that it can respond to the flow induced by a multi vortex system, i.e. no averaging over the whole domain should be performed. On the other hand, the model should establish realistic velocity profiles in half channel flow. The Grötzbach-Schumann wall model that locally computes τ_w based on the logarithmic law is employed (Grötzbach, 1987). Therefore one of the first grid points above the ground z^* is chosen and the tangential velocity u_{tan} evaluated. τ_w is modeled directly assuming that z^* lies in the logarithmic layer, such that from Eq. (2.32)

$$u_{tan}(z^*) \;=\; \frac{\mathrm{Re}_\tau \, \nu}{\delta} \left(\frac{1}{\kappa} \log \left(\frac{z^* \, \mathrm{Re}_\tau}{\delta} \right) + B \right). \tag{2.53}$$

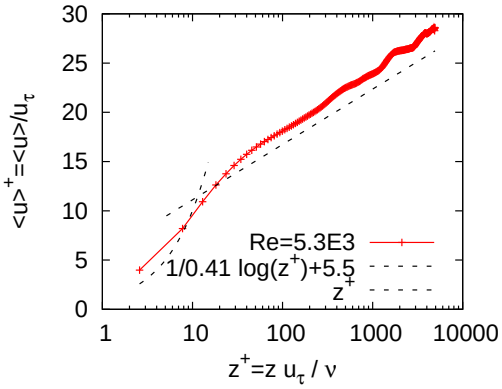

(a) $\mathrm{Re}_\tau = 5300$

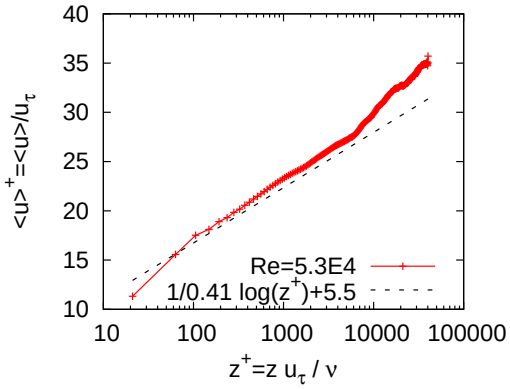

(b) $\mathrm{Re}_\tau = 53000$

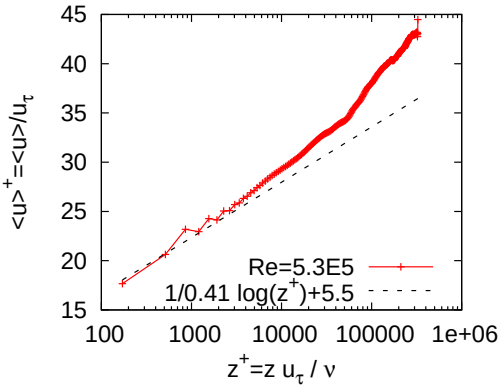

(c) $\mathrm{Re}_\tau = 53000$

Abbildung 2.16.: Mean velocity profiles of half channel flow at different Reynolds numbers applying the Grötzbach-Schumann wall model.

With some Newton iterations Re_τ is calculated from Eq. (2.53) and from Eq. (2.30) the friction velocity and the wall shear stress. Applied to half channel flow this model yields the desired results concerning the mean velocity profile, see Fig. 2.16. Alternatively one could model τ_w independently of Re_τ, assuming a certain wall roughness and employing a logarithmic law for flow over a rough surface (Schmidt & Schumann, 1989; Hultmark et al., 2013), see also Appendix B.

2.5. RANS/LES Coupling

Up to now one of the most challenging problems in computational fluid dynamics dealing with turbulence is the simulation of multi scale flows as they appear in aerodynamics (Samulat, 2013). Calculating full NSE is way to expensive, hence appropriate models are needed for the small scales. LES have proved to be an excellent methodology for (locally)

isotropic, homogeneous space, whereas RANS approximations capture the most important flow features, modes and frequencies around complex geometries. The coupling used in this thesis is an appropriate solution for multi-scale flows with complex geometries. It was developed in Misaka et al. (2012a) for cruise flight and extended for landing aircraft in Stephan et al. (2013b). In Misaka et al. (2012a) a validation of the developed method for a NACA0012 wing with experimental results was performed.

We employ a wake initialization approach where a realistic aircraft wake is generated in a LES domain by sweeping a high-fidelity RANS flow field through the domain. This enables to simulate the wake-vortex evolution from generation until final decay (Misaka et al., 2013). Investigating the aircraft wake in cruise flight the environmental conditions are kept constant. The turbulent rollup process is averaged in time. Hence a steady RANS solution is used for wake initialization. Turbulent fluctuations can be modeled and superimposed into the LES domain (Misaka et al., 2013). The simulations are performed for a large transport aircraft model in high-lift configuration used in ONERA's catapult facility during the European AWIATOR project. The approach developed in Misaka et al. (2012a) is schematically shown in Fig. 2.17. Physically that kind of simulation might be viewed as the realization of a catapult experiment in Coton (1998). Actually, it corresponds well to real flight through a realistic environment. The approach allows the investigation of the aircraft wake from roll-up to far-field, bridging the near-field simulation performed with steady RANS methods to the far-field solution performed with an LES. As the decay of the aircraft wake vortices strongly depends on the environmental conditions like ambient turbulence and temperature gradient it is important to control these parameters in simulations. This approach uses periodic boundaries in horizontal directions. Hence, it allows to include a turbulent environment in a straightforward manner performing a pre-simulation. This has been done for ambient homogeneous turbulence in (Misaka et al., 2012a) and is straight forward for wind turbulence in a boundary layer for landing aircraft. From that viewpoint a ground fixed domain is much more appropriate than an aircraft fixed LES domain employing inflow boundary conditions. Note that an ambient wind would change the inflow condition leading to an adjustment of the steady RANS field, as well as the time step due to a perturbed flight speed.

2.5.1. Fortified solution algorithm

The steady RANS flow field serves as a forcing term of the Navier-Stokes equations in the LES. This approach might be referred to as a fortified solution algorithm (Fujii, 1995), or a nudging technique used in data assimilation (Kalnay, 2003). The resulting velocity field in the aircraft vicinity consists of the weighted sum

$$\mathbf{V} = f(y)\mathbf{V}_{\mathrm{LES}} + (1 - f(y))\mathbf{V}_{\mathrm{RANS}} \tag{2.54}$$

of the LES and the RANS velocity field, see Fig 2.18, with a transition function

$$f(y, \alpha, \beta) = \frac{1}{2}\left[\tanh\left[\alpha\left(\frac{y}{\beta} - \frac{\beta}{y}\right)\right] + 1.0\right]. \tag{2.55}$$

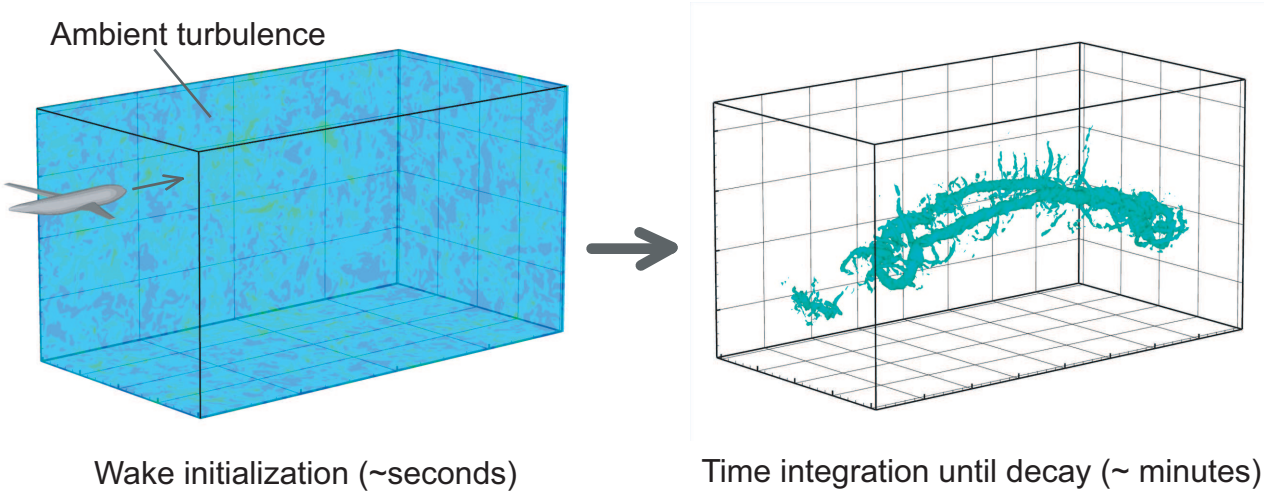

Abbildung 2.17.: Schematic of the approach developed in (Misaka et al., 2012a), (a) wake initialization on the order of seconds, (b) wake evolution on the order of several minutes until vortex decay.

Here α and β represent slope and wall-distance of the transition, respectively. In the simulations $\beta^* = 0.08$ and $\alpha^* = 0.56$ is chosen, similar to the value in Misaka et al. (2013).

2.5.2. RANS/LES interface

The fortification of the steady RANS solution into the LES domain in Misaka et al. (2013) is technically realized such that a parent coarse grid contains the information of the LES solution fields and a moving fine child grid contains the near-field information. The fine mesh spacing $\Delta x_f, \Delta y_f, \Delta z_f$ is half of the coarse mesh spacing $\Delta x_c, \Delta y_c, \Delta z_c$ in each spatial direction. The moving is realized by two near-field data sets shifted by Δx_f in flight direction. The two sets are mapped alternately to the coarse grid using the mapping function and moved by one Δx_c in flight direction. This determines the time step to be $\Delta t = \Delta x_f / U$, where U is the flight speed. The mapping of velocity and pressure fields obtained from the RANS flow field from an unstructured, mesh refined grid, Fig. 2.19, to the structured LES domain is performed by a linear interpolation before the wake initialization. Hence, few additional computational power is required, but depending on the size of the mapped domain we have an increase in memory.

For landing this approach was developed further enabling downward (or upward) sloping trajectories. Again a steady RANS flow field is used neglecting the influence of the ground surface for the near field. The present approach is shown schematically in Fig. 2.20. As before two grid sizes are used. The moving of the finer mesh, containing the near-field information is now realized by $2n$ sets of data. The k-th data set is shifted $k\Delta x_f$ in flight direction and $\frac{k}{n}\Delta z_f$ down. They are mapped alternately and now moved $n\Delta x_c$ in flight

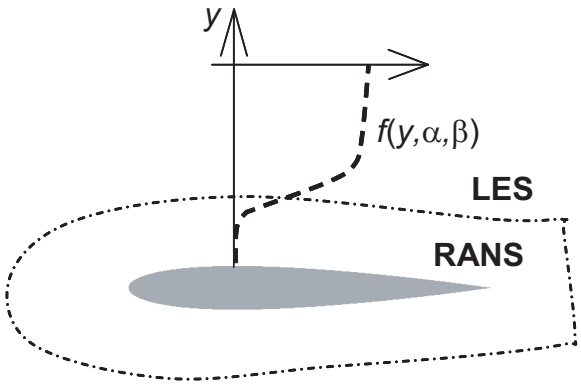

Abbildung 2.18.: Schematic of a weighting function for a combination of RANS and LES flow fields (Misaka et al., 2013).

direction and one Δz_c down. Thus, the data sets interpolate the aircraft's flow field on a downward sloping straight line with a slope angle of

$$\gamma = \arctan\left(\frac{\Delta x_c}{n\Delta z_c}\right). \tag{2.56}$$

The $2n$ data sets are used to provide a complete period of the flow field of a uniformly descending aircraft. Certainly, every flight path angle can be implemented choosing appropriate values for the ratio $\Delta x_c/\Delta z_c$ and a number n, which will require $2n$ sets of data. Thus n determines the additional amount of required memory. However, for numerical reasons $\Delta x_c/\Delta z_c$ should not be too small and n can not be chosen arbitrary large. Thus the flight path angle can not be chosen arbitrary small. As the flight speed U is fixed this determines Δt_γ to be

$$\Delta t_\gamma = \sqrt{\Delta x_f^2 + \left(\frac{\Delta z_f}{n^2}\right)^2}, \tag{2.57}$$

for landing configuration.

2.5.3. Aircraft descent and touchdown

In the thesis realistic descent angles are realized. In the simulations the aircraft approaches the ground with an angle of 3.57 degree, slightly larger than the standard glide path angle of 3 degree. Thirty-two RANS fields are used alternately in an equidistant mesh with $\Delta x_c = \Delta z_c$. In addition the wall-distance parameter $\beta = 0.08$ is gradually reduced depending on the distance to the ground to $\beta = 0.013$. This way the LES takes account for the wing-in-ground effect which is not considered in the steady RANS solution. At the instant of touchdown the lift ceases quickly, when the bound vortex as well as the wake vortices quickly vanish. After touchdown the aircraft wake can be regarded as white

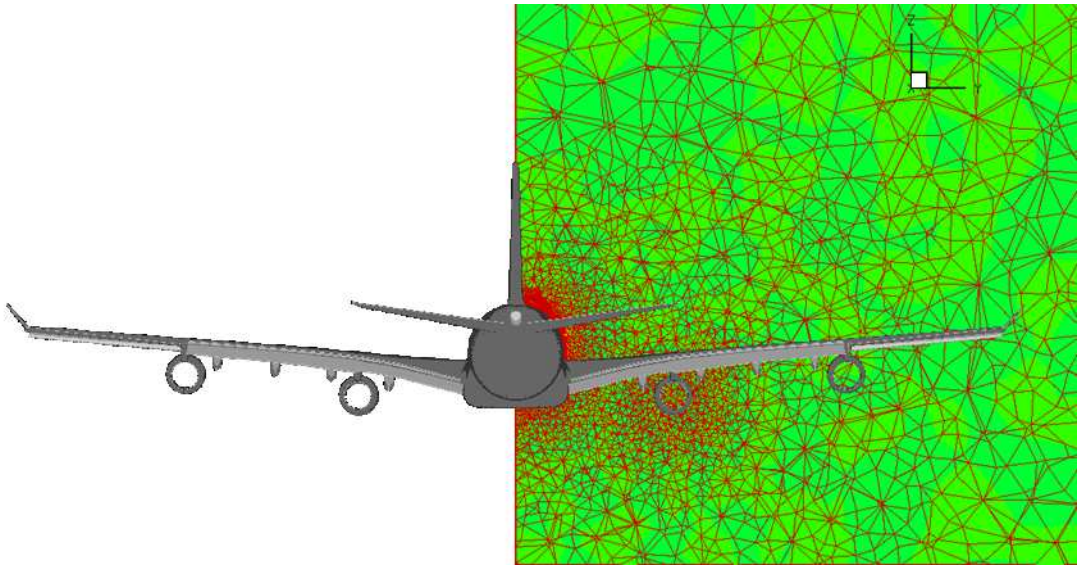

Abbildung 2.19.: Unstructured mesh refined grid used for the RANS simulation of the near-field by Stefan Melber.

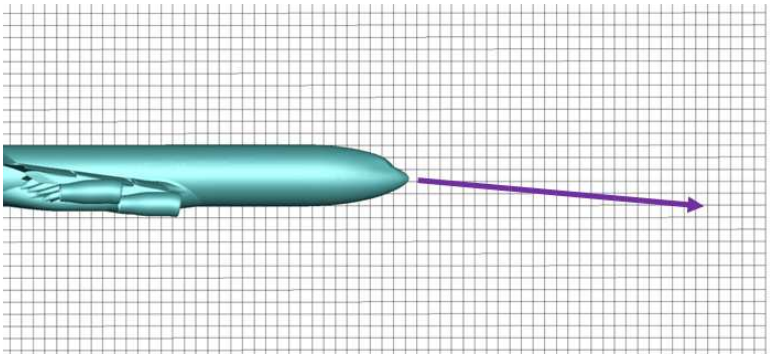

Abbildung 2.20.: Schematic of the descent realization.

noise (Hah & Lakshminarayana, 1982) which is not taken into account in the simulations. We model the touchdown just by removing the RANS flow field forcing term from the simulation. This approach leaves the bound vortex in the computational domain at the point of touchdown. Alternatively the strength of the remaining vortex was varied. This small study has shown that the evolution of the wake vortices does not depend very much on the bound vortex strength remaining at the point of touchdown. This can be explained by the rapid vortex ground interaction very close to the ground leading to an annihilation of the bound vortex.

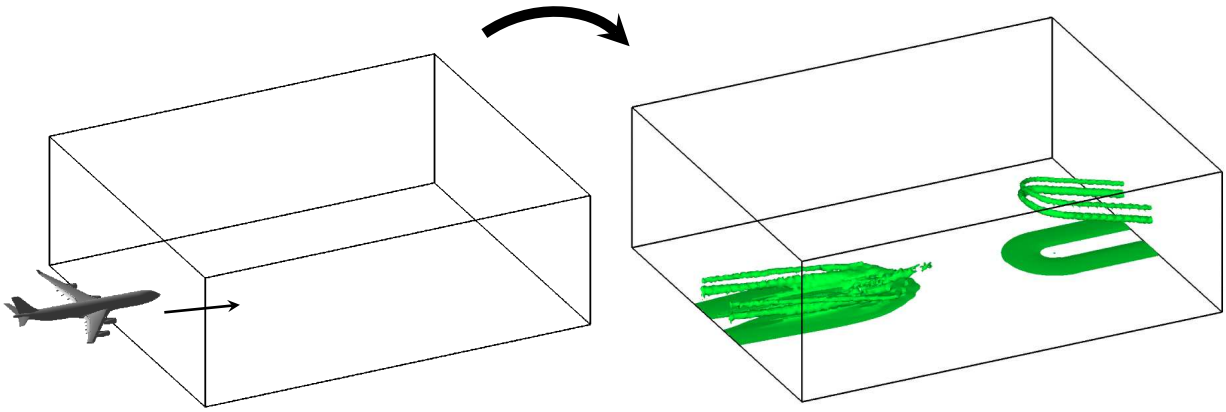

(a) Wake initialization until touchdown. (b) LES, vortex decay after touchdown.

Abbildung 2.21.: Schematic of aircraft landing, (a) wake initialization, (b) artificial vortex reconnection and wake evolution after touchdown (Stephan et al., 2013b).

2.5.4. Boundary treatment

We employ periodic boundary conditions in horizontal directions, a no-slip condition at the ground and a free-slip condition at the top side. The aircraft starts in the back part of the domain passes the boundary and approaches the ground. After touchdown the first slice of the domain is prolonged into the back part continuing the remainder vortex which is closed artificially to a half ring, Fig. 2.21 (b). This procedure is effectively avoiding disturbances generated at the starting point of vortex initialization. Note, that wake vortex linking due to Crow instability is frequently observed in cruise altitudes and may also occur in ground proximity.

2.6. Turbulence Initialization

2.6.1. Wind initialization

For a fixed molecular viscosity ν_{mol} and channel half height δ the averaged wind profile depends on one parameter, e.g the intrinsic Reynolds number Re_τ, or with Eq. (2.31) the pressure gradient. For initialization we fix a pressure gradient such that the time-averaged stream-wise velocity of the wind at the initial vortex height is a certain multiple of w_0, the initial vortex descent speed. This leads to

$$\overline{u}(b_0) = cw_0 = \frac{\text{Re}_\tau\,\nu}{\delta}\left(\frac{1}{\kappa}\log\left(\frac{z\,\text{Re}_\tau}{\delta}\right) + B\right), \tag{2.58}$$

which can be solved by some Newton iterations. To establish the turbulent wind we apply a pressure gradient and initialize a velocity field

$$u^+(z^+) = \begin{cases} z^+ & \text{for} \quad z^+ \leq 11.445 \\ \frac{1}{\kappa}\log(z^+) + B & \text{otherwise} \end{cases} \tag{2.59}$$

with random fluctuations added.

We let the flow develop until characteristic wall streaks appear and an equilibrium between the pressure gradient and the wall friction is established. Averaged wind profile $\overline{u}^+$ and velocity fluctuations $\overline{uu}^+, \overline{vv}^+, \overline{ww}^+$, see Fig. 2.11, converge to the typical half channel flow characteristics (Moser et al., 1999).

2.6.2. Strut wake initialization

The wake of the strut for the comparison with towing tank experiments is simulated in separate simulations before vortex initialization. For this purpose an isotropic turbulence field is generated, based on the stochastic noise generation approach using the von Karman and Pao spectrum (Béchara et al., 1994) in a separate simulation. An overview of the fundamental properties describing isotropic turbulence can be found in Rotta (1972). The energy spectrum is initialized using the results from Zhang et al. (2004). The LES of decaying turbulence is performed in a $2b_0^3$ domain until the eddy dissipation rate reaches its maximum value in time. At that time, the energy density spectrum, depicted in Fig. 2.22, has formed a $-5/3$ slope. The isotropic turbulence field is weighted using the similarity profiles given in Eq. (2.36). The maximum value of u_{rms} is scaled from the experiment to LES assuming that the ratio of the turbulent kinetic energy in the strut wake and in the two wake vortices is constant.

$$\frac{E_{strut}}{E_\Gamma} = const. \tag{2.60}$$

The kinetic energy per distance of Lamb-Oseen vortices in the case that $r_c/b_0 < 0.2$ can be computed by (de Bruin & Winckelmans, 2005):

$$\frac{E_\Gamma}{dx} = \frac{\rho\Gamma^2}{2\pi}\left\{\log\left(b_0/r_c\right) + 0.0562\right\}. \tag{2.61}$$

Computing the turbulent kinetic energy per distance in the strut wake one has with (2.36)

$$\begin{aligned}\frac{E_{strut}}{dx} = \int_0^{l_{strut}}\int_{-\infty}^{\infty}\frac{3}{2}\rho u_{\mathrm{rms}}^2 dydz &= l_{strut}\rho\frac{3}{2}u_{\mathrm{rms,max}}^2\int_{-\infty}^{\infty}e^{\left(-\frac{1}{2}\left(\frac{y}{\sigma}\right)^2\right)}dy \\ &= \frac{3}{2}\sqrt{2\pi}l_{strut}\sigma\rho u_{\mathrm{rms,max}}^2.\end{aligned} \tag{2.62}$$

The strut length l_{strut} is scaled with the vortex separation b_0. From (2.60)-(2.62) a relation for the turbulence levels is derived

$$\frac{\sigma_L\rho_L b_{0,L}u_{\mathrm{rms,max},L}^2}{\sigma_W\rho_W b_{0,W}u_{\mathrm{rms,max},W}^2} = \frac{\rho_L\Gamma_L^2\left\{\log\left(b_{0,L}/r_{c,L}\right)+0.0562\right\}}{\rho_W\Gamma_W^2\left\{\log\left(b_{0,W}/r_{c,W}\right)+0.0562\right\}}, \tag{2.63}$$

in the LES (index L) and WSG (index W).

Tabelle 2.1.: Initial parameters in the experimental and numerical set-up

	Re_Γ	Γ_0 [m^2 / s]	b_0 [m]	w_0 [m / s]	ρ [kg / m^3]	$r_{c,0}$ [m]
WSG	52 000	0.052	0.153	0.049	1000	0.09
LES	23 130	530	47.1	1.79	1.2	3

For initializing turbulence it is assumed that the standard deviations of the similarity profiles in Eq. (2.36) scale with b_0.

$$\frac{\sigma_W}{\sigma_L} = \frac{b_{0,W}}{b_{0,L}}$$

which yields

$$u_{\mathrm{rms,max},L} = u_{\mathrm{rms,max},W} \frac{\Gamma_L / b_{0,L}}{\Gamma_W / b_{0,W}} \sqrt{\frac{\log(b_{0,L}/r_{c,L}) + 0.0562}{\log(b_{0,W}/r_{c,W}) + 0.0562}} \tag{2.64}$$

Hence, the maximal u_{rms} values scale approximately with the vortex descent velocities times a coefficient depending on the vortex dimensions. The above calculated u_{rms} values and the initial parameters listed in Table 2.1 yield $u_{\mathrm{rms,max},L} = u_{\mathrm{rms,max},W} * 35.5$. For turbulence initialization in the LES $x' = 30$ is chosen, corresponding to $\sigma'_W(30) = 0.245, \sigma_L = 0.38\,\mathrm{m}$ and $u_{\mathrm{rms,max},L} = 0.0163\,\mathrm{m/s} * 35.5 = 0.58\,\mathrm{m/s}$. Finally, the turbulence field is mapped periodically to the simulation domain according to Eq. (2.36).

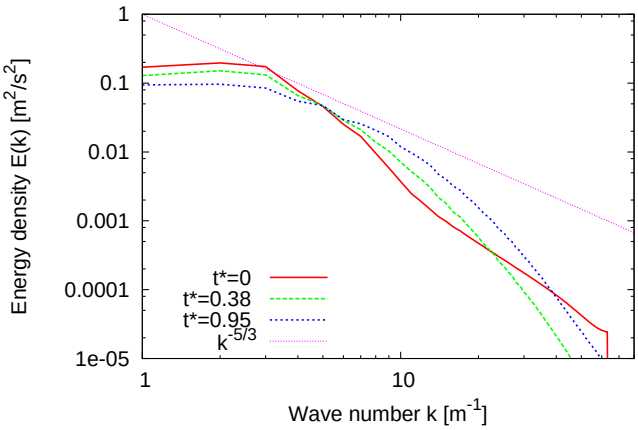

Abbildung 2.22.: Energy density spectra established during separate simulation (Stephan et al., 2013c).

2.7. Wake-Vortex Initialization

For the initialization of the aircraft's wake two different approaches have been developed and successfully applied to study various questions concerning wake vortices. Over the last decades in LES the aircraft's wake was modeled by a pair of fully rolled-up vortices, initialized constantly in flight direction. This so-called *temporal LES* approach allows the evolution of the wake vortices in space and time but the vortex age is constant in the whole simulation domain. This is a good approximation for the vortex phase and the decay phase and numerous insights have been gained by this approach concerning these phases. The initial velocity field consists of the superposition of two modeled vortices with opposite circulation. Different vortex models are used in literature (Gerz et al., 2002), e.g. the *Lamb-Oseen vortex* as an exact solution of the NSE (Lamb, 1932) used in Holzäpfel et al. (2001), or others (Proctor et al., 2000; Jacquin et al., 2001). All vortex models have different advantages, however certain assumptions have to be met in this approach. As for example an elliptical wing loading is assumed if we employ the Lamb-Oseen vortices.

Secondly, the above described *spatial LES* incorporating the RANS/LES coupling was presented by Misaka et al. (2012a) where the vortices feature a spatial gradient of vortex age and structure in flight direction. In this thesis, LES with both methods of vortex initialization are performed. This is due to the fact that the spatial LES for landing aircraft was developed in the last phase of the dissertation. However, the temporal LES are well justified for phenomena that exclude touchdown effects.

2.7.1. Temporal LES

The fully rolled-up wake vortices are initialized by superposition of a pair of counter rotating Lamb-Oseen vortices with a circulation of $\Gamma_0 = 530\,\mathrm{m}^2\,/\,\mathrm{s}$, a vortex core radius of $r_c = 3.0\,\mathrm{m}$ and a vortex separation $b_0 = 47.1\,\mathrm{m}$, which are representative values for a generic heavy aircraft (Gerz et al., 2002). We employ a relatively large core radius of 6.4% of b_0, because in numerical simulations regions with steep velocity gradients have to be resolved well to limit numerical dispersion (Holzäpfel, 2004). General vortex behavior is little affected by the relatively coarse initial core radius. This is a highly idealized model, because aircraft in landing configuration with flaps and slats deployed generate complex wakes consisting of at least four vortices. Depending on the aircraft type vortex separation in high-lift configuration may be smaller than it may be expected for elliptical wing loading Delisi et al. (2013). The initial height of the vortex pair is set to $h_0 = b_0$. The Reynolds number is set to $\mathrm{Re}_\Gamma = \Gamma_0/\nu = 23\,130$. The molecular viscosity of air of $13.5 \cdot 10^{-6}\ \mathrm{m}^2\,/\,\mathrm{s}$ corresponds to a Reynolds number of $3.9 \cdot 10^7$. The velocity scale is based on the initial descent speed of the vortex pair $w_0 = \Gamma_0/2\pi b_0 = 1.79\,\mathrm{m}\,/\,\mathrm{s}$. This defines the non-dimensional time $t^* = t\frac{w_0}{b_0}$ with $t_0 = b_0/w_0 = 26.3\,\mathrm{s}$ and non-dimensional vorticity $\omega^* = \omega t_0$. Lengths are non-dimensionalized by b_0 and velocities by w_0 if marked with an asterisk. For prescribing the initial vortex velocity field six image vortex pairs in spanwise direction and two mirror vortices in the direction perpendicular to the ground are taken into account, Fig. 2.23.

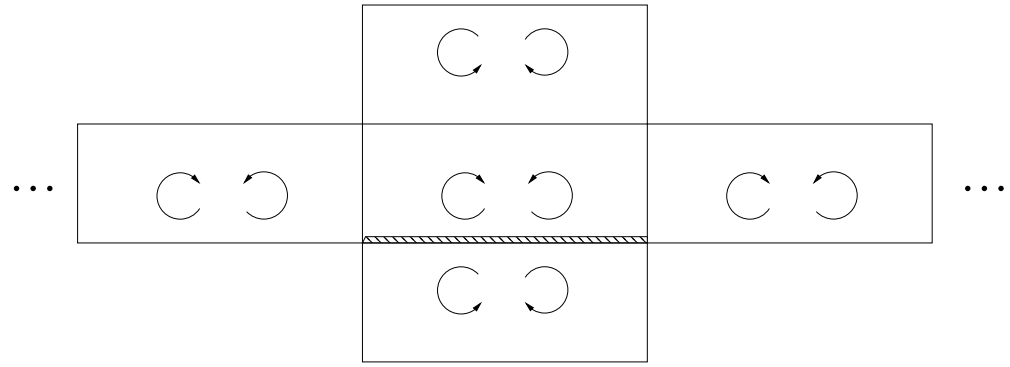

Abbildung 2.23.: Schematic of the wake vortex initialization employing mirror and image vortices.

2.7.2. Spatial LES

We employ a RANS flow field obtained by the DLR TAU-code with an adaptive mesh refinement for wingtip and flap vortices as well as the fuselage wake (Schwamborn et al., 2006; Keye, 2011). The RANS simulations have been performed at the DLR Braunschweig and were kindly provided by Stefan Melber. The flow conditions of the RANS simulation are the same as in ONERA's catapult facility experiment, i.e. Reynolds number $\mathrm{Re}_c = 5.2 \cdot 10^5$, free stream velocity respectively flight speed $U = 25\,\mathrm{m}\,/\,\mathrm{s}$, and a lift coefficient of $C_L = 1.4$. The 1/27 scaled model has a wingspan of 2.236 m. We normalize quantities with the following reference values, initial circulation, vortex spacing, vortex descent velocity, and characteristic time, for an elliptic load distribution (Gerz et al., 2002),

$$\Gamma_0 = \frac{2C_L U b}{\pi \Lambda}, \quad b_0 = \frac{\pi}{4} b, \quad w_0 = \frac{\Gamma_0}{2\pi b_0}, \quad t_0 = \frac{b_0}{w_0} \tag{2.65}$$

with a wing aspect ratio of $\Lambda = 9.3$. The resulting reference values for the normalization are $\Gamma_0 = 5.36\,\mathrm{m}^2\,/\,\mathrm{s}$ for circulation, $b_0 = 1.756$ for length, $w_0 = 0.49\,\mathrm{m}\,/\,\mathrm{s}$ for velocity, and $t_0 = 3.617\,\mathrm{s}$ for time. The associated vortex flow Reynolds number equals $\mathrm{Re}_\Gamma = 3.0 \cdot 10^5$. We set $t = 0$ at the instant of the touchdown. During landing the angle of attack of the fuselage is fixed to 5.54 degree.

2.7.3. RANS flow field

From (Misaka et al., 2013) the main properties of the steady RANS flow field are recapitulated. The near-field distribution of axial vorticity is depicted in Fig. 2.24. Blue colors represent clockwise and red counter-clockwise vorticity, respectively. The complex flow structures of the wake behind the wing roll up and constitute three main vortices, wing-tip and flap-tip vortices, which are the immediate consequence of lift as well as the vortices from the wing-fuselage junction with opposite rotational direction, possessing undesirable aerodynamic flow features (Yi & Kim, 2013). The flap vortex results after merging of two

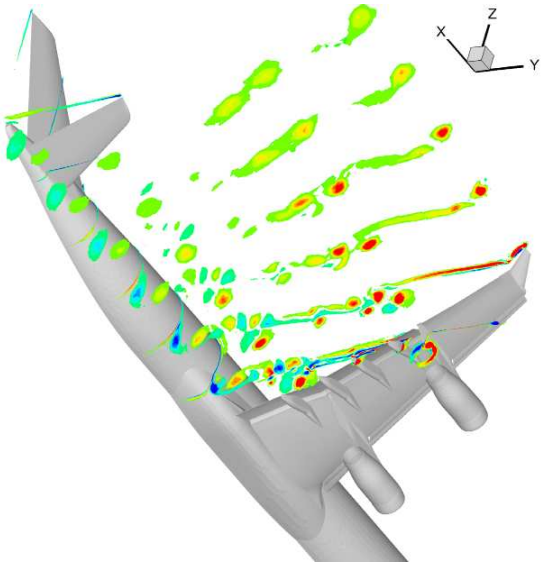

Abbildung 2.24.: Near-field vorticity distribution around AWIATOR long range aircraft obtained from a RANS simulation by Stefan Melber, (Misaka et al., 2013).

vortices from the outer edge of the flap at a time of $t^* = 0.021$. Another isolated vortex is observed rotating around the primary co-rotating vortices stemming from the inner engine pylon.

2.8. Computational Domain

2.8.1. Temporal LES

In the temporal LES we use two different domain sizes. The dimensions are either $L_x = 192\,\mathrm{m}$, $L_y = 384\,\mathrm{m}$, $L_z = 144\,\mathrm{m}$ (Fig. 2.25) or $L_x = 384\,\mathrm{m}$, $L_y = 288\,\mathrm{m}$, $L_z = 96\,\mathrm{m}$. This corresponds to approximately $4b_0 \times 8b_0 \times 3b_0$ or $8b_0 \times 6b_0 \times 2b_0$, respectively. We impose periodic boundary conditions in the flight direction x and the spanwise direction y. A no-slip condition is set at the ground at $z = 0$ and a free slip condition at the top at $z = z_{\max}$. The number of grid points are $N_x = 256, N_y = 512, N_z = 256$ or $N_x = 512, N_y = 384, N_z = 192$, respectively, leading to a total of 33.5 and 37.7 million grid points. We employ a horizontally equidistant mesh. In vertical direction the mesh is stretched geometrically up to a height of b_0 and then is continued equidistantly until the top of the domain. We impose obstacles at the ground surface with square-shaped and rectangular cross section of $9\,\mathrm{m} \times 9\,\mathrm{m}$, $9\,\mathrm{m} \times 4.5\,\mathrm{m}$ or plate lines in order to trigger the formation of secondary vorticity structures (SVS) and to achieve early vortex decay.

Two different domain sizes are used to investigate different effects in order to save com-

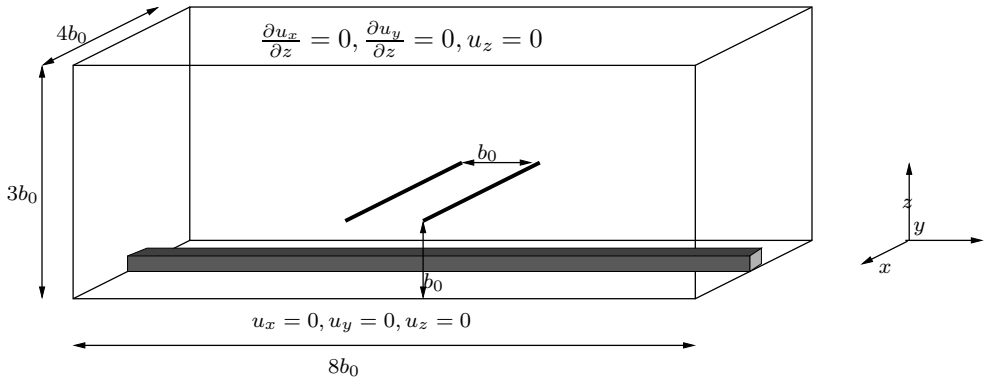

Abbildung 2.25.: Schematic of the computational domain showing the initial vortex position and an obstacle.

putational costs. The first one focuses on the effect of crosswind and the interaction of the obstacle with the wake vortices. Only for relatively small times the obstacle can be regarded as solitary. After the disturbances have reached the boundary the setting is representing the effect of periodically arranged obstacles. The second domain nearly covers a Crow wave length of $8.4b_0$ and allows investigating obstacle effects for larger times, until again periodic obstacle effects appear.

2.8.2. Spatial LES

In the spatial LES we employ uniform mesh spacing for all three spatial directions, with a resolution of $\Delta^* = dx^* = dy^* = dz^* = 0.011$, comparable to mesh spacing in Misaka et al. (2013). Hence, the out of ground effect behavior of the wake vortices should be similar to Misaka et al. (2013). This includes the evolution of the vortex position in space, as well as vortex strength and decay in a non-turbulent environment. It should be mentioned that the vortex core size is affected by the mesh resolution, as it contains the largest velocity gradients in the whole domain. The slightly coarser mesh resolution employed here leads to a slightly larger vortex core size. The numerical dissipation of the LES code leads to non-physical core growth rates. However, this does not prevent us of detecting exceptional physical vortex core behavior like sudden vortex core growth or vortex core shrinking.

Two different domains are used for each simulation. The first one is used for the vortex initiation phase. The dimensions of the complete computational domain are $23.3b_0$, $5.8b_0$, and $2.2b_0$ in flight, spanwise and vertical directions, respectively. After touchdown a larger domain is used for the simulation of the vortex decay due to the strong divergence of the vortices. The dimensions are $23.3b_0$, $8.7b_0$, and $2.2b_0$. The number of grid points are $N_x = 2048, N_y = 512, N_z = 192$ during wake initialization and $N_x = 2048, N_y = 768, N_z = 192$ after touchdown, leading to a total of 201 and 302 million grid points, respectively. The back part of the domain with a length of $5b_0$ is used to launch the aircraft and the half ring closing as boundary treatment compliant with Helmholtz's third vortex theorem stating

that a vortex tube cannot end within a fluid (Kundu & Cohen, 1990). At touchdown the tail wing is at $x^* = 16.3$, the plate line is centered at $x^* = 5.1$, see also Fig. 2.15.

2.9. Post-Processing

Knowledge and prediction of the position and the strength of the wake vortices is an essential skill of a for a WVAS (Holzäpfel et al., 2009; Hennemann & Holzäpfel, 2011). With different post-processing algorithms the turbulent flow field is evaluated. A special post processing routine was written to evaluate the initial wind turbulence. Other routines analyze the vortex flow. First the vortex center line of the primary and secondary vortices is tracked in the pressure and velocity solution fields using different techniques detailed in Sec. 2.9.1. Having identified the vortex center line, averaged as well as slice wise vortex positions, rebound height, lateral transport as well as vortex separation of the primary vortices are determined. Then, parameters revealing the vortex strength, mainly circulation $\Gamma_{5-15}, \Gamma_{\max}, \Gamma_5$ but also turbulent kinetic energy, are evaluated. The core radius is evaluated and averaged.

The post-processing is performed in slices perpendicular to the flight direction separately for every time step. In temporal LES also as averages in flight direction. In most of the situations in ground proximity the deformation of the primary vortices is not too strong. The tracking algorithms work well in principle, however in regions of strong vortex curvature evaluated quantities, might be spurious. Particularly vortex circulation is underestimated there, thus the results have to be interpreted carefully. Methods for investigating complex vortex topologies like vortex rings and strongly pronounced Crow instabilities are presented in Hennemann & Holzäpfel (2011).

Especially the tracking of the secondary vortices turns out to be very difficult. Firstly these become turbulent very fast. Secondly the primary vortex stretches and tilts the secondary vortices in a way that the center line gets curved developing loops end bumps, as it will be explained later. As a consequence it is getting impossible to distinguish them from the ambient turbulent flow field.

2.9.1. Vortex center tracking

For the investigation of turbulent flows, particularly separated flows, the identification of vortices and vortex center lines is highly important. Recognizing coherent structures in turbulent motions reveals important insights into the physics, the mass and heat transfer and the dissipation of the flow (Jeong & Hussain, 1995). Different physical parameters for vortex tracking are used in literature (Chong et al., 1990; Jeong & Hussain, 1995; Sujudi & Haimes, 1995). Beside obvious criteria like vorticity strength and pressure minimum they use helicity, streamlines or eigenvalues of the velocity gradient matrix. The more sophisticated methods are especially useful in highly turbulent flows with weak coherent structures. A detailed investigation of the appropriate physical quantities to detect wake vortices in turbulent environment can be found in Hennemann (2010). According to outcomes of this

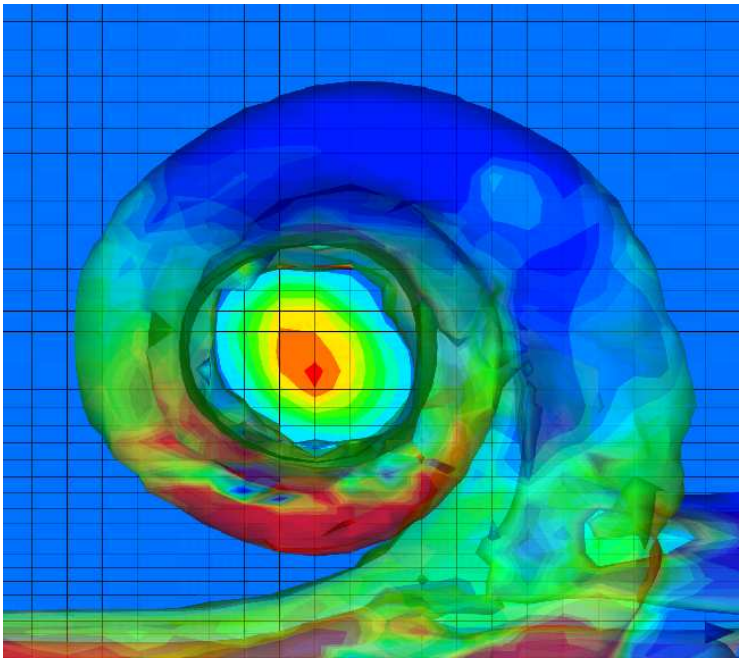

Abbildung 2.26.: Determination of secondary vortex helix parameters, circulation Γ_{hel}, ring radius R_{hel}, and core radius a_{hel}. Axial vorticity and iso-surface of vorticity magnitude (translucent).

work we use a combination of vorticity and pressure.

The primary and secondary vortices are tracked detecting global extreme values of $\omega_x \cdot p^\kappa$, $\kappa > 0$. Here κ serves as weighting coefficient. For $\kappa > 1$ p dominates and for $\kappa < 1$ the influence of the vorticity magnitude is increased. To reduce the disturbance by turbulent fluctuations $\omega_x \cdot p^\kappa$ is averaged within a box. This method is refined including spatial and temporal constraints, i.e. it is assumed, that the vortex core center varies in space and time within a certain bound $b_0/3$ for a primary vortex of interest. This way fluctuations occurring at the other vortex and disturbing the tracking are excluded. The stretched and tilted secondary vortices in a turbulent environment can vary very much in space and time. Hence, they can be tracked only for a short time after they appear at the ground surface.

2.9.2. Secondary vortex helix

For investigating the speed of the secondary vortex helix, initiated by plate lines and block-shaped obstacles the exact position and circulation values at different parts of the helix are needed, Fig. 2.26. Here the center of the helical secondary vortex is tracked in each slice. The point with a maximum surrounding circulation of opposite sign to the primary vortex around a circle of a relatively small radius is determined.

3. Results

3.1. Listing of Simulations

A listing of the conducted simulations presented in the thesis is given in Table 3.1. Cases 0 to 8 are temporal LES. Case 0 serves as a purely academic study to point out the pure viscid interaction of a vortex pair with a flat ground surface, see Sec. 3.3.1. In Sec. 3.3.2 we present simulation results of wake vortex decay mechanisms in the situation of a flat ground with the influence of an ambient crosswind (case 1). The effect of the Grötzbach-Schumann wall model and an increased Reynolds number is investigated in Sec. 3.3.4 (case 2). In Sec. 3.4 we study the effect of an obstacle and how it enhances wake vortex decay by comparing case 1 and case 3. We describe the underlying vortex dynamics, Sec. 3.4.1 and quantify the accelerated decay, Sec. 3.4.2. Further (case 4) we study the simplified setup of case 3 without environmental turbulence but an axially doubled domain, to point out the flow field characteristics and investigate the disturbances. Case 5 is also only used as a reference case for towing tank experiments with flat ground see Sec. 4.1. In Sec. 3.4.3 we examine different obstacle geometries in order to optimize them with respect to size and shape (cases 6 and 7) and the influence of headwind (case 8).

Case 9 and 10 present spatial LES, Sec. 3.5 - 3.8. Flat ground is employed in case 9 and a plate line case 10. The height h_0 in Table 3.1 denotes the entrance height of the aircraft into the computational domain. The altitude above the plate line amounts to $0.88b_0$. Here the largest Re_Γ is employed, using the wall model for the ground surface.

Tabelle 3.1.: Performed LES. Parameters of the numerical setup.

	case	domain	obstacle	amb. turb.	h_0	Re_Γ
temporal LES	0	$4b_0 \times 8b_0 \times 3b_0$	flat ground	no turb	b_0	$2.313 \cdot 10^4$
	1	$4b_0 \times 8b_0 \times 3b_0$	flat ground	crosswind	b_0	$2.313 \cdot 10^4$
	2	$4b_0 \times 8b_0 \times 3b_0$	flat ground	crosswind	b_0	$2.313 \cdot 10^5$
	3	$4b_0 \times 8b_0 \times 3b_0$	$0.2b_0 \times 0.2b_0$ block	crosswind	b_0	$2.313 \cdot 10^4$
	4	$8b_0 \times 6b_0 \times 2b_0$	$0.2b_0 \times 0.2b_0$ block	no turb	$b_0/2$	$2.313 \cdot 10^4$
	5	$8b_0 \times 6b_0 \times 2b_0$	flat ground	strut wake	$b_0/2$	$2.313 \cdot 10^4$
	6	$8b_0 \times 6b_0 \times 2b_0$	$0.2b_0 \times 0.1b_0$ block	no turb	b_0	$2.313 \cdot 10^4$
	7	$8b_0 \times 6b_0 \times 2b_0$	$0.2b_0 \times 0.1b_0$ plates	no turb	b_0	$2.313 \cdot 10^4$
	8	$8b_0 \times 6b_0 \times 2b_0$	$0.2b_0 \times 0.1b_0$ plates	headwind	b_0	$2.313 \cdot 10^4$
sLES	9	$23.3b_0 \times 8.7b_0 \times 2.2b_0$	flat ground	no turb	$1.2b_0$	$3.0 \cdot 10^5$
	10	$23.3b_0 \times 8.7b_0 \times 2.2b_0$	$0.2b_0 \times 0.1b_0$ plates	no turb	$1.2b_0$	$3.0 \cdot 10^5$

3.2. Flow Field of a Landing Aircraft

Firstly the flow field of the complete landing phase including approach, flare, touchdown, and roll-out is presented. Later the distinct stages of the flow are investigated separately.

3.2.1. Complete landing

According to Misaka et al. (2013) the wake behind the aircraft wings consists of a complex vorticity distribution in the near-field, see Fig. 3.1 and Fig. 3.2. However, only a few vortices remain behind the tail wing, wing-tip and flap-tip vortices, as well as vortices from the wing-fuselage junction, clearly visible in Figs. 3.1 (a)-(d). Out of ground proximity wing-tip and flap-tip vortices merge at a distance of about $x^* = 13$ from the aircraft, Fig. 3.1 (c). The wake vortices as well as the bound vortex induce a vorticity layer of opposite sign at the ground surface, first the wake vortices and later the bound vortex at the aircraft wings, Figs. 3.1 (a),(b). The effect of the plate line disturbing the secondary vorticity layer is visible in Fig. 3.1 (c). Shortly after touchdown the bound vortex vanishes and the free ends of the wake vortices start to interact with the vorticity layer at the ground, disturbing the wake vortices starting from the point of touchdown. This process constitutes the end effects propagating as a combination of helical disturbances of the vortex cores and a pressure jump along the wake vortices, see Figs. 3.2. Close to the ground the primary vortices induce secondary vortex structures at the ground, which separate from the ground and wrap around the primary vortices, Figs. 3.1 (e)-(h). Port- and starboard-vortices are no longer linked by the bound vortex and quickly diverge at the point of touchdown, Figs. 3.1 (e)-(h).

Additionally we observe a linking of the vortex ends with the ground. The secondary vorticity layer induced by the descending wake vortices at the ground rolls up to secondary vortex structures as detailed in Stephan et al. (2013a). Due to the low flight height this process starts first at touchdown and then above the plate line, Figs. 3.1 (f),(g). At the plate line secondary vortex structures wind around the primary vortices and propagate by self-induction in axial directions to both sides. These helical disturbances finally interact with the end effects.

The turbulent wake generated by the fuselage, Figs. 3.1 (a)-(c), is stretched around the primary vortices and is quickly transported to the ground between the vortex pair disturbing the relatively smooth shape of the secondary vorticity layer, Figs. 3.1 (e)-(h). Hence, the secondary vortices are disturbed in their development generating irregularities. The counter-rotating secondary vortices finally develop into relatively strong turbulent structures initiating rapid vortex decay of the primary vortices, see Stephan et al. (2013a).

Fig. 3.2 additionally highlights the flare and touchdown phase. Note that the merger of flap-tip and wing-tip vortex to a single vortex pair is fairly accelerated very close to the ground, see Fig. 3.2 (b). The secondary vortex structures interact with the remaining bound vortex. Levels of high vorticity magnitude dissolve starting at the point of touchdown, see Fig. 3.2 (c).

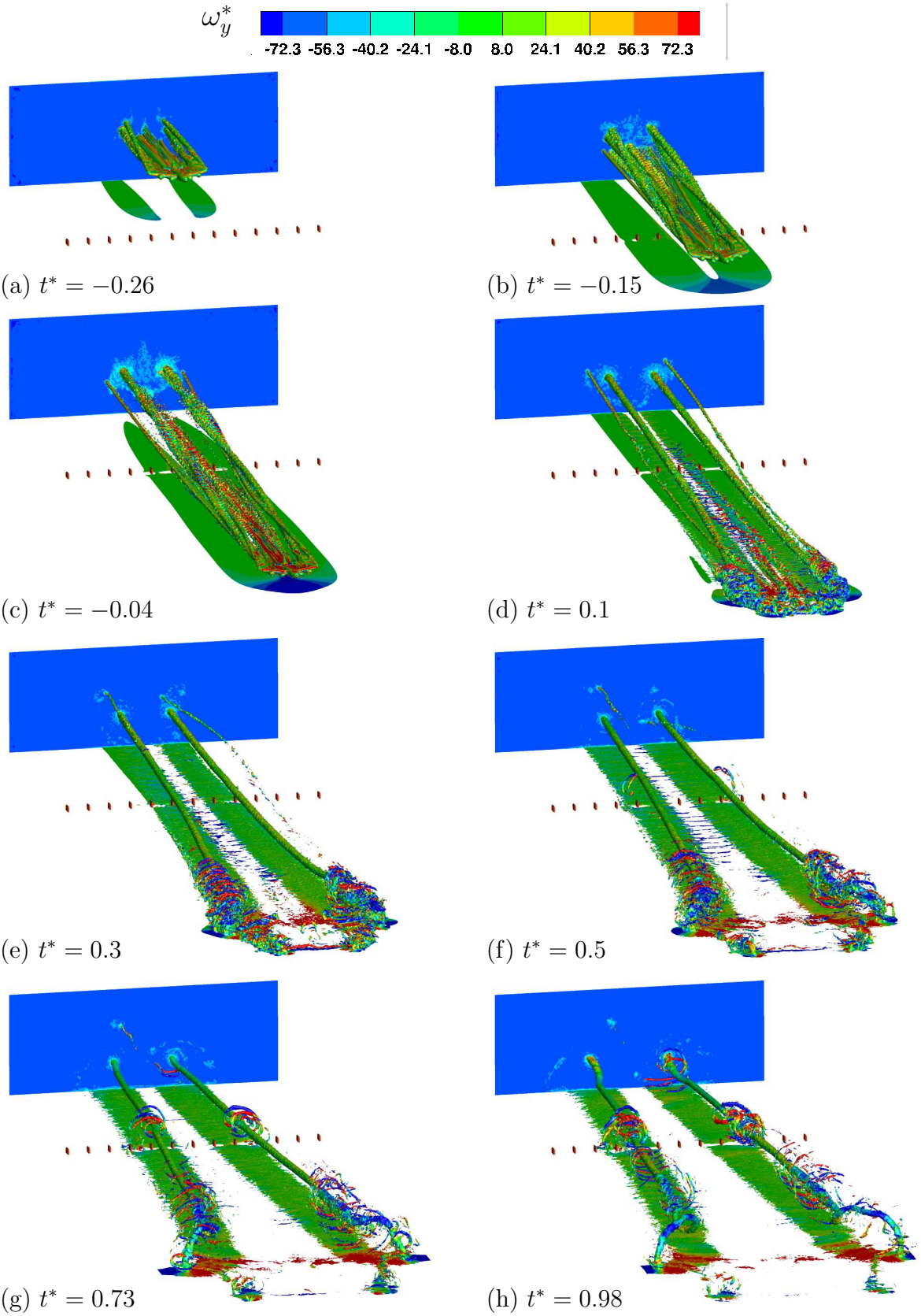

(a) $t^* = -0.26$ (b) $t^* = -0.15$

(c) $t^* = -0.04$ (d) $t^* = 0.1$

(e) $t^* = 0.3$ (f) $t^* = 0.5$

(g) $t^* = 0.73$ (h) $t^* = 0.98$

Abbildung 3.1.: Aircraft landing with roll-up, approach, touchdown, plate line, and developing end effects, case 10. Iso-vorticity surface $||\omega^*|| = 110$ colored with vorticity in spanwise direction (Stephan et al., 2013b).

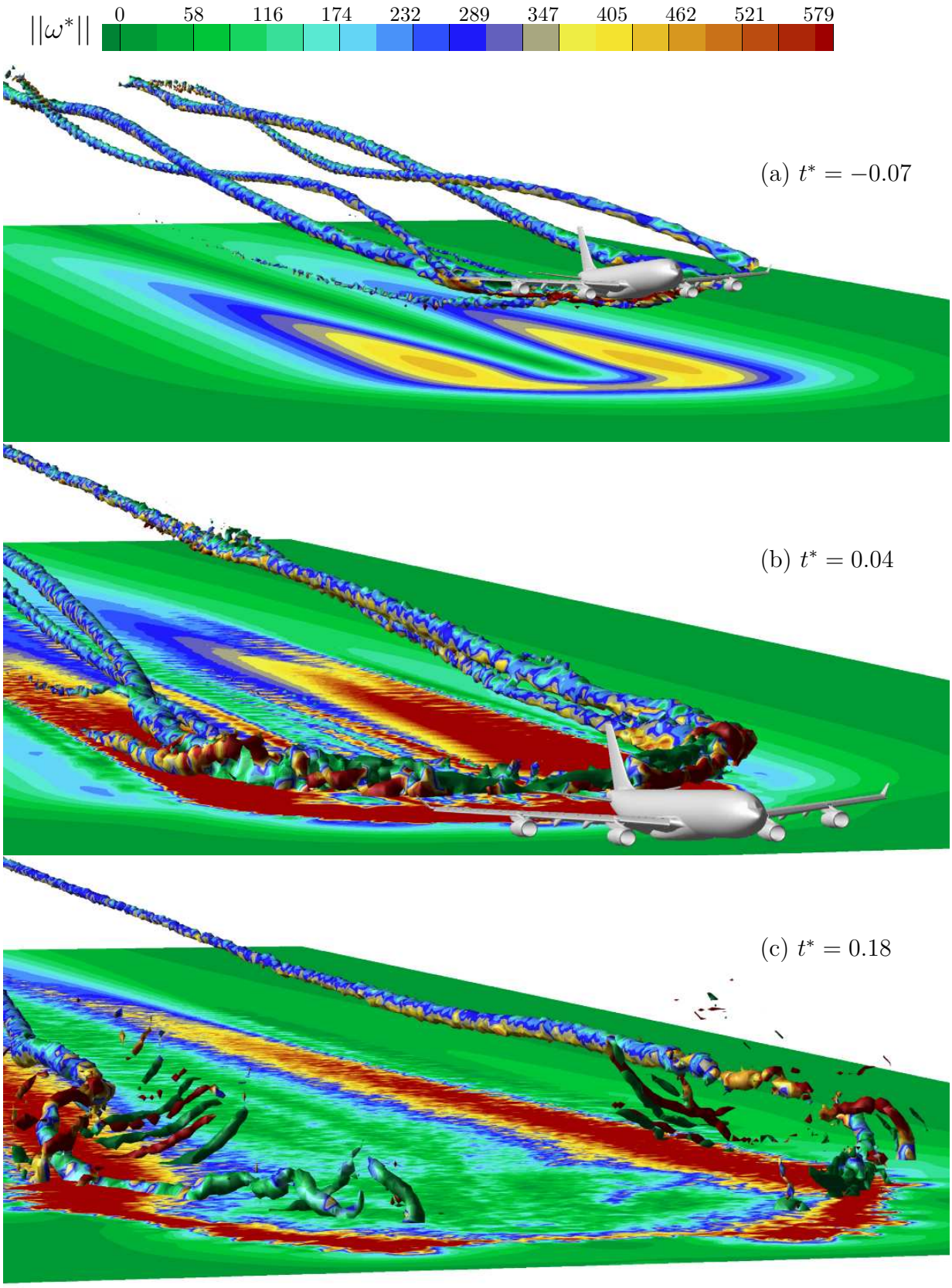

Abbildung 3.2.: Aircraft landing with roll-up, approach, touchdown, and developing end effects, case 9. Iso-vorticity surface $||\omega^*|| = 346$ colored with vorticity in spanwise direction.

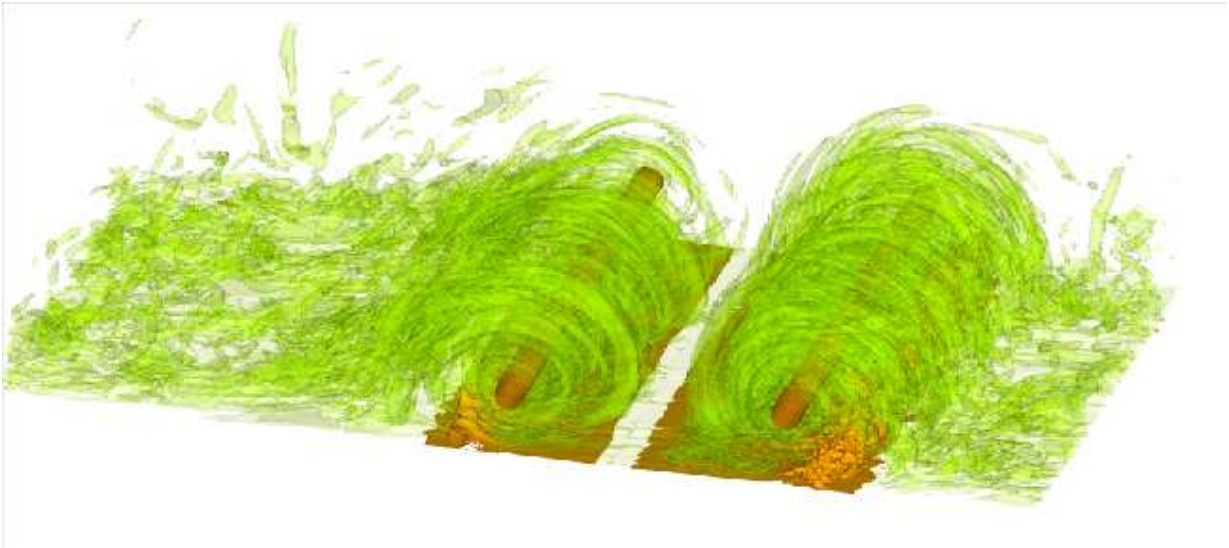

Abbildung 3.3.: Wake vortex pair in crosswind situation, case 1. Two levels of iso-surfaces $||w^*|| = 31.4$ (brown) and 3.14 (green), (Stephan et al., 2013a).

3.2.2. Vortex pair in ground proximity

In the early phase the approach of a vortex pair to a planar wall can be regarded as quasi two dimensional. Early achievements in the framework of inviscid theory, employing a free slip ground surface, imply a monotonic descent of the vortices on hyperbolic trajectories (Lamb, 1932; Saffman, 1979). However a viscous boundary layer changes the flow characteristics strongly (Schlichting & Gersten, 1997).

When the vortex pair descends it induces a vorticity layer at the ground (Harvey & Perry, 1971), see Fig. 3.3. An adverse pressure gradient builds up in the boundary layer while the primary vortices are diverging. The boundary layer bifurcates with a layer remaining close to the wall and a layer growing from the surface, which finally rolls up into secondary vortices and separates (Doligalski et al., 1994). From numerical simulations, as well as field measurement campaigns (Holzäpfel & Steen, 2007) we observe a minimum descent height of about $b_0/2$, (assuming the vortices are initialized sufficiently aloft), at the instant when secondary vortices detach from the ground.

3.2.3. Crosswind effect

Crosswind also induces vorticity at the ground, which has opposite sign as the vorticity layer induced by the up-wind vortex and the same sign as the vorticity layer induced by the downwind vortex, see Fig. 3.4. So the crosswind vorticity supports the formation of the downwind vorticity layer and attenuates the upwind vorticity layer. As a consequence vorticity layers generated by the wake vortices become unequally strong and the upwind and downwind vortices behave asymmetrically. The magnitudes of the wake-vortex induced vorticity layers are growing leading eventually to separation and the generation of counter-

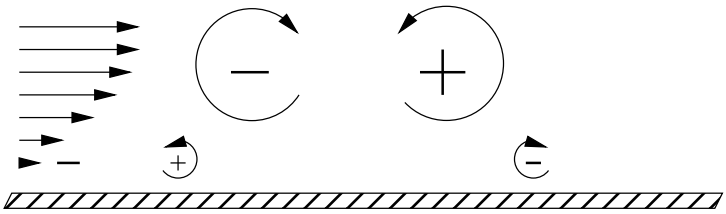

Abbildung 3.4.: Sketch of wake vortex flow with crosswind.

rotating secondary vortices, first at the downwind and then at the upwind vortex. Then the secondary vortices rebound and interact with the primary vortices, which we will discuss in detail. We also observe that the turbulent structures (streaks) of the wind boundary layer are entrained during the roll-up while these structures are cleared out at the ground between the vortices, see Fig. 3.3.

3.2.4. Obstacle effect

In this section we compare wake vortex flow above flat ground with ground obstacles, both with the influence of a crosswind. When we impose an obstacle at the ground surface the flow changes substantially. At the top and edges of the barrier secondary vorticity is generated rapidly after vortex initialization, which subsequently detaches and develops into a distinct loop, as shown in Fig. 3.5 (right). The loop is stretched and winds around the primary vortex forming an omega-shaped loop, approaching and immersing itself into the primary vortex. The process follows the vortex stretching and tilting mechanisms detailed in Holzäpfel et al. (2003b). The geometrically induced SVSs travel along the primary vortices driven by self-induced velocity induction while they weaken the primary vortices efficiently as we show below in detail. In Fig. 3.5 (left) we see that for flat terrain the separation process just begins at a time of $t^* = 1.35$. By this time with an obstacle at the ground substantial disturbances engulf the primary vortices (Fig. 3.5 right).

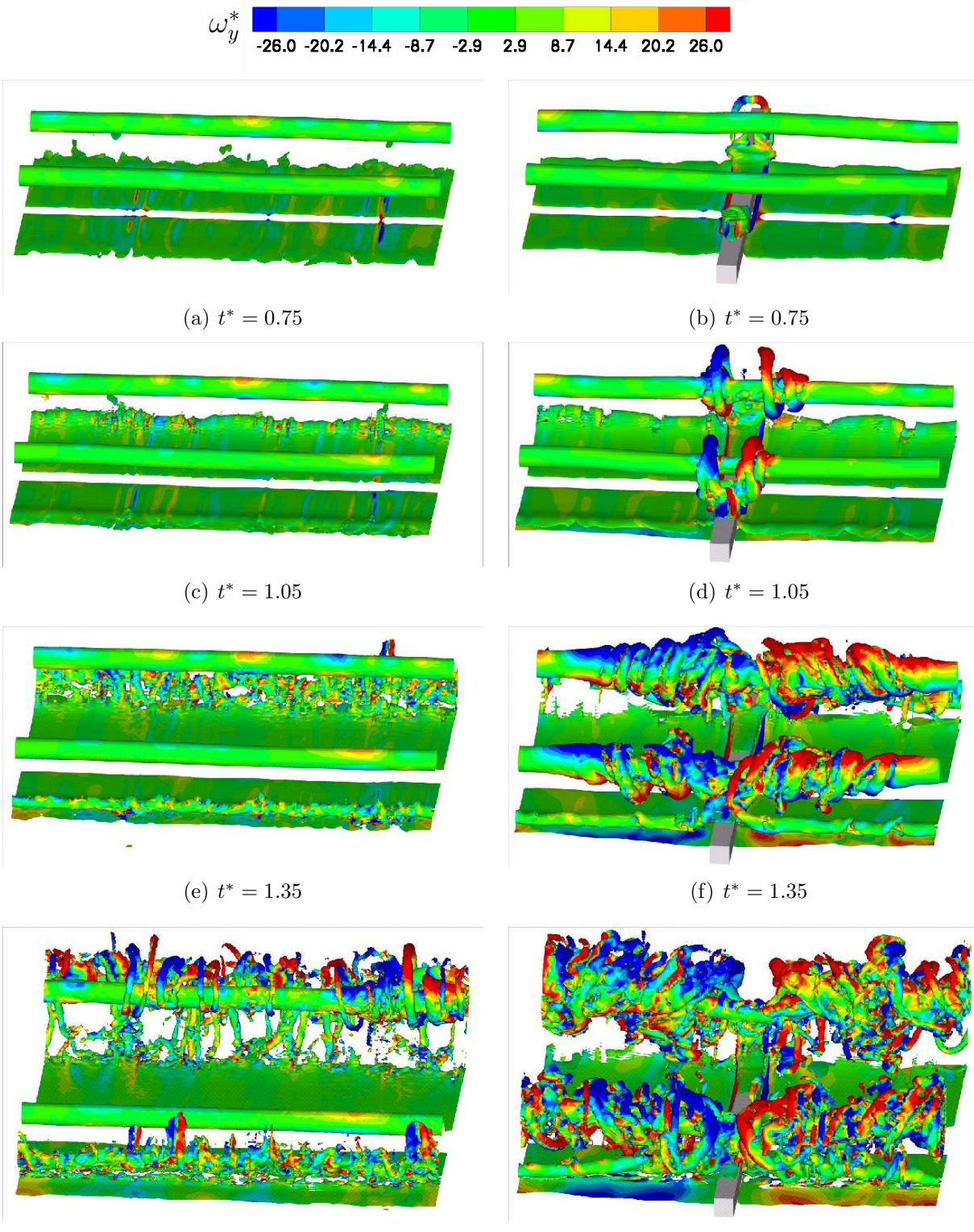

(a) $t^* = 0.75$ (b) $t^* = 0.75$

(c) $t^* = 1.05$ (d) $t^* = 1.05$

(e) $t^* = 1.35$ (f) $t^* = 1.35$

(g) $t^* = 1.75$ (h) $t^* = 1.75$

Abbildung 3.5.: Wake vortex evolution with crosswind without, case 1 (left) and with square-shaped obstacle, case 3 (right) at the ground. Iso-surfaces of $||w^*|| = 39.4$ colored by vorticity strength ω_y^* in spanwise direction (Stephan et al., 2013a).

3.3. Wake-Vortex Evolution With Flat Ground

Wake vortices generated before flare (above $b_0/2$) in the approach phase can be assumed as fully rolled up when they hit the ground surface. This part of the flow is investigated with temporal LES.

3.3.1. In ground effect without turbulence, academic case

In this section the in ground effect without any ambient turbulence is presented. Simulations with ambient turbulence can be considered as an extension of this academic case. This simulation serves as a reference case.

The flow field is depicted in Fig. 3.6. Wake vortices approach the ground and diverge on hyperbolic trajectories. Secondary vortices are generated, separate and rotate around the primary vortices, which consequently rebound. The trajectory is no longer hyperbolic, see Fig. 3.7. Tertiary vortices roll up and rebound. The flow remains laminar for a long time. Finally secondary vortices develop so called short wave instabilities and start to interact with the primary vortices, see Harris & Williamson (2012).

3.3.2. Wake-vortex decay mechanisms in crosswind situation

In this section the effect of a turbulent crosswind on the wake-vortex evolution is investigated further. The wind is established in a separate simulation as detailed in Sec. 2.6.1. The time-averaged stream-wise velocity of the crosswind at the initial vortex height is $0.85w_0 = 1.52\,\mathrm{m/s}$, where w_0 is the initial vortex descent speed. In contrast to the wake vortex decay mechanisms that appear aloft, which are driven by atmospheric turbulence and thermal stratification (Misaka et al., 2012b; Holzäpfel et al., 2003b) an important origin of turbulence here is the no slip condition at the ground, i.e. the strong shear established between the free crosswind flow and the no slip condition directly at the ground surface. The generated counter-rotating secondary vortices eventually develop into relatively strong turbulent structures initiating rapid vortex decay. Figure 3.3 (b) shows that the secondary vortices do not detach homogeneously from the ground but that hairpin vortices or omega-shaped vortices detach at distinct positions and then wrap around the primary vortices. As explained above this occurs first at the downwind and then at the upwind vortex. To our knowledge, this phenomenon has not been well documented and explained before. Thus we examine the origin of these instabilities in our simulations.

A closer look at the velocity distribution at the ground, before imposing the vortex system, reveals a wave-shaped pattern of highly elongated structures, so-called streaks seen in Fig. 3.8 (Jimenez & Moin, 1991; Adrian et al., 2000). These streaks correspond to regions of high velocities oriented in crosswind/spanwise direction (u_y) in immediate ground proximity. Regions of high crosswind velocity (gradients) and low crosswind velocity (gradients) at the ground strengthen or weaken the roll-up process of the secondary vortices, respectively (Fig. 3.4).

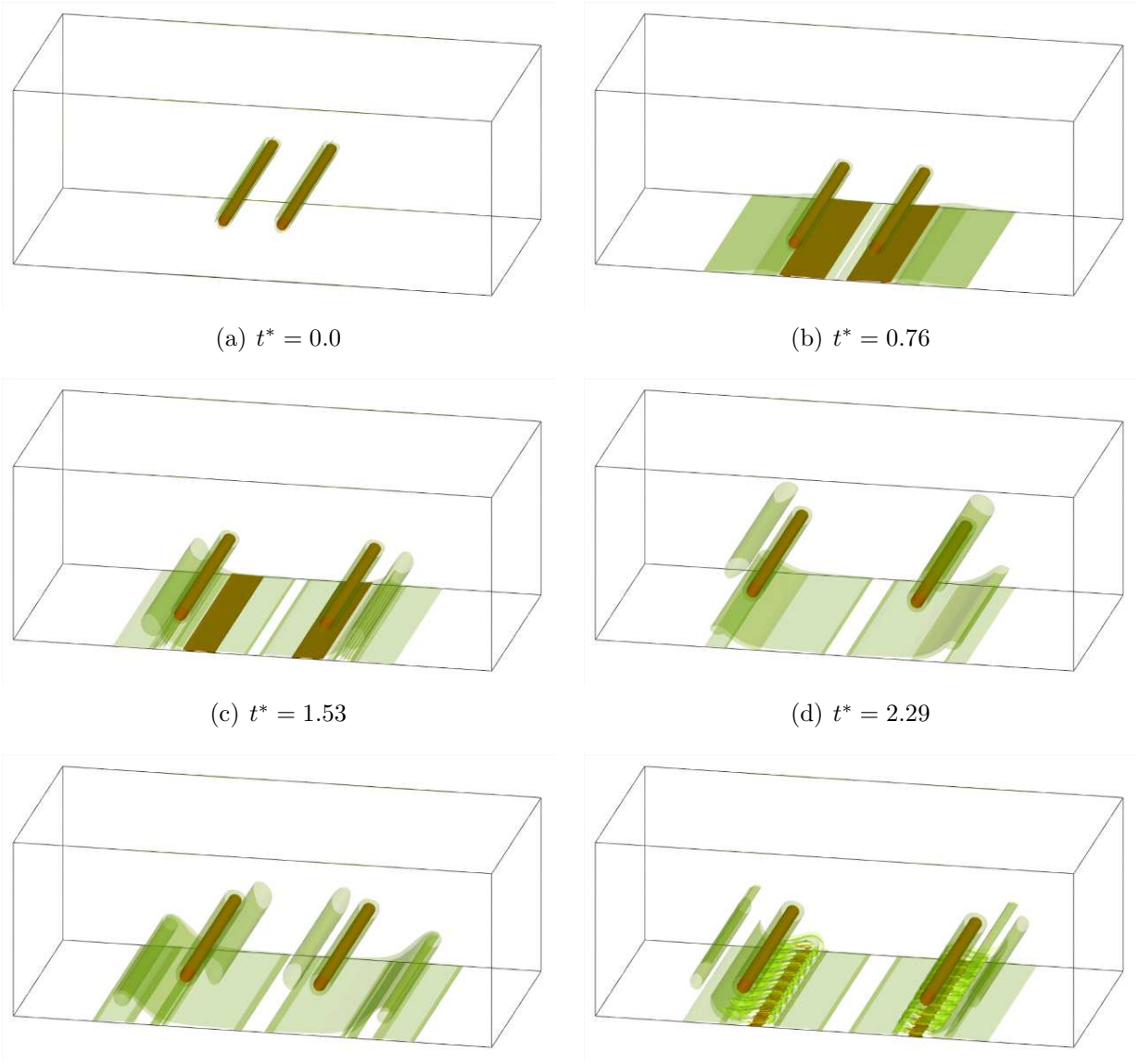

(a) $t^* = 0.0$ (b) $t^* = 0.76$

(c) $t^* = 1.53$ (d) $t^* = 2.29$

(e) $t^* = 3.05$ (f) $t^* = 3.82$

Abbildung 3.6.: Wake vortex evolution without turbulence, case 0. Two levels of iso-surfaces $||w^*|| = 31.4$ (brown) and 3.14 (green).

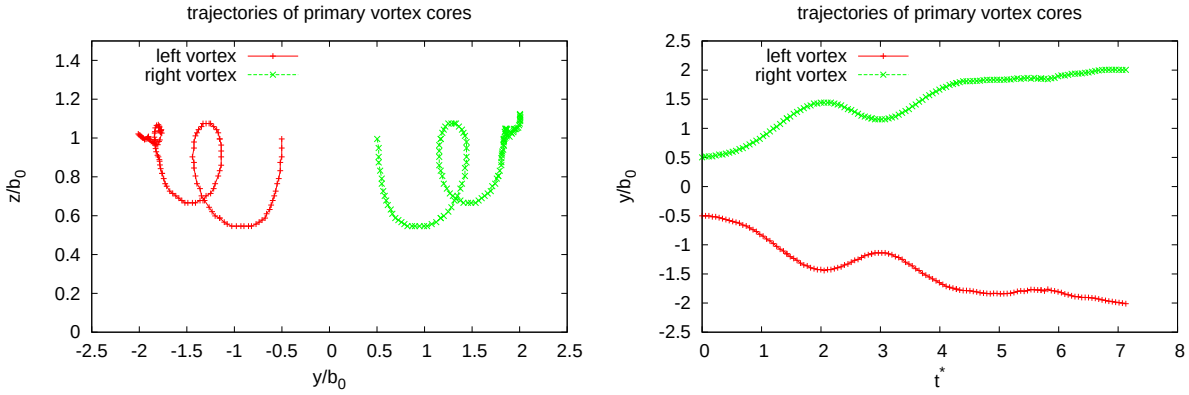

Abbildung 3.7.: Evolution of primary vortex center trajectories, case 0 laminar flow.

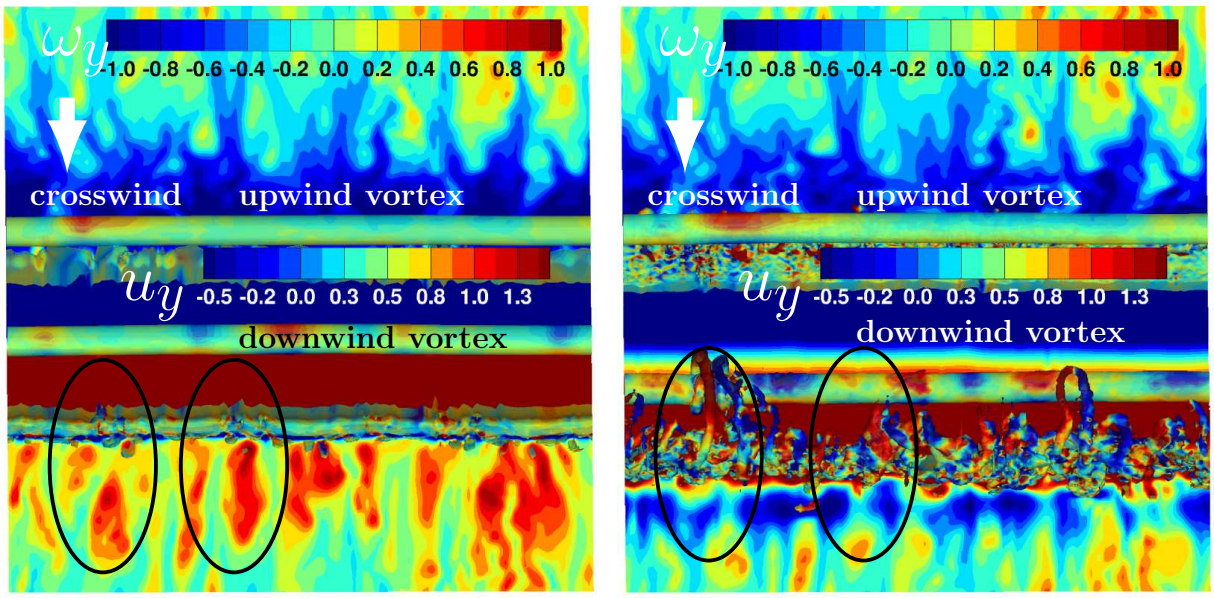

(a) $t^* = 0.95$ (b) $t^* = 1.52$

Abbildung 3.8.: Velocity irregularities at the ground (streaks) trigger hairpin vortices at secondary downwind vortices, case 1, top view. Iso-surface of vorticity magnitude $||w^*|| = 39.4$ colored by ω_y vorticity component, showing primary and secondary vortices (foreground), combined with velocity at the ground surface showing regions of near-wall crosswind excesses (back ground). (Stephan et al., 2013a)

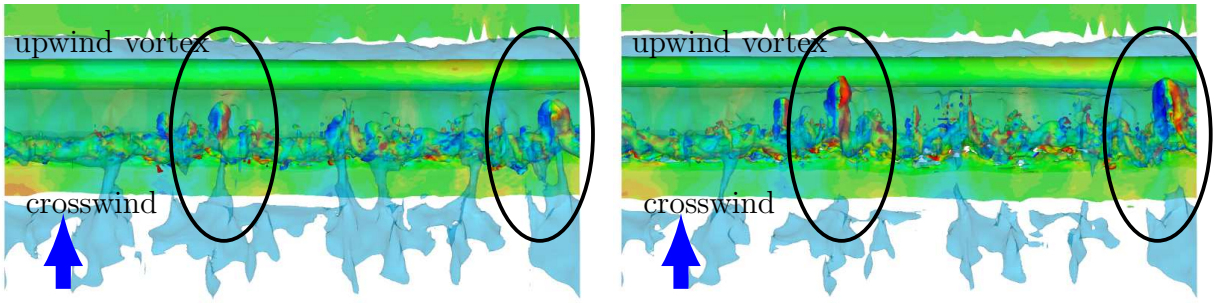

(a) $t^* = 1.61$ (b) $t^* = 1.71$

Abbildung 3.9.: Velocity irregularities at the ground trigger hairpin vortices at secondary upwind vortex, case 1, top view. Iso-surface of vorticity magnitude $||w^*|| = 39.4$ colored by ω_y vorticity component, showing primary and secondary vortices, with iso-surface of velocity $u_y^* = 0.06$ (translucent) showing regions of near-wall crosswind deficits (Stephan et al., 2013a).

So a region of small vertical wind gradients at the upwind secondary vortex (Fig. 3.9) and a region of high wind gradients at the downwind secondary vortex (Fig. 3.8) both influence the secondary vortices to detach earlier. The shape and development of the omega loops are clearly visible in Fig. 3.8 at the downwind vortex, whereas the correlation of the boundary layer streaks and the omega loops is even more obvious for the upwind vortex, as shown in Fig. 3.9.

As a consequence a correlation of the crosswind structures in the boundary layer flow and the secondary vortex disturbances should be expected. In the LES computations the crosswind structures correspond to streaks with a spacing $\lambda^+ \sim 100$ ($\lambda \sim 27\,\mathrm{m}$) which is also found in experiments (Cantwell et al., 1978) as well as in numerical simulations for a relatively large molecular viscosity (Jimenez & Moin, 1991). Butler & Farrell (1993) provide evidence that $\lambda^+ \sim 100$ also holds for a small molecular viscosity. Consequently, the dimensions of the disturbances of the secondary vortices are highly dependent on the molecular viscosity. Hence, for a molecular viscosity of air the streak spacing would be on the order of centimeters, which is insignificant for wake vortices. We suppose that in reality inhomogeneities of the ground on the order of several meters may cause similar crosswind gradients at the ground surface leading to similar decay scenarios as observed at $\mathrm{Re}_\tau = 23\,130$. Unfortunately, limitations of computational resources limit wall resolving LES to relatively low Reynolds numbers, whereas wall models do not yield the required coherent structures. The following list provides a description of wake vortex decay in ground proximity broken down to five steps, where the different items will be discussed in detail below:

- The formation of secondary vortices is favored at crosswind velocity excesses or deficits for the downwind and upwind vortex, respectively, and can be triggered by perturbations like crosswind streaks

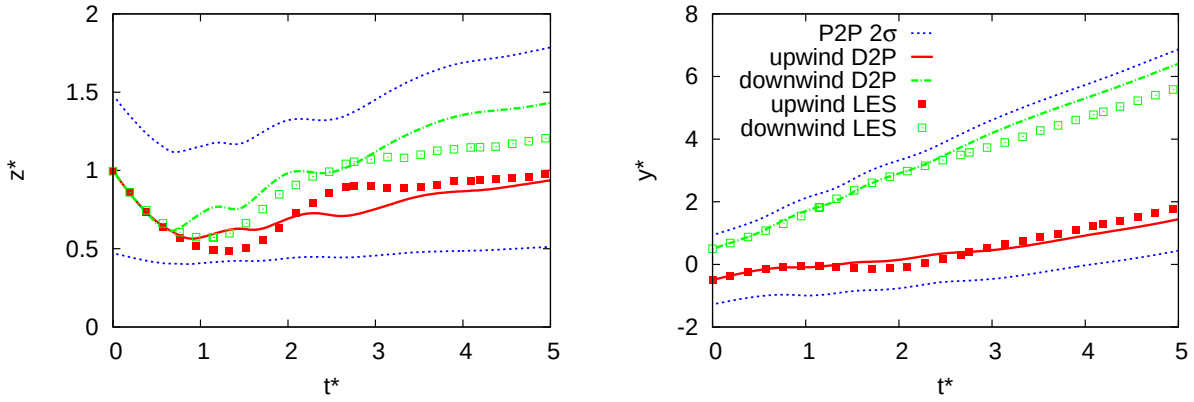

Abbildung 3.10.: Evolution of normalized vertical and lateral vortex positions of wake vortices in crosswind situation. Results from LES, case 1, compared with deterministic predictions from D2P and 2σ envelopes from P2P wake vortex model (Stephan et al., 2013a).

- The subsequent stretching and tilting of the secondary vortices by the primary vortex causes intense omega loops (hairpin vortices)
- Omega shaped secondary vortices approach the primary vortex by self-induction
- After the secondary vortex has looped around the primary vortex, the omega head widens driven by self induction
- The interaction of approaching secondary vortices and primary vortex causes turbulence and annihilation of vorticity

The prominent role of secondary vorticity structures for wake vortex decay is well known and has also been analyzed in detail in Holzäpfel et al. (2003b). The formation of omega loops from secondary vortices has been studied in Ortega et al. (2003). We will have a closer look at these mechanisms when we investigate the effect of obstacles at the ground. An idealized development of a strong omega loop can be seen in Fig. 3.13.

3.3.3. Trajectories and decay

In the LES simulations primary and secondary vortex centers can be tracked. This is done by detecting local pressure minima and extreme values of vorticity. Results for the axially averaged vortex core trajectories are displayed in Fig. 3.10 and compared with predictions of the deterministic and the probabilistic two-phase wake vortex decay and transport model (D2P, P2P) Holzäpfel (2003); Holzäpfel & Steen (2007). In the LES results, it is seen that the wake vortices descend somewhat deeper and the final vertical and lateral offsets are smaller than in the deterministic real-time predictions. Clearly, Fig. 3.10 shows that the

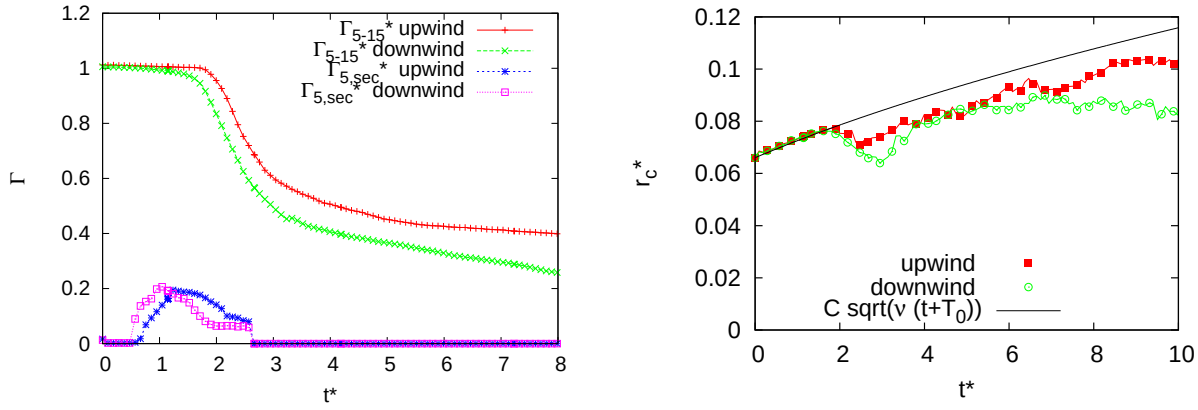

Abbildung 3.11.: Evolution of vortex circulation, case 1, for primary and secondary vortices (left) and core radius with characteristic core growth for LES code (right) (Stephan et al., 2013a).

LES curves reside well within the probabilistic model predictions at 2σ (95.4%) envelopes.

Of particular interest is the vortex strength that ultimately might affect a following aircraft. As a common measure of the vortex intensity for aircraft with sufficiently large wingspans, we consider Γ_{5-15} for the primary and Γ_5 for the secondary vortices. The evolution of these quantities is shown in Fig. 3.11. For early times, where the upwind vortex may be located at the most critical point hovering over the runway, the circulation remains almost constant. Then the phase of rapid decay sets in for the upwind vortex at $t^* = 1.5$ and for the downwind vortex at 1.9 shortly after the secondary vortices have reached a maximum strength. Finally the circulation decay rate is reduced which is again more pronounced for the downwind vortex. Remarkably, in spite of the rapid decay between $t^* = 1.5$ and 3 the core radius of the primary vortices, defined as the averaged distance from vortex center to the point of maximal tangential velocity, is shrinking temporarily, as shown in Fig. 3.11 (right), before it starts to grow steadily. The high viscosity and numerical dispersion cause unrealistically high growth rates of the core radius (Holzäpfel, 2004). Until a time of $2t_0$ we see the characteristic core growth rate ($\sim C\sqrt{t}$) for the used LES code. Between $2t_0$ and $3t_0$ we observe a temporal shrinking of the core radius due to the interaction with the secondary vortices. After $3t_0$ the growth roughly continues at the characteristic rate.

A systematic investigation of the influence of crosswind, headwind and diagonal wind of different strengths on vortex transport and decay with temporal LES was performed in Tchipev (2013) under the supervision of the author. As main results in headwind situation, asymptotic trajectory curves for increasing wind strength have been deduced. The behavior of strongly separated vortices in crosswind situation could be explained by single vortex ground interaction mechanisms. It was shown that for relatively wind speeds the effect of a diagonal wind could be effectively modeled by a superposition of headwind an d crosswind.

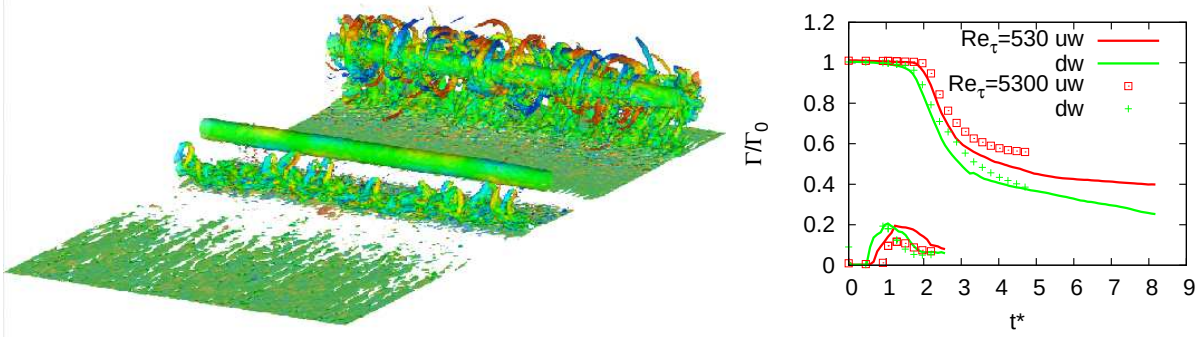

Abbildung 3.12.: (left) Iso-surface of vorticity magnitude $||w^*|| = 39.4$, colored by vorticity in spanwise direction, at $t^* = 1.66$, case 2, (right) evolution of vortex circulation for primary and secondary vortices for different values of Re, case 1 and 2, (Stephan et al., 2013a).

3.3.4. The effect of a wall model in high Reynolds number flows

In this section we discuss Reynolds number effects and the use of a wall model. A simulation with $\mathrm{Re}_\Gamma = 231\,300$ and $\nu = 2.29 \cdot 10^{-3}\,\mathrm{m}^2\,/\,\mathrm{s}$ is used to investigate the Reynolds number dependence of vortex decay. For this purpose we impose the Grötzbach-Schumann wall model based on the logarithmic wall law, to achieve the characteristic boundary layer velocity profile in the pre-simulation. Again we use a pressure driven flow with the same pressure gradient $dp/dy = 5.9 \cdot 10^{-5}\,\mathrm{N}\,/\,\mathrm{m}^3$ as before. As expected the spacing between the detaching SVS becomes much smaller, Fig. 3.12 (left) and the SVS are not well resolved. The vortex decay at a Re which is 10 times larger appears to follow the same physics but is somewhat delayed and the circulation after decay remains slightly higher than in the low Reynolds number case (Fig. 3.12 right). The attenuated decay supports the idea stated in the previous sections that coherent structures generated at the ground, i.e. excesses and deficits in the boundary layer velocity, promote wake vortex decay. On the other hand, also the secondary vortices are stronger for the lower Reynolds number which might explain more intense interaction of primary and secondary vortices leading to slightly increased decay rates.

From the last sections we see that the vortex decay of wake vortices in ground proximity strongly depends on the instabilities of the secondary vortices. Thus the decay depends on the structures of the turbulent crosswind at the ground. In Chapman (1979) the requirements for resolving crosswind streaks in a situation of flat ground are discussed. Obviously for realistic Reynolds numbers the current computing power does not enable us to resolve the viscous sublayer. Without massive grid refinement the interesting structures would all dissolve inside the first grid cell. To the author's knowledge it is an open question, how to model the effect of the unresolved streaks on the vortex flow. In reality the ground surface close to the runway never is ideally flat. Always existing surface irregularities will instead affect the boundary layer flow such that the crosswind excesses and deficits that trigger instabilities of the secondary vortices will emerge at different scales depending on

the local surface and meteorological conditions. Therefore for future work we propose to model reasonable instabilities explicitly.

However, spatial LES indicate that the turbulent aircraft wake causes a structured near surface flow that even develops above an ideally flat surface. In this situation the discussed chain of events that explains wake-vortex decay in ground proximity can also be considered as a direct result of the turbulent aircraft wake.

3.4. Obstacle Effects

3.4.1. Detailed analysis of vortex dynamics with obstacle

For clarity we analyze vortex dynamics triggered by the obstacle without the influence of the turbulent crosswind. In Stephan et al. (2013c) we compare the results from LES with towing tank experiments. There the initial vortex height is approximately $b_0/2$. Therefore in this section the wake vortex pair is initialized at $b_0/2$ (case 4).

The following five characteristics of the phenomenon explain how the dedicated secondary vortices are generated at the ground, how they approach the primary vortices and how their interaction with the primary vortices can be substantially accelerated in order to achieve early vortex decay. Another study investigating the interaction of anti-parallel vortices of different strength was performed by Marshall et al. (2001).

Early detachment of strong omega-shaped secondary vortices

Depending on the obstacle height secondary vorticity detaches earlier. Because the distance to the primary vortices is smaller than $b_0/2$ also the strength of these SVS is slightly increased (Fig. 3.5). In our simulations we find above the obstacle a secondary vortex strength of up to 28% of the primary vortices opposed to 26% above flat ground.

Omega shaped secondary vortex approaches the primary vortex by self-induction

Once the secondary vortices are perturbed due to the obstacle (or other instabilities) the flow can no longer be considered as two dimensional. The early detachment of the vorticity layer above the obstacle leads to an omega-shaped SVS, as shown in Fig. 3.13. Figure 3.13 (left) reveals the physical mechanism of how the hairpin vortex induces itself a velocity towards the primary vortex. This speeds up substantially the interaction between the vortices. Simultaneously the omega-shaped SVS is stretched and bent around the primary vortex by its velocity field as detailed in Holzäpfel et al. (2003b). Subsequently the spirally moving secondary vortex induces itself a propagation velocity along the primary vortex similar to free vortex rings (Fig. 3.13 right).

After the secondary vortex has looped around the primary vortex it travels along the primary vortex again driven by self induction

The helically looped SVS propagates up and down along the primary vortex where the two vortices are merging to a single highly turbulent vortex (Fig. 3.5). The secondary vortex also deforms the primary vortex. During that process the secondary and primary vortices take the shape of a screw and a double helix is created, larger and wider at the basis above the obstacle (Fig. 3.14a).

In this phase we identify two complementary effects, leading to an axial velocity inside the vortex, as shown in Fig. 3.14b. Similar effects are also known as end effects that were observed in test facilities with finite length Bao & Vollmers (2005).

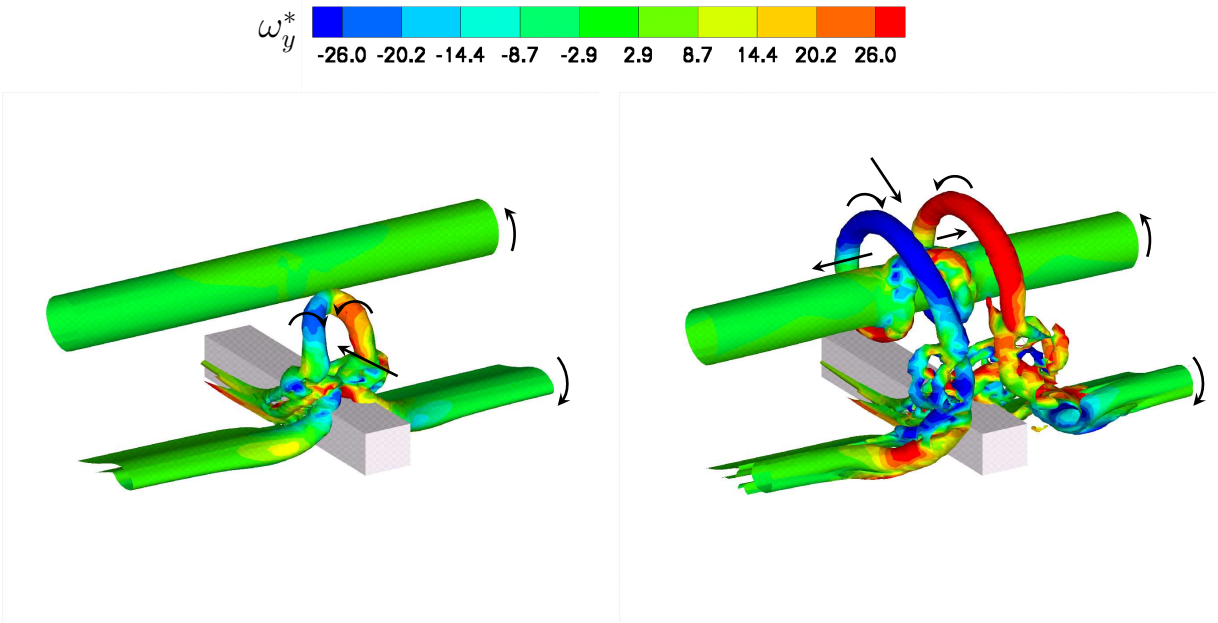

Abbildung 3.13.: LES shows, case 4, that an omega-shaped SVS detaches from the obstacle and induces a velocity towards the primary vortex (left), rolled-up SVS induces streamwise propagation velocity (right). Iso-surfaces of $||w^*|| = 39.4$ colored by vorticity strength ω_y^* in spanwise direction (Stephan et al., 2013a).

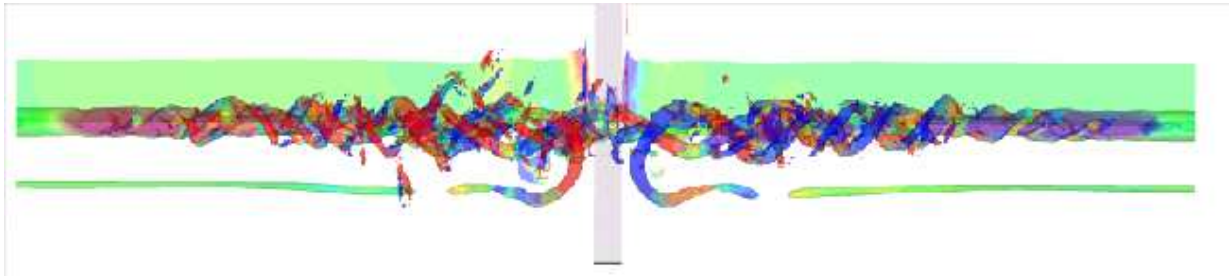

(a)

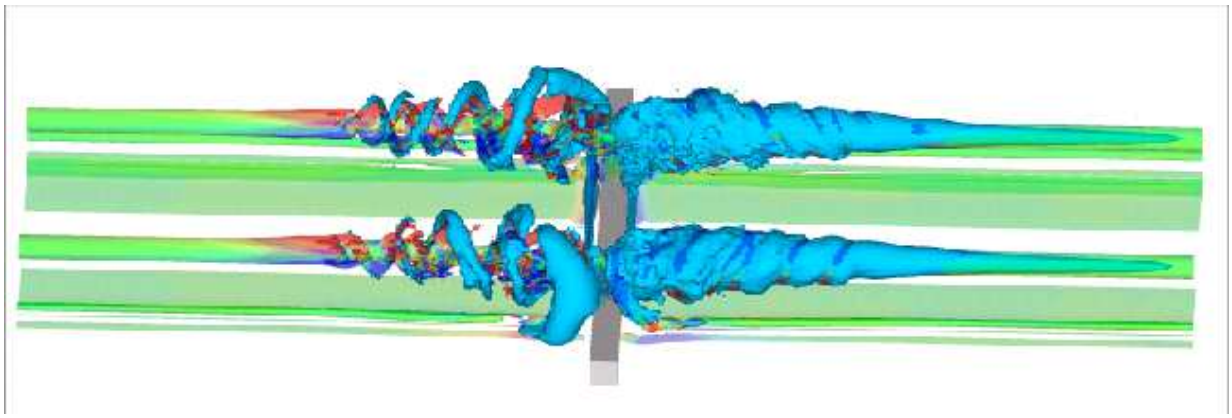

(b)

Abbildung 3.14.: Iso-surface of vorticity magnitude $||w^*|| = 105.2$ colored with vorticity strength ω_y in spanwise direction, case 4, (a) forming a double helix at $t^* = 0.84$ (color indicates sense of rotation), (b) with an additional blue iso-surface of axial velocity $u_x^* = 0.56$ at $t^* = 0.61$ (Stephan et al., 2013a).

(*i*) When primary and secondary vortex are transformed into a double helix, both vortices have the same sense of rotation and helicity and consequently induce an axial velocity to the same direction inside the double helix, blue cone in Fig. 3.14b.
(*ii*) We also observe an axial velocity in the vortex core in regions far ahead of the helix (Fig. 3.14b). The second effect is initiated by a reduction of the circulation above the obstacle (Fig. 3.15) corresponding to a local increase the pressure in the vortex core. This leads to a pressure gradient within the vortex core in axial directions inducing axial velocities, as seen in Fig. 3.15, where the locally averaged pressure and velocity in flight direction at the vortex center are depicted. The pressure disturbance starts at a time of $t^* = 0.08$ and reaches the domain boundary at a time of $t^* = 0.53$, corresponding to a propagation speed of $U_{hel}^* = 8.8$. The propagation of pressure disturbances in Lamb-Oseen vortices has been thoroughly investigated in Moet et al. (2005).

The described obstacle effects have similar characteristics as end effects generated by aircraft that touch down on the tarmac. Obstacle effects, end effects occurring in a towing tank facility and after touchdown are all characterized by an instability inside the the

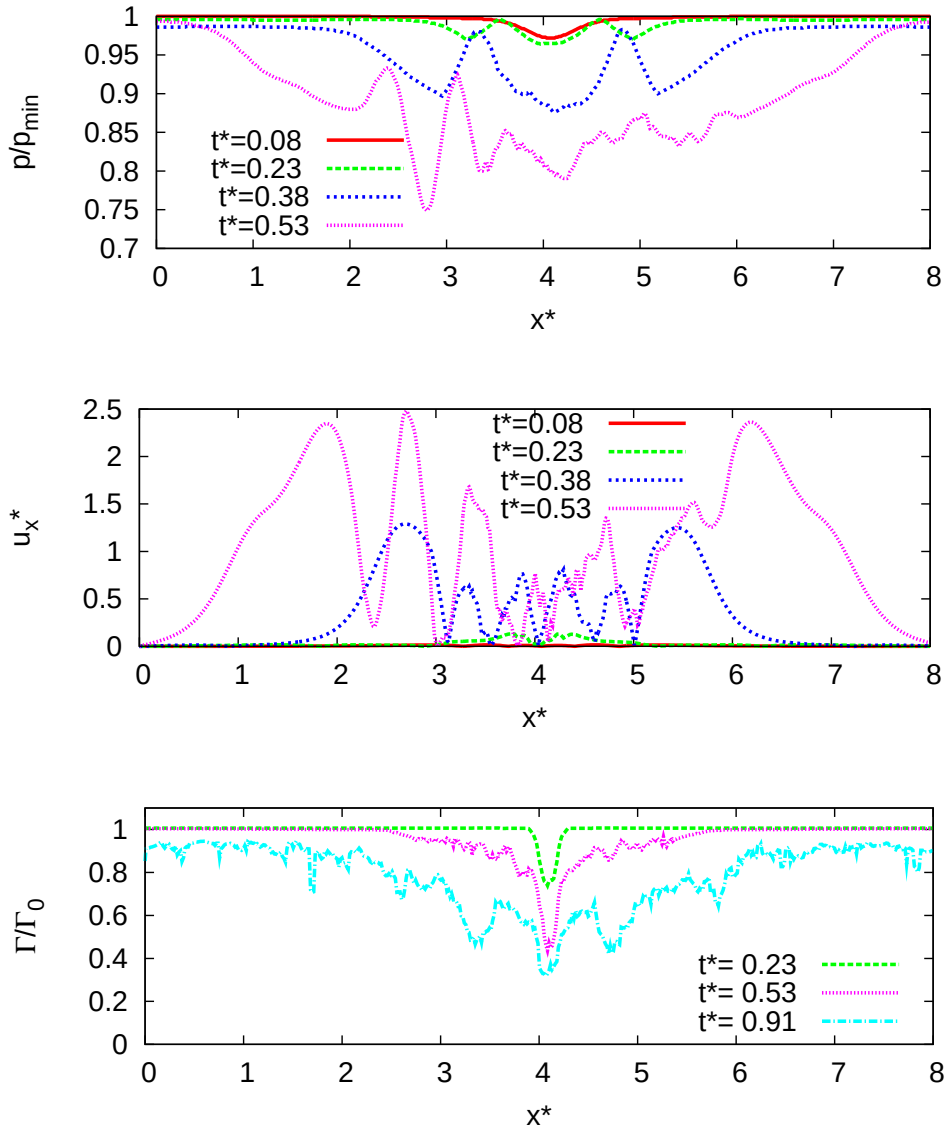

Abbildung 3.15.: Distribution of $p/p_{\min}, u_x^*$, and Γ_{5-15}^* along the vortex center, case 4, at different times (Stephan et al., 2013a).

Tabelle 3.2.: Parameters of secondary vortex helix evaluated from LES.

t^*	x^*	U^*_{hel}	Γ^*_{hel}	R^*_{hel}	a^*_{hel}	U^*_{ring}	U^*_{hel}/U^*_{ring}
0.30	0.32	2.8	0.12	0.082	0.02	2.2	1.27
0.38	0.62	3.9	0.16	0.104	0.02	2.6	1.5
0.46	0.90	3.7	0.23	0.123	0.02	3.3	1.12
0.53	1.34	5.9	0.24	0.081	0.02	4.7	1.26
0.61	1.79	5.9	0.21	0.087	0.02	4.0	1.48
0.68	2.28	6.4	0.18	0.079	0.02	3.5	1.83
0.76	2.81	7.0	0.20	0.064	0.02	4.6	1.52
0.84	3.21	5.3	0.19	0.080	0.02	3.6	1.47

vortex propagating axially along the vortex filaments. They also appear when parallel vortices link Misaka et al. (2012b). This phenomenon of an axial vortex instability will be called end effect in the sequel of the thesis, see Stephan et al. (2013a). The knowledge of the propagation speed of the disturbance and the related rapid decrease of circulation is crucial for practical applications at airports where the decay of wake vortices close to the touchdown zone and suitable distances between adjacent obstacles need to be determined. The spiral disturbance can be approximated as a vortex ring at least during the first stage of its roll-up. Vortex rings move with a self-induced velocity in the direction of the flow inside the ring. The propagation speed depends on the ring radius R, the core radius a and the circulation Γ of the ring vortex. Neglecting viscosity the induced propagation speed of a thin vortex ring can be computed with the following formula (Lamb, 1932):

$$U_{ring} = \frac{\Gamma}{4\pi R}\left(\log\frac{8R}{a} - 0.25\right). \tag{3.1}$$

To determine the propagation speed we consider the helix front, see e.g. Fig. 3.14 (b), and estimate a core radius of $0.02b_0$. We evaluate the circulation Γ^*_{hel} and radius R^*_{hel} of the secondary vortex helix at the helix front for different time steps, see Table 3.2. With these quantities we compute the propagation speed according to Eq. (3.1).

Figure 3.16 indicates that Eq. (3.1) apparently underestimates the propagation speed. In particular in the later stage the double helix propagates at a higher speed compared to a simple vortex ring. Potentially, the conical shape of the double helix as well as the helical shape of the primary vortex cause higher induced velocities. On average the ratio $A = U^*_{hel}/U^*_{ring}$ equals 1.43. We take it as a correction factor for calculating

$$U^*_{hel} = A \cdot U^*_{ring} \tag{3.2}$$

(see Fig. 3.16). For the design of obstacle separations at an airport Eq. (3.1) and Eq. (3.2) may provide an approximation of the propagation speed of the disturbances. Scaling of

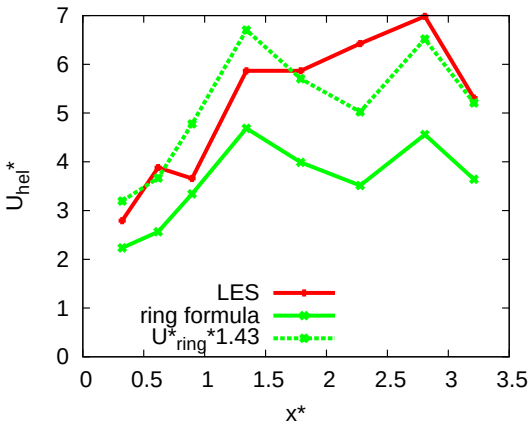

Abbildung 3.16.: Propagation speed of helix compared with theoretical speed of a vortex ring.

Eq. (3.1) allows estimating the propagation velocity for different aircraft types. The interaction of disturbances caused by more than one obstacle is investigated in Stephan et al. (2013c). A study investigating the flow induced by periodic vortex rings wrapped around a straight vortex can be found in Marshall (1997).

Dedicated secondary vortex remains connected to the regular ground effect vortex and thus obtains continued supply of energy

As we can see in Fig. 3.13 the secondary vortex detaches much faster above the obstacle. However it stays connected in accordance to the third Helmholtz law stating that a vortex tube cannot end within a fluid. It must either end at a solid boundary or form a closed loop. Iso-surfaces of vorticity magnitude in Fig. 3.14 show the connected secondary vortex.

Highly intense interaction of primary and secondary vortices leads to rapid wake vortex decay

The decay rates of wake vortices highly depend on the interaction with their environment Holzäpfel et al. (2003b). The circulation decreases while the primary vortex is conducting work on SVS and merging. The stronger the SVS the faster the vortex decay. In ground proximity distinct SVS evolve that trigger vortex decay close to ground. Obstacles lead to an earlier interaction of even higher intensity than the flat ground.

The above identified five flow features describe how obstacles at the ground may induce rapid wake vortex decay independently of natural external disturbances.

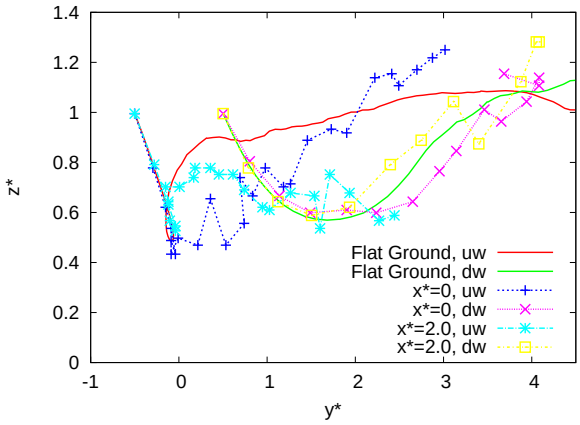

Abbildung 3.17.: Vortex center trajectories for flat ground and different distances from an obstacle with $0.2b_0 \times 0.2b_0$ cross section, case 1 and 3. The series of symbols starts at $t^* = 0$ and proceeds with steps of $0.3t_0$ (Stephan et al., 2013a).

3.4.2. Trajectories and decay

Now we analyze the enhanced decay characteristics quantitatively. As a source of turbulence a crosswind as in Sec. 3.3.2 and Sec. 3.3.3 is initialized. The time-averaged stream-wise velocity of the crosswind at the initial vortex height is $0.85w_0$. We are interested in the change of trajectories, i.e. whether for example the rebound height is influenced by an obstacle or not. We have to keep in mind that we use periodic boundary conditions. So interpreting the simulations correctly, we do not consider the influence of one single obstacle, but periodically arranged obstacles with a separation equal to the domain length of $4b_0$. However, until the disturbance reaches the domain boundary we can neglect the influence of the adjacent obstacles. Because of the intense interaction of primary and secondary vortices it becomes very difficult to track the vortices in the flow with obstacles, especially the downwind vortex, for larger times than $t^* = 3$.

Lateral advection of the primary vortices plays an important role for the clearance of the flight corridor during final approach. In a the weak crosswind situation the upwind vortex may hover above the runway for a long time, as depicted in Fig. 3.17. This is a potentially hazardous situation for following aircraft. We see that an obstacle does not change that fact. Above flat ground the primary vortices can rebound to a height of about $1.1b_0$. Directly above the obstacle the rebound height is much reduced but can exceed the height above flat ground at later times when circulation is already much reduced (Fig. 3.18). In a distance of $x^* = 2.0$ the rebound remains consistently below that with flat ground.

Above the obstacle we observe a tremendous and rapid reduction of the circulation to 50% of the initial circulation (Fig. 3.18a) at a vortex age of $1.5t_0$, whereas in case of a flat ground the circulation does almost not change in this early time period. We further observe that within a distance of $2b_0$ from the obstacle the circulation is also reduced faster. Because the decay does not develop uniformly along the vortex filaments, we compare wake vortex

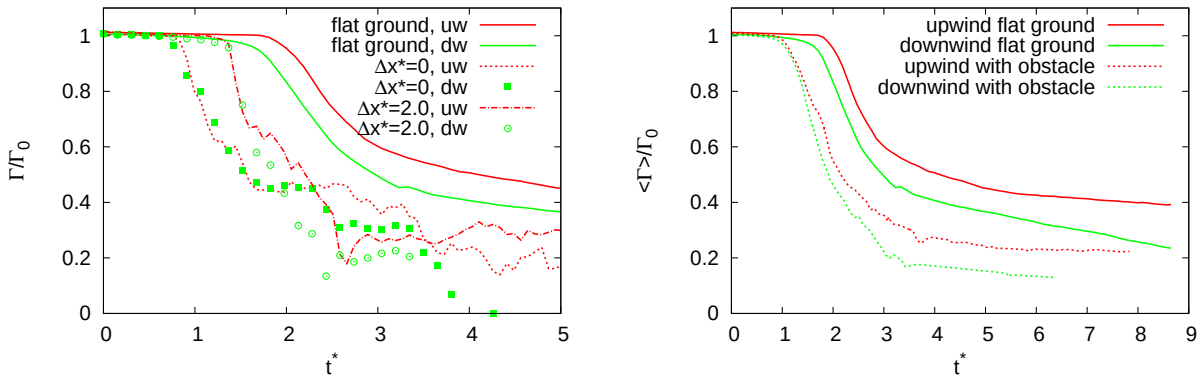

(a) (b)

Abbildung 3.18.: Vortex circulation Γ_{5-15} in crosswind situation with flat ground or obstacle with $0.2b_0 \times 0.2b_0$ cross section, case 1 and 3, at (a) different distances from the obstacle (b) averaged in axial direction (Stephan et al., 2013a).

decay with flat ground by averaging Γ_{5-15} in axial directions. During the initial descent the vortex strength remains nearly constant for one t_0 as shown in Fig. 3.18 (b). The decay of Γ_{5-15} sets in when secondary vorticity merges with the primary vortices. With crosswind vortex decay proceeds asymmetrically. The downwind vortex decays faster and reaches lower values than the upwind vortex. With obstacle the decay process is initiated nearly one t_0 earlier. If we assume that the ICAO separation of 5 nautical miles of a Medium aircraft following a Heavy correspond to 120 seconds or 4.6 t_0 we read 50% of the initial circulation for the operationally relevant upwind vortex. Figure 3.18 (b) indicates that the obstacle reduces Γ_{5-15} of the upwind vortex by 50% already at a vortex age of $2t_0$ compared to the case without obstacle where this decay level is only reached two t_0 later. This simple estimate would mean that with obstacles of the chosen dimensions aircraft separations could by halved, provided that it is guaranteed by a WVAS that the glide slope is free of wake vortices.

3.4.3. Effects of different obstacle geometries and headwind

In this section we discuss the shape and the size of the obstacles. In our baseline setting we use $0.2b_0 \times 0.2b_0$ square profiles in normalized coordinates, which corresponds to a barrier of 9 m ×9 m square cross section in reality for an A340 aircraft. This appears quite high for realistic applications at airports. Moreover a massive barrier requires a lot of material and might conflict with frangibility requirements or undershoot or overshoot from the runway. We reduce the obstacle height to $h^* = 0.1$ keeping the width fixed. Furthermore we reduce the obstacle volume. The idea is to mimic the block shape by thin plates at intervals of $\Delta y^* = 0.45$ (21m) to achieve a similar effect, Fig. 2.15.

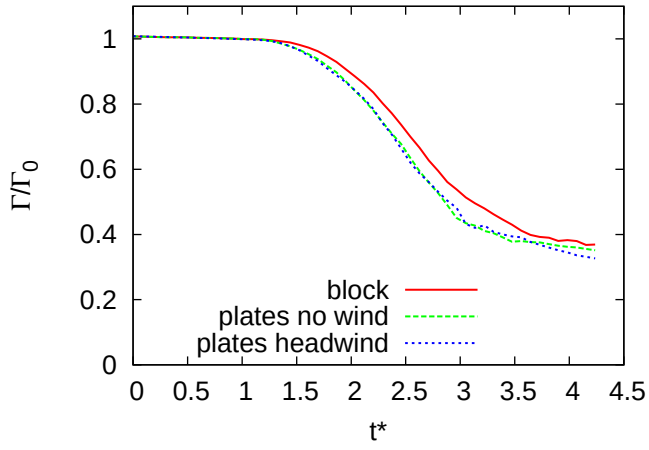

Abbildung 3.19.: Evolution of Γ_{5-15} averaged in flight direction, cases 6, 7, and 8, for different geometries and wind configurations (Stephan et al., 2013a).

Figure 3.19 shows that we can reduce the volume of the obstacle without reducing the effects on wake vortex decay. We see that the decay with the plate line starts even slightly earlier and proceeds slightly faster. Comparing Fig. 3.20 (a) and Fig. 3.21 (a) we observe that a plate line leads to similar effects on the secondary vortices as a block-shaped obstacle. SVS separate even slightly earlier, although their contours are less smooth. The longitudinal circulation distributions look very similar in both cases, Fig. 3.20 (b) and Fig. 3.21 (b). We clearly see that with a plate line the decay is even faster, Fig. 3.19.

A plate line raises the question of robustness with respect to headwind advecting the primary and secondary vortices across the obstacles. The headwind shifts the rolled-up SVS, however each of the listed effects, can still be observed, see Fig. 3.22 (a). Although the headwind shifts the roll-up of the SVS, the effect of the plates appears to be very robust and the averaged circulation decay is not affected, Fig. 3.19. The longitudinal circulation distributions, Fig. 3.22 (b), are shifted in the direction of the headwind.

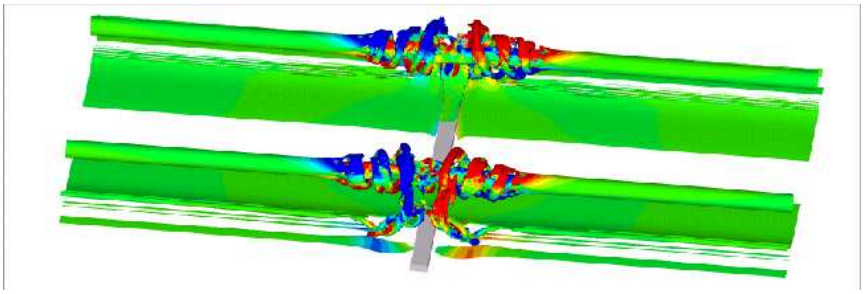

(a)

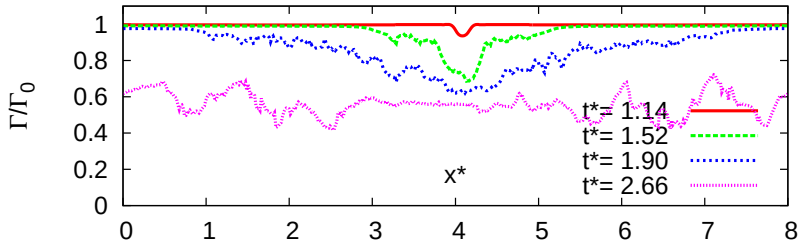

(b)

Abbildung 3.20.: Effect of block-shaped obstacle, case 6. (a) iso-surfaces of $||w^*|| = 52.6$ colored by vorticity in spanwise direction at a time of $t^* = 1.52$, (b) axial distribution of Γ^*_{5-15} at different times (Stephan et al., 2013a).

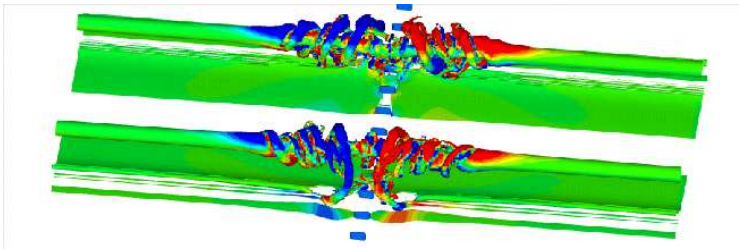

(a)

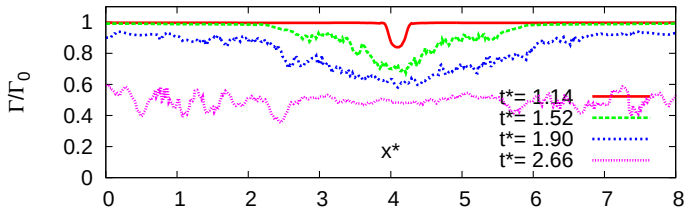

(b)

Abbildung 3.21.: Effect of plate line, case 7. (a) iso-surfaces of $||w^*|| = 52.6$ colored by vorticity in spanwise direction at a time of $t^* = 1.52$, (b) axial distribution of Γ^*_{5-15} at different times (Stephan et al., 2013a).

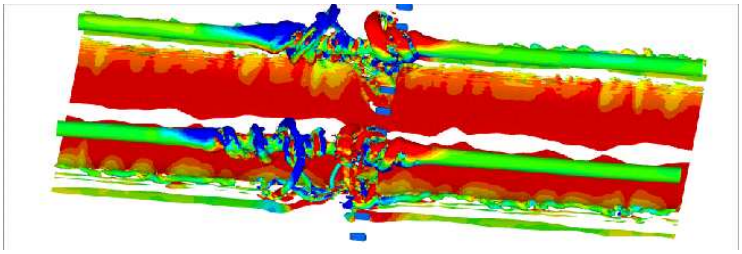

(a)

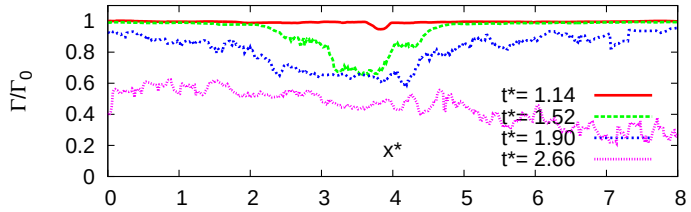

(b)

Abbildung 3.22.: Effect of plate line with headwind, case 8. (a) iso-surfaces of $||w^*|| = 52.6$ colored by vorticity in spanwise direction at a time of $t^* = 1.52$, (b) axial distribution of Γ^*_{5-15} at different times (Stephan et al., 2013a).

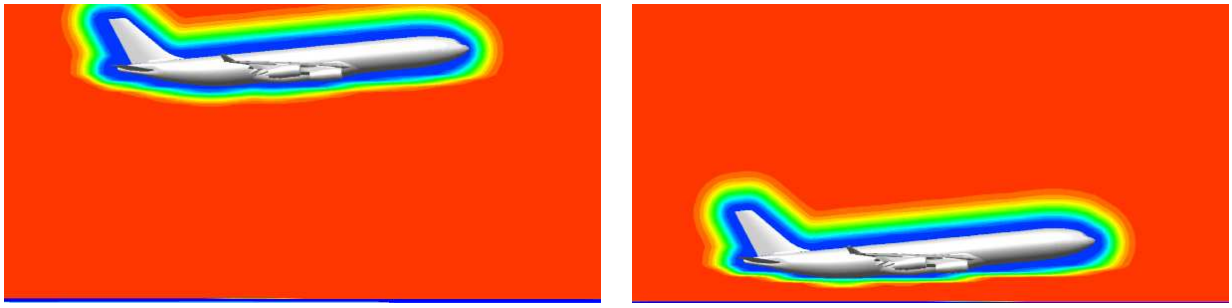

(a) $t^* = -0.14$ (b) $t^* = -0.003$

Abbildung 3.23.: Wall switching function $f(y, \alpha, \beta)$ mapping RANS flow field to the LES domain is adapted towards the ground, case 9, $f \equiv 0$ blue area, $f \equiv 1$ red area.

3.5. Wing-in-Ground Effect

Theoretical considerations of the effects an aircraft experiences in the very ground proximity are reviewed in Sec. 2.1.2. These considerations have been purely stationary, neither flare nor the changing angle of attack have been considered there. A more realistic investigation is described in Sec. 2.1.5. Here particularly the "in ground effect" and its consequence for wake vortex strength is figured out. As we do neither simulate the flare nor modify the angle of attack the realistic case can not serve as a direct reference case for the simulation. Also the theoretical considerations cannot be used directly as a reference because they assume a fix aircraft altitude whereas we consider aircraft descent.

The LES are performed with RANS fields without any influence of the ground. Nevertheless, we use these fields to simulate the in ground effect and touchdown. Therefore the wall switching distance that maps the RANS field to the LES domain, see Eq. (2.55), is adapted beneath the aircraft, see Fig. 3.23. The adaptation is implemented depending linearly on the aircraft altitude. This way the RANS field fades towards the ground surface allowing the flow field to adjust to the aircraft as well as the ground surface. This allows the pressure field to develop between the aircraft and the ground surface, see Fig. 3.24. The left side depicts a pressure iso-surface and reveals the pressure pillow beneath the aircraft and the aircraft nose. During approach to the ground the belly pillow grows. On the right side the contours show the quantitative growth of the pressure in the center plane beneath the aircraft. Hence, we observe the theoretically stated in ground effects with this LES/RANS approach. Fig. 3.25 shows the circulation distribution in axial direction at the instant of touchdown. The ground effect is clearly observable by the increase of circulation towards the ground surface.

In addition theoretical results from Daeninck et al. (2006) are plotted, normalized to the initial circulation of the LES. These assume a double-elliptic wing with an aspect ratio $A_r = b/c = 10.0$ which was used as a typical case for modern commercial airplanes, see Appendix A. Qualitatively the curves agree, but the theoretically stated increase of the

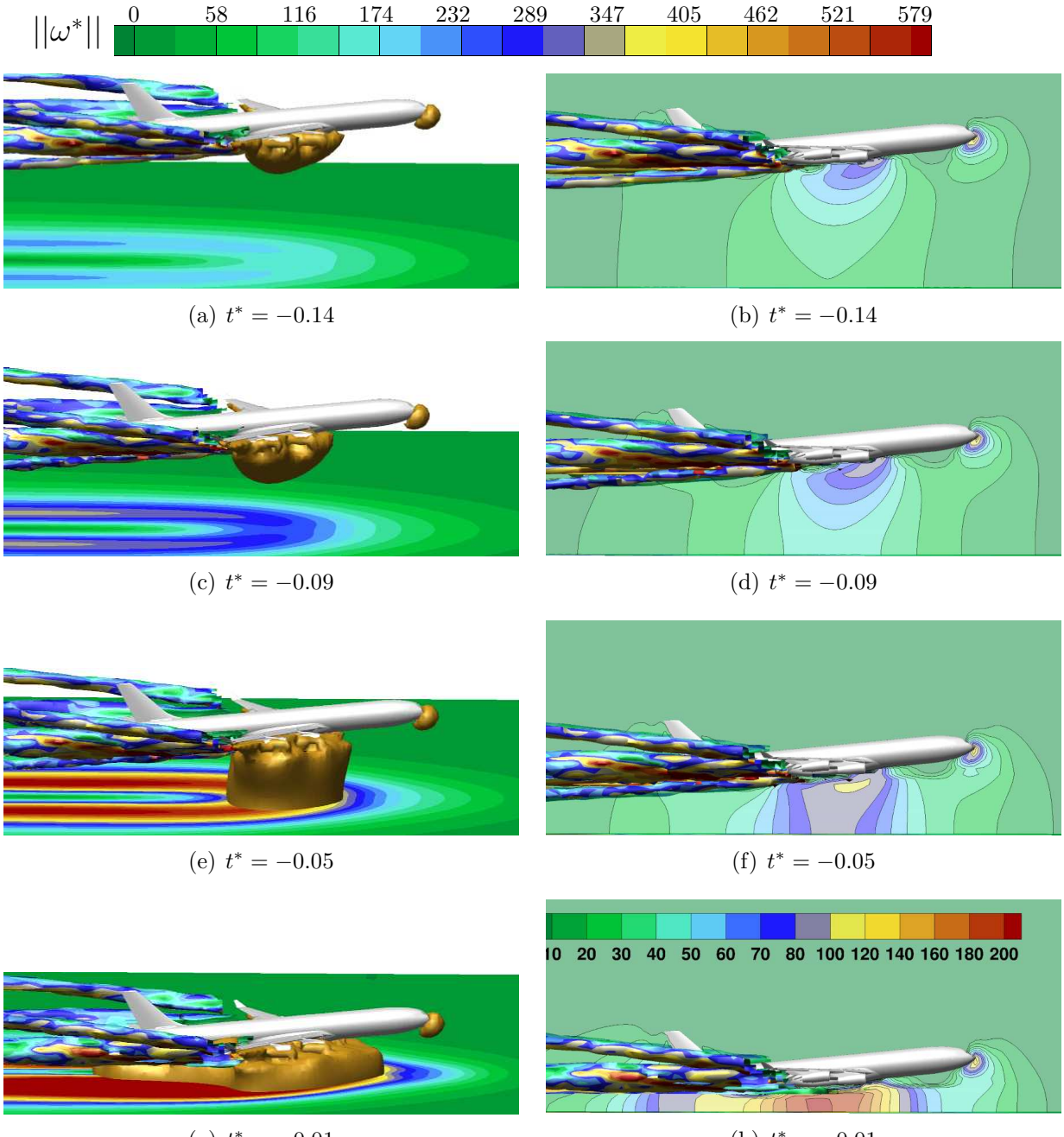

(a) $t^* = -0.14$ (b) $t^* = -0.14$

(c) $t^* = -0.09$ (d) $t^* = -0.09$

(e) $t^* = -0.05$ (f) $t^* = -0.05$

(g) $t^* = -0.01$ (h) $t^* = -0.01$

Abbildung 3.24.: Pressure increase in ground proximity, case 9, pressure iso-surface $p = 60$ N/m^2 (left), pressure distribution in center plane (right). Vorticity magnitude visualizing the ground surface (left) and the wake (both sides).

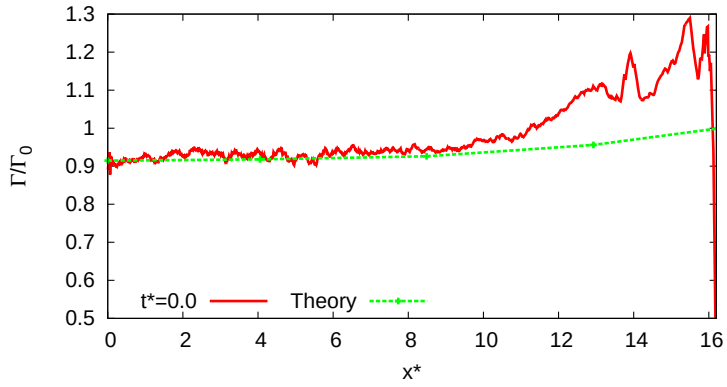

Abbildung 3.25.: Circulation distribution at the instant of touchdown, case 9, comparison with theoretical results from Daeninck et al. (2006).

wake vortex strength is exceeded by the LES simulations, which possibly can be explained by an additional pressure increase due to aircraft descent. Further the theoretical considerations neglect viscosity. Indeed due to viscosity the bound vortex creates a vorticity layer at the ground, see Fig. 3.24 (left), which results in an additional pressure increase beneath the aircraft. For a more accurate investigation RANS fields including the ground surface at different altitudes would be appropriate as well as flight data statistics.

3.6. Touchdown Effects

3.6.1. Vortex divergence

After touchdown wake vortices are abruptly cut off. They are neither connected to the bound vortex nor to the very weak wake of the braking aircraft, see Fig. 3.2, 3.27. Wake vortices diverge in ground proximity. After landing, the divergence is not uniform, but starts at the point of touchdown and proceeds against flight direction, as depicted in Fig. 3.26. At $t^* = 2.22$ a maximum vortex separation of more than $7b_0$ is reached. Later, at the periodic lateral domain boundaries, the vortices connect, see Fig. 3.29 (d), hence we may expect even larger vortex separations close to the touchdown area in reality.

3.6.2. End effects

The disconnected vortices dissolve starting from the point of touchdown as vortices may not end freely in space in accordance with the Helmholtz vortex laws (Kundu & Cohen, 1990). Inside the vortex core the low pressure region is faced with the high pressure region at the end of the vortex. The pressure difference causes strong axial flows and disturbances such that the vortices start to dissolve, see Fig. 3.28 (a) and (c). This phenomenon is called end effect. Together with a reduction of pressure we observe helical disturbances of the vortex core propagating against flight direction. The reduction of circulation coincides with the

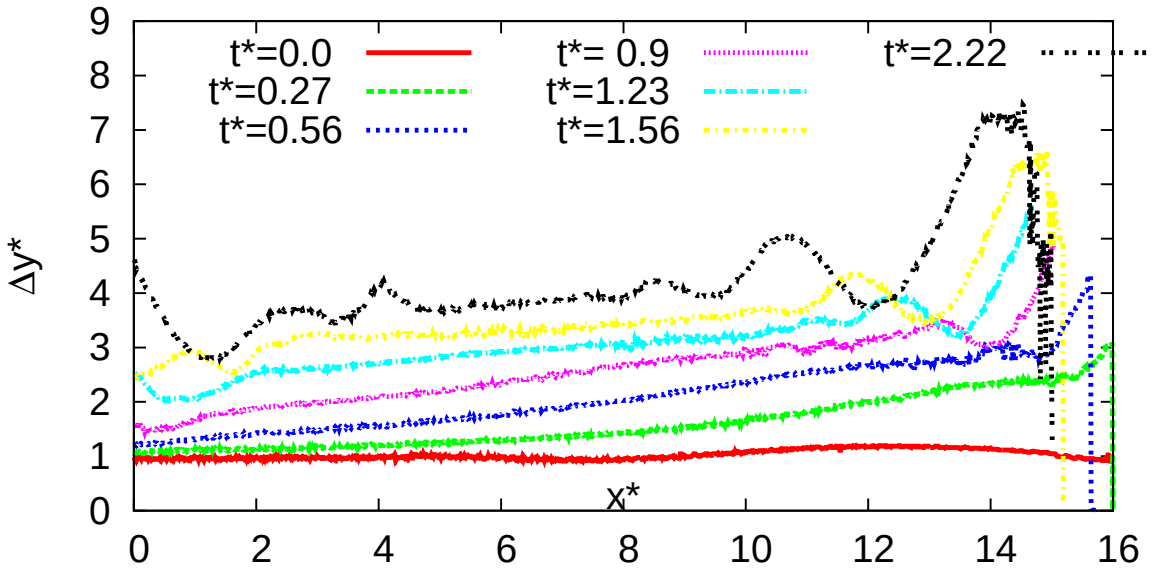

Abbildung 3.26.: Vortex spacing at different vortex ages after touch down, case 9.

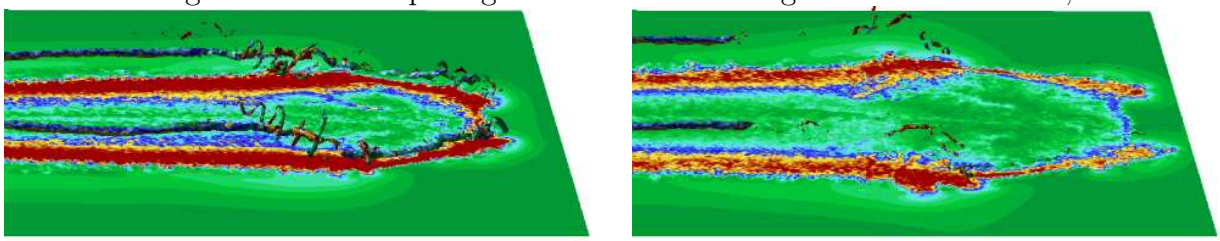

(a) $t^* = 0.15$ (b) $t^* = 0.29$

Abbildung 3.27.: Developing end effects after touchdown, case 9. Iso-vorticity surface $||\omega^*|| = 346$.

end effect, see Sec. 3.8.2. Note that the primary vortices quickly link with the ground leading to a stabilization of the primary vortices. The end effect is similar to the effects triggered by plate lines, detailed in previous sections. In addition the classical interaction of wake vortices with ground proceeds, i.e. secondary vortex structures separate from the ground and wrap around the primary vortices, see Fig. 3.28 (b) and (d). This ground effect, also observable in temporal LES, is independent of the end effects and depends only at the altitude of the vortices, the lower the flight height the earlier and more rapid the ground effect sequence proceeds. Hence, the propagation speed of the end effects and the ground effect do not coincide, see Fig. 3.28.

End effects can occasionally be observed when condensation trails form in humid air marking the vortex cores that adopt helical shapes and quickly disappear after touchdown.[1]

[1]Video available online at http://www.youtube.com/watch?v=oHGqxM1-rAI and http://www.youtube.com/watch?v=KqU70RORXtA [retrieved September 2013]

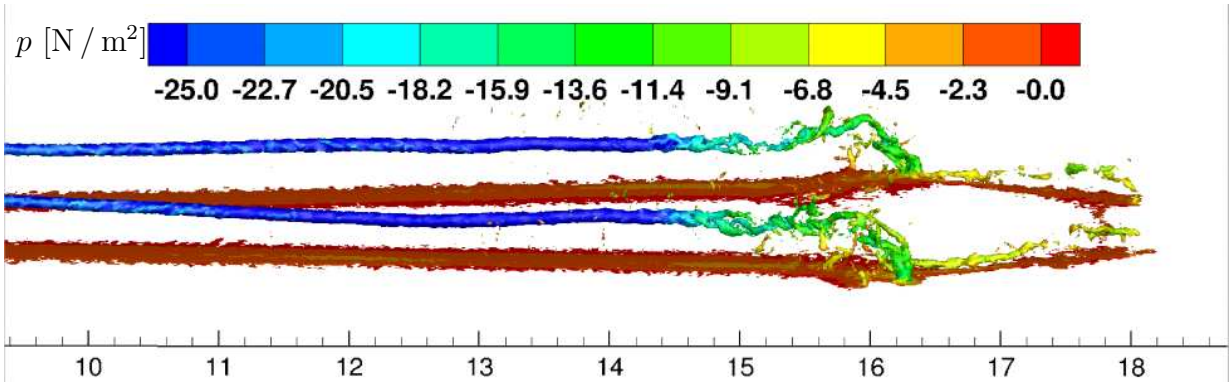

(a) $t^* = 0.28$

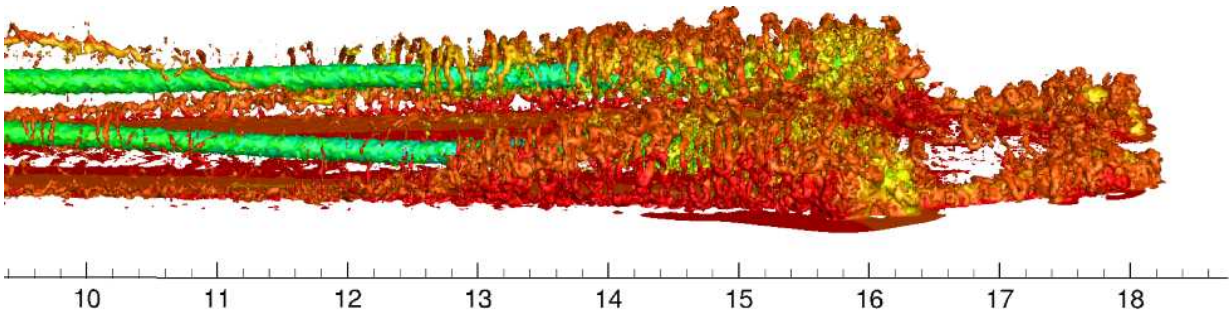

(b) $t^* = 0.28$

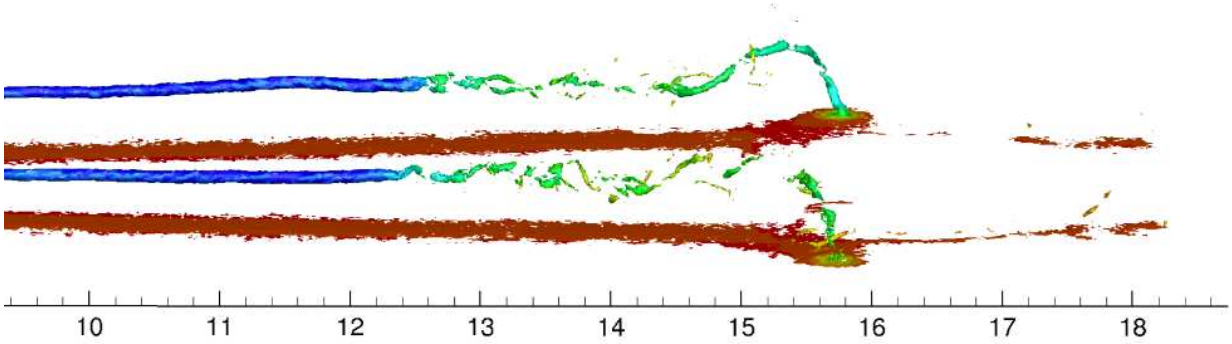

(c) $t^* = 0.56$

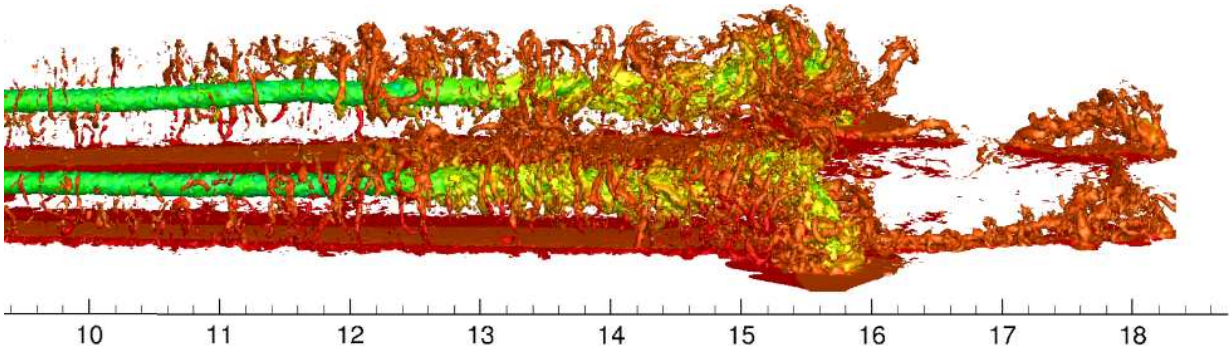

(d) $t^* = 0.56$

Abbildung 3.28.: Iso-vorticity surface $||\omega^*|| = 235$ (a) and (c) and $||\omega^*|| = 76$ (b) and (d), colored by pressure showing end effects as pressure disturbance and helical disturbance of the vortex core as well as ground effect for different time steps.

Condensation trails may occur when the temperature, lowered by the pressure decrease in the vortex core, leads to supersaturation of water vapor and thus to condensation. So the rapid disappearance of the condensation trail is directly related to the pressure and consequential temperature increase in the vortex cores.

In the simulation the vortices tend to reconnect with the ground, or equivalently formulated with their image vortices, which prevents them to dissolve further and thus conserves a certain level of circulation. Vortex linking with the ground has frequently been observed Proctor et al. (2000).

3.7. Wake Vortex Topology

The wake vortex topology in ground proximity features pronounced three dimensional behavior. Fig. 3.29 shows the complex development of the vortices after touchdown. The full computational domain is depicted showing also the back part, used for boundary treatment. The closing to a horse shoe vortex might be somewhat artificial, however wake vortex linking due to Crow instability is frequently observed in cruise altitudes Misaka et al. (2012a) and may also occur in ground proximity. Close to touchdown as well as in the back part we observe vortex linking with the ground, see Fig. 3.29 (a),(b). Beside the non-uniform divergence, see Fig. 3.29 (a), the rebound is non-uniform as well, in strong contrast to temporal LES. As the rebound is caused by secondary vortices, which are generated first at low flight altitudes the rebound starts close to the touchdown zone. The secondary vortices winding around the primary vortices, the end effects, and the ground linking deform the primary vortices to helical structures, see Fig. 3.29 (c). The vortex ends connected with the ground propagate against flight direction. The helix contracts. Evaluation in single slices, perpendicular to flight direction, displays the shift of that helix corresponding to peaks and kinks of the vortex altitude, see Sec. 4.2.2. Such a complex behavior is not known from classical temporal LES and might be also observed in reality. Vortex parts, that come close to the ground might also link, see Fig. 3.29 (d). In the LES a lateral domain width of $8.6b_0$ is employed, which does not completely cover the observed divergence, see Fig. 3.29 (d). This leads to unphysical vortex behavior at the boundaries, for example, excessive vortex rebound.

3.8. Vortex Decay and Core Radius Evolution

3.8.1. Flat ground

For circulation evaluation of the aircraft wake we take the center of the flap-tip vortex as the vortex center. Misaka et al. (2013) evaluates Γ_{5-15} for wing-tip as well as flap-tip vortex. There it is found that Γ_{5-15} centered at the flap-tip vortex covers the vorticity of the whole wake vortex. In cruise conditions the circulation Γ_{5-15} of the flap-tip vortex as well as the finally rolled up vortex is slightly larger than $0.9\Gamma_0$.

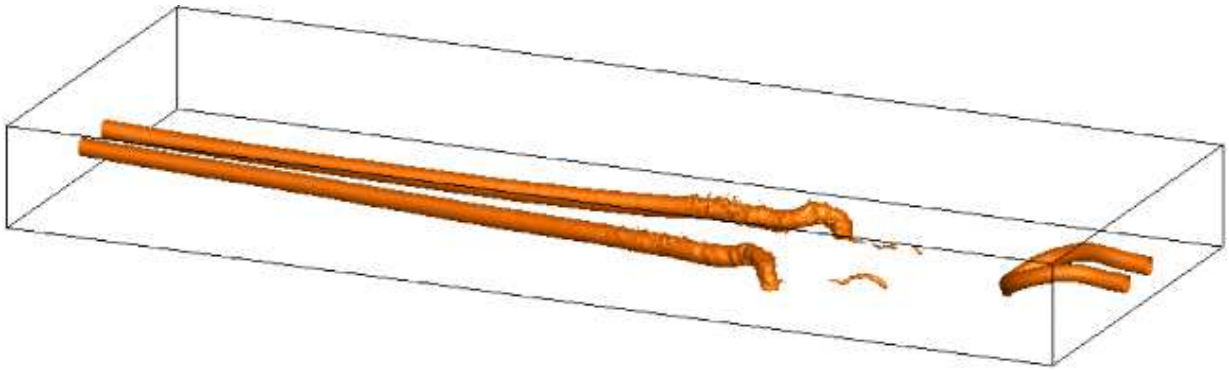

(a) $t^* = 0.42$

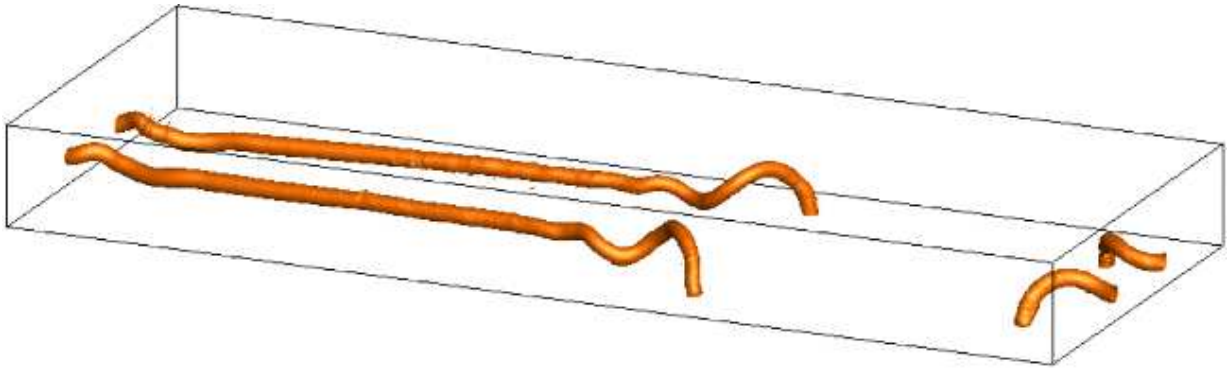

(b) $t^* = 1.31$

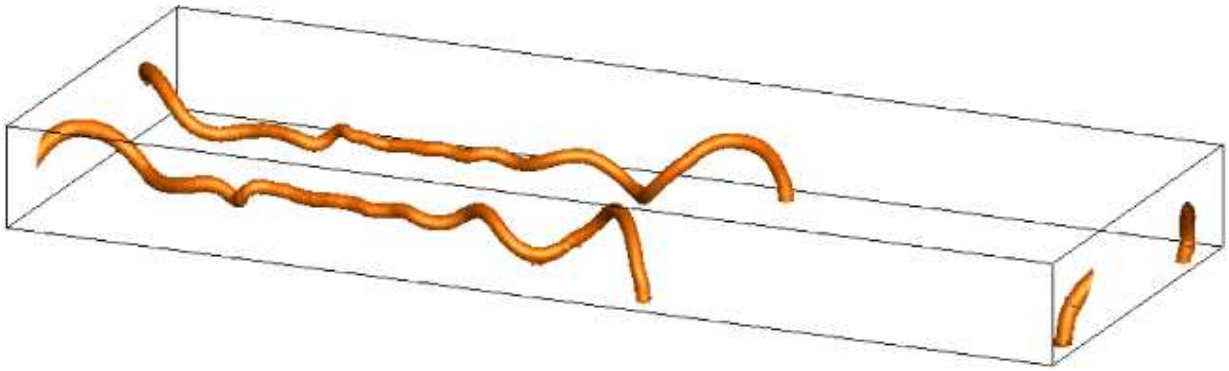

(c) $t^* = 2.38$

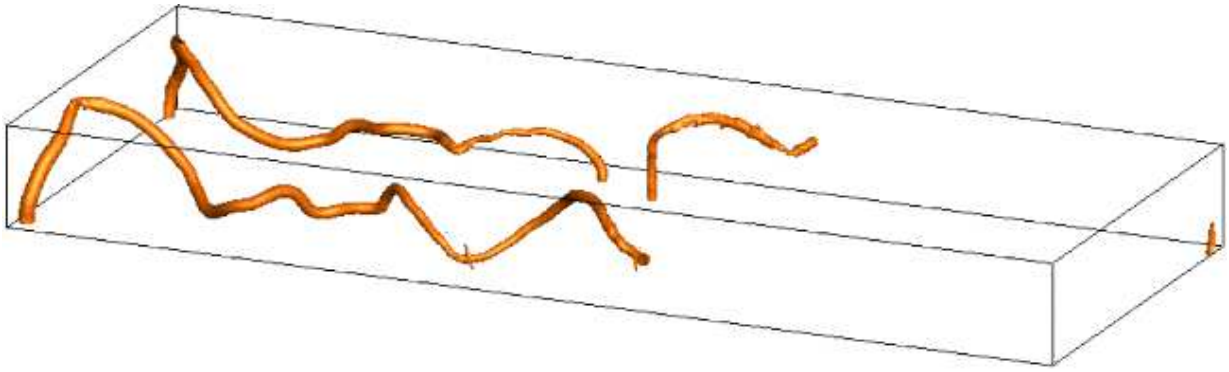

(d) $t^* = 3.71$

Abbildung 3.29.: Full computation domain. Iso-surface of pressure showing vortex filaments, case 9. Vortex ground linking, and linking with periodic boundaries.

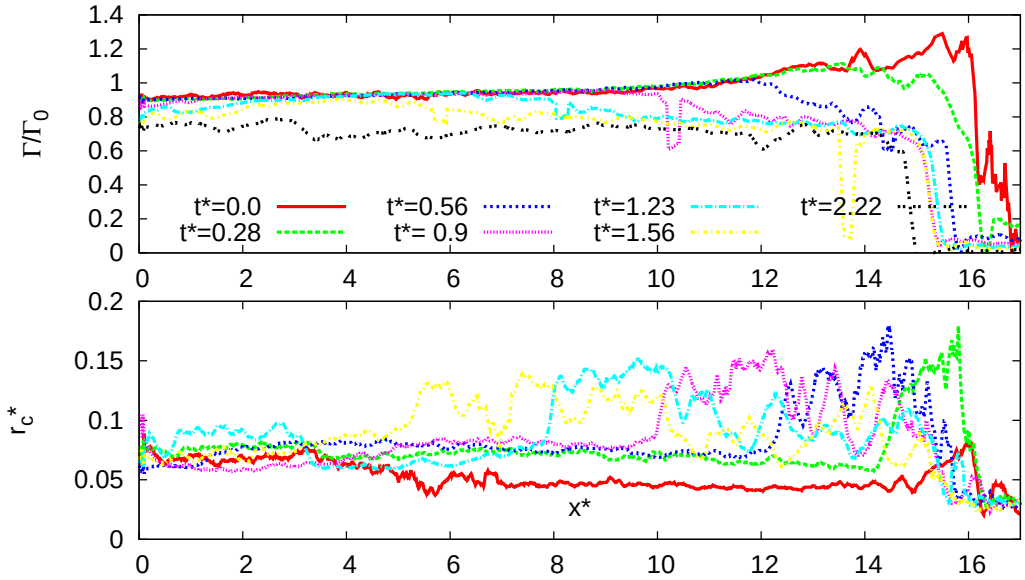

Abbildung 3.30.: Vortex circulation (Γ_{5-15}) distribution and core radius evolution, case 9, flat ground (Stephan et al., 2013b).

At the instant of touchdown we have an increasing circulation starting slightly larger than $0.9\Gamma_0$ at out of ground altitudes in accordance with Misaka et al. (2013), see Fig. 3.30. We clearly see the end effects after touch down, leading to a rapid circulation decay starting from the very ends of the wake vortices. The disturbance propagates until the end of the domain. In that case, without a plate line, the decay proceeds quite uniformly. The core radius, which is initially a bit too high, due to resolution limitations, increases drastically after touchdown. Together with the circulation decay the end effect causes an augmentation of the core radius to 300% of the initial value. The end effects propagate with an approximately constant speed of $U^*_{prop} = 7.1$ up to a time of $t^* = 2$.

3.8.2. Plate line effects

The effect of the plate line is clearly visible in Fig. 3.32 (b). Above the plate line, centered at $x^* = 5.1$, the circulation decay is initiated propagating subsequently to either side. The disturbances from the end effects as well as from the plate line superpose, leading to a more vigorous decay. In the region of the plate line we have a reduction of the circulation to less than 50%, whereas in case without the plate line the circulation falls to 70 % at $t^* = 2.2$, see Fig. 3.32. Note that the interaction of the end effect and the disturbance coming from the plate line leads to intriguing behavior of the core radius, see Fig. 3.31. The growth of the core radius is suppressed in the region of the plate line.

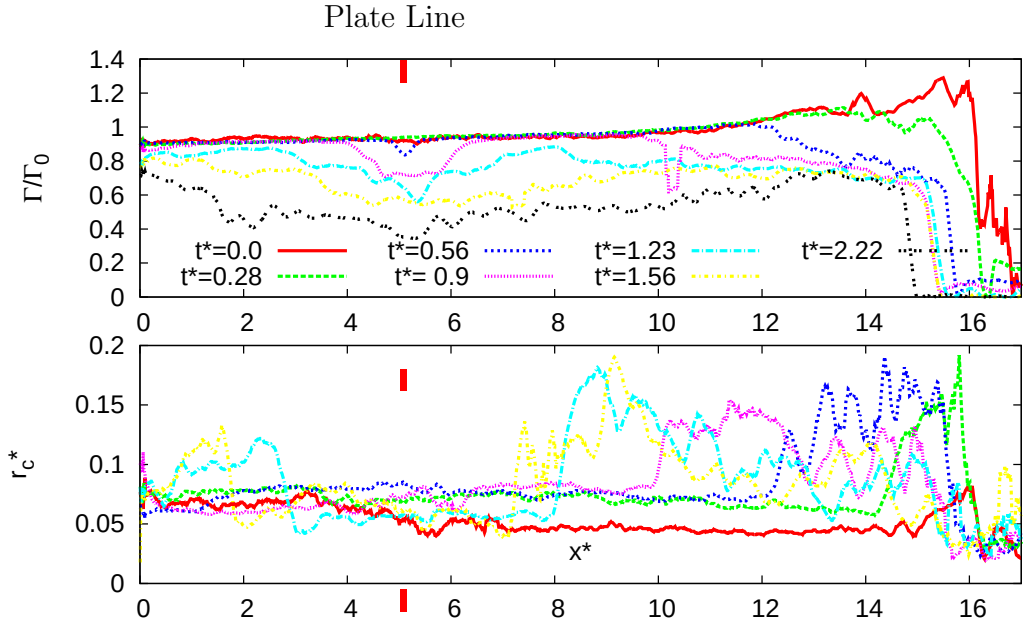

Abbildung 3.31.: Vortex circulation (Γ_{5-15}) distribution and core radius evolution, case 10, plate line (Stephan et al., 2013b).

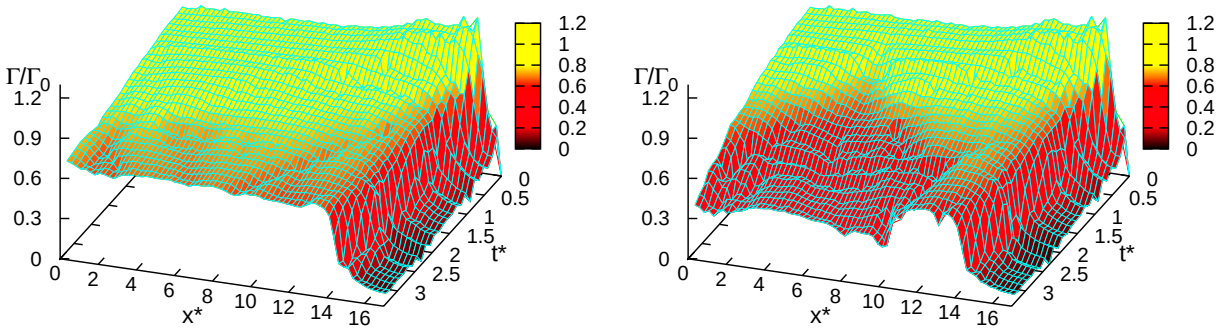

Abbildung 3.32.: Vortex circulation (Γ_{5-15}) distribution evolution after touchdown, case 9 and 10, flat ground and effect of a plate line (Stephan et al., 2013b).

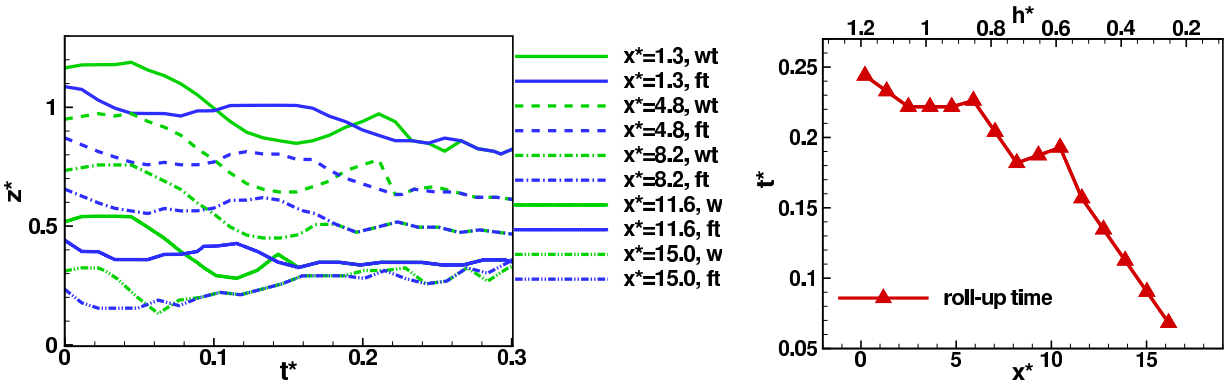

(a) (b)

Abbildung 3.33.: Roll-up of wing-tip (wt) and flap-tip (ft) vortex. (a) Altitude of vortices at different positions plotted until roll-up against time. (b) Vortex roll-up time depending on vortex generation height h.

3.8.3. Wake-vortex decay phases in ground proximity

Out of ground proximity the three vortex evolution phases, the *roll-up phase*, the *vortex phase* and the *decay phase* depend mainly on the meteorological conditions and proceed uniformly along the flight path. This crucially changes in ground proximity.

The roll-up phase is accelerated, depending on the generation altitude of the aircraft wake. Fig. 3.33 (a) depicts the roll-up process of the wing-tip and flap-tip vortex in different slices perpendicular to flight direction. Out of ground proximity, in accordance with Misaka et al. (2013), the roll-up is completed after approximately $t^* = 0.25$. Closer to the ground the distance between wing-tip and flap-tip vortex is progressively reduced, due to the influence of the ground surface. Fig. 3.33 (b) depicts the roll-up time depending on the generation altitude. Note, that the roll-up time decreases progressively.

In ground proximity also the wake vortex decay phases depend on the aircraft altitude. Due to end effects the vortex decay is strongly accelerated close to touchdown zone. To visualize the decay phases Fig. 3.34 shows the vortex circulation (color coded) against position and time. Fig. 3.34 (a) depicts a landing with flat ground. At time $t^* = 0$ the touchdown takes place. For negative times the the wake is initialized and rolls up. At $x^{=}0$, the domain boundary first and then shifted by flight speed. In cruise altitudes we would expect a uniform decay, the color coded pattern would have a parallelogram shape. A completely different pattern describes the decay characteristics during landing, schematically shown in Fig. 2.7. The end effect accelerates the decay and propagates against flight direction with a approximately constant speed, leading to the triangular pattern. The effect of a plate line on the decay phases is clearly visible in Fig. 3.34 (b). The triangular shape is changed. The plate line additionally reduces the vortex phase and rapidly initiates the decay phase leading to an irregular pattern.

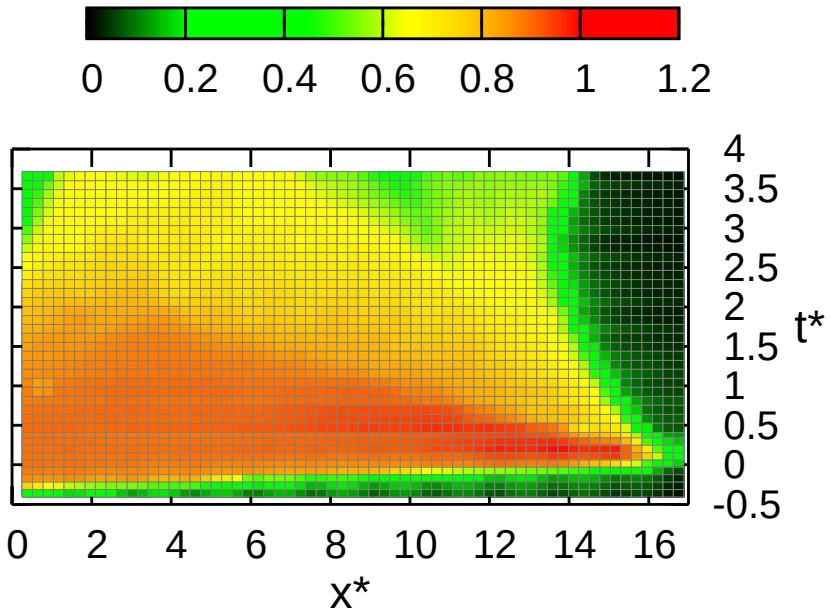

(a) flat ground

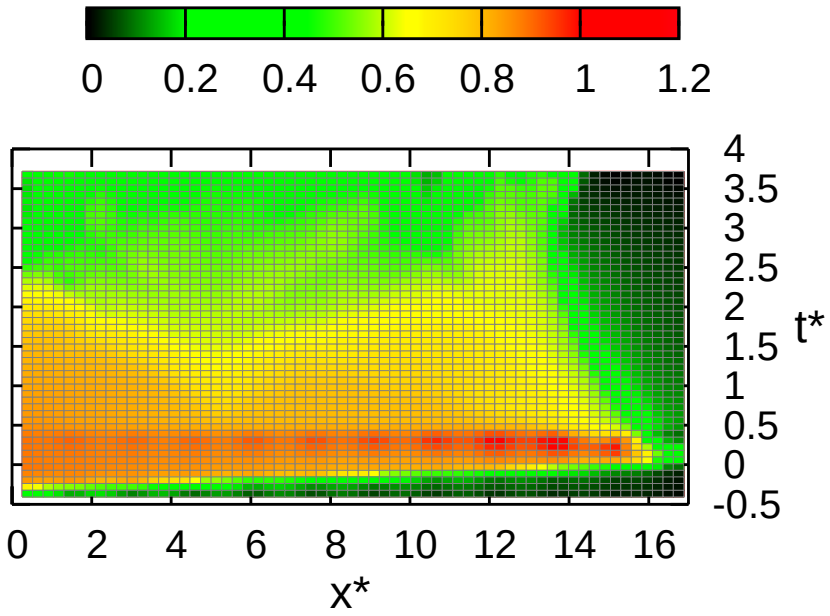

(b) plate line

Abbildung 3.34.: Vortex circulation (Γ_{5-15}/Γ_0) distribution (color coded), plotted against position x^* and decay time t^*, showing phases of vortex decay, case 9 and 10.

4. Discussion

The aim of this part of the thesis is to compare the results from LES with experiments performed in a water towing tank as well as results from field measurement campaigns at Frankfurt and Munich Airport.

4.1. Comparison of LES with Towing Tank Experiments

LES allows three-dimensional evaluation of arbitrary quantities derived from the velocity and pressure fields. The experiments only reveal the quantities derived from the imaging methods and are limited to low Reynolds numbers. On the other hand experiments reflect real fluid dynamics, so LES and towing tank experiments are complementary for analyzing flow phenomena. In order to ensure comparability of the two methods, a similar Reynolds number is employed. Beside, there is a main difference to towing tank experiments. In the experiments the vortices still need to roll up when they are generated at a height of $b_0/2$. However, unlike for high lift wing configurations, vortex sheets shed off uniformly and in clean configuration the roll-up is finalized very fast (Misaka et al., 2012a). Thus we assume, that after the roll-up process LES and experiments compare approximately. Directly above the obstacles the roll-up effect may lead to differences to the LES results, though.

4.1.1. Experimental setup - water towing tank

A detailed description of the experimental set-up can be found in Geisler & Konrath (2012) and Stephan et al. (2013c). Here the main properties are shortly recapitulated. The experiments have been conducted in the DLR water towing tank in Göttingen termed Wasser Schleppkanal Göttingen (WSG). This facility consists of an 18 m long tank with a cross-section of 1.1 m $\times$1.1 m equipped with a carriage capable of crossing the tank at a maximum speed of 5 m/s. Models under investigation can be attached to this carriage and are propelled along the tank at defined velocities while the water inside the tank is at rest. Compared to a recirculating water tunnel, this approach permits measurements far behind the aircraft model, i.e. old vortex ages. In order to achieve low turbulence levels the water in the tank was left to rest for at least 20 minutes prior to each run.
To minimize the influence of the towing tank side walls, a minimum distance of one model span between walls and vortices is required. To ensure this limit, a small version of the DLR F13 aircraft model was build, see Fig. 2.12 (b). This model has a rectangular wing with a span of 175 mm and a chord length of 35 mm.

The profile is a Wortman FX63-137B-PT. Embedded in the wing tips are outlets for contrast agents to trace the vortex cores. The model is supported by a profiled strut attached to the carriage via a translation stage. By this means the vertical position of the model can be adjusted. For the present experiments, the angle-of-attack is set to 10 degrees and the tail wing is replaced by a cone tail. The initial measured vortex separation is $b_0 = 153\,\mathrm{mm}$, the model is towed with 2.44 m/s through the tank, which leads to an initial measured circulation of $\Gamma_0 = 0.052\,\mathrm{m}^2/\mathrm{s}$, an initial measured descent speed of $V_0 = 49\,\mathrm{mm/s}$ and a resulting reference time $t_0 = b_0/V_0 = 3.1\,\mathrm{s}$. The corresponding Reynolds number is $\mathrm{Re} = \Gamma_0/\nu = 52{,}000$, with $\nu = \nu_{water} = 10^{-6}\,\mathrm{m}^2/\mathrm{s}$. These values are used for normalization in the experimental setup. Flat ground, one bar-shaped obstacle as well as two obstacles with a separation of $\Delta x/b_0 = 7.2$ have been investigated.

The velocity vector fields (u, v, w) of the wake vortices are measured in a certain plane by means of a time-resolved stereo particle image velocimetry (PIV) system. Polyamide particles of 20μm average diameter and $1.03\,\mathrm{g}\,/\,\mathrm{cm}^3$ density are suspended into the water and illuminated as tracer particles. Since PIV provides only local planar information on the wake vortices, vortex core visualization has also been applied. Driven by gravity, black ink from a vessel 0.5 m above the water surface is fed into the tube system of the model and finally released into the vortex cores through outlets at the wing tips. The ink traces are recorded with background illumination from above the tank by a consumer grade HD video camcorder.

Depending on the time separation of recorded images, the uncertainty of the velocity is estimated to $2\,\mathrm{mm}\,/\,\mathrm{s}$ to $20\,\mathrm{mm}\,/\,\mathrm{s}$ that corresponds to about $1 - 2\%$ of the maximal velocity in the flow field.

4.1.2. Numerical setup

In the simulations a computational domain size with dimensions $L_x = 384\,\mathrm{m}$, $L_y = 288\,\mathrm{m}$, $L_z = 96\,\mathrm{m}$, see Fig. 4.1, is used. This corresponds to approximately $8b_0 \times 6b_0 \times 2b_0$. The interaction of wake vortices with obstacles develops in all three spatial directions. The axially propagating disturbance requires a large extent of the x dimension to exclude boundary effects. The simulations cover the range that was used for the investigation of two obstacles in the experiments. The initial height of the vortex pair is set to $h_0 = b_0/2$. The number of grid points are $N_x = 512$, $N_y = 384$, $N_z = 192$, leading to a total of 37.7 millions grid points. In vertical direction the mesh is stretched geometrically up to a height of b_0 and then continued equidistantly. For comparison with the experimental vortex core visualizations in the LES a passive tracer concentrated in the core is initialized.

4.1.3. Simulation

In contrast to the wake vortex decay mechanisms presented before driven by the turbulence originating from the ground surface there is another origin of turbulence here which is the turbulent strut wake, see Fig. 4.2. The turbulent strut wake was modeled with an approach described in Sec. 2.2.2 and was initialized across the entire domain in vertical direction

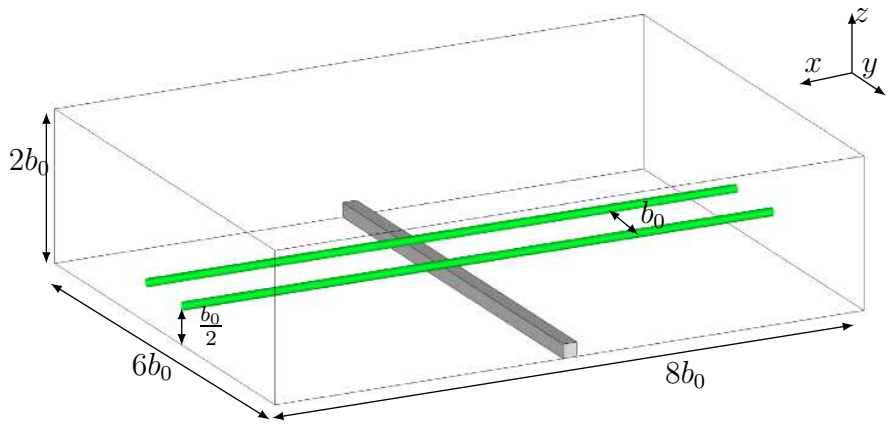

Abbildung 4.1.: Schematic of the computational domain, case 4, with the initial vortex position and an obstacle (Stephan et al., 2013c).

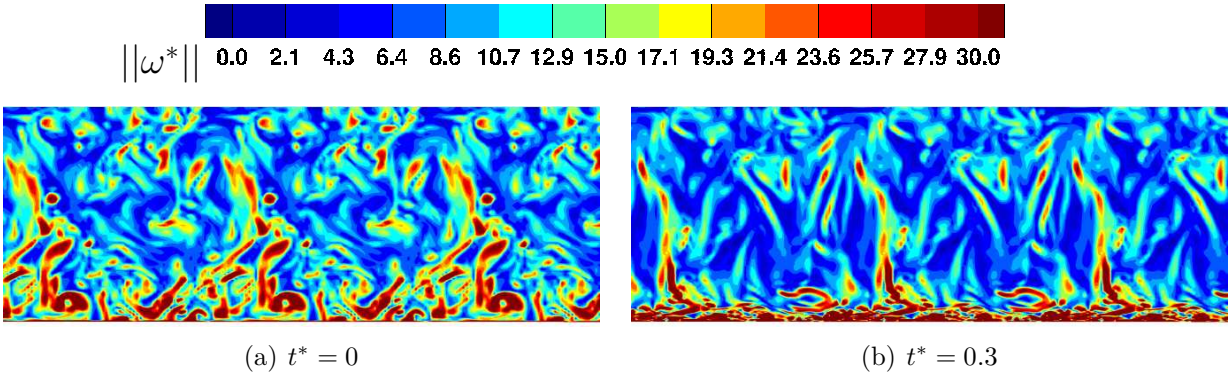

(a) $t^* = 0$ (b) $t^* = 0.3$

Abbildung 4.2.: Stretching and tilting of wake turbulence initialized between the primary vortices across the entire domain, case 5. Center slice colored by vorticity magnitude $||\omega^*||$ (Stephan et al., 2013c).

using a cutoff function horizontally, as described in Sec. 2.6.2. The turbulent structures, depicted in Fig. 4.2, are stretched around the primary vortices and quickly transported to the ground between the vortex pair, disturbing the formation of the secondary vortices. Hence, the secondary vortices interfere with the turbulent strut wake already during their formation leading to highly irregular vorticity patterns. The counter-rotating secondary vortices finally develop into relatively strong turbulent structures initiating rapid vortex decay of the primary vortices. Fig. 4.3 (left) shows how those secondary vorticity structures (SVS) develop from the ground effect vortices.

Exactly as in the previously presented case with crosswind the obstacle changes the flow field significantly. At the top of the barrier secondary vorticity is generated rapidly after vortex initialization, which subsequently detaches and develops a distinct loop, see Fig. 4.4 (right). The loop is stretched and winds around the primary vortex forming an omega-shape, which is approaching to and subsequently immersing into the primary vortex. The process follows the vortex stretching and tilting mechanisms detailed in Sec. 3.3.2. Again

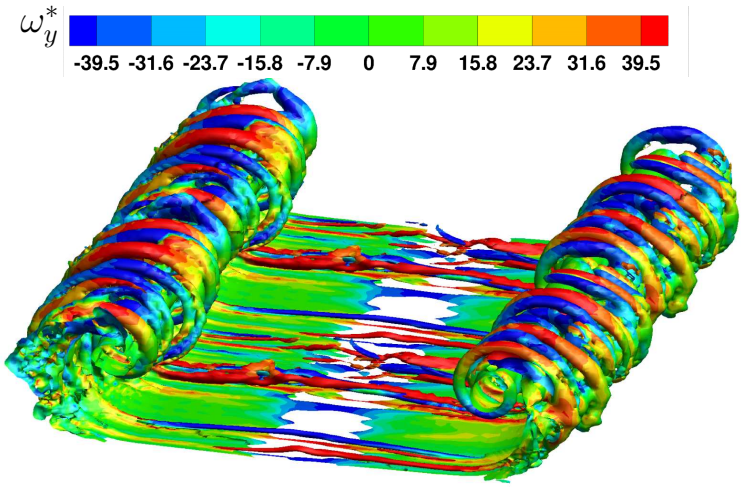

Abbildung 4.3.: Iso-surfaces of $||w^*|| = 79$ colored by vorticity strength ω_y^* in spanwise direction at $t* = 0.91$, case 5. Cutout from the original domain. Roll-up of secondary vortex structures generated by strut turbulence (Stephan et al., 2013c).

the geometrically induced SVS travel along the primary vortices driven by self-induced velocity induction, until they collide at the boundary of the periodic domain. Comparing the evolution of the wake vortex pairs over flat terrain (Fig. 4.4, left) and over terrain with the obstacle (right) the rapid and vigorous decay triggered by the obstacle can be observed.

4.1.4. Experiment

In the case of a square obstacle (cross section $0.2b_0 \times 0.2b_0$ as in the LES) oriented perpendicular to the towing direction, see Fig. 4.5 (left), disturbances emerging and propagating with and against flight direction from the point where the vortex first hits the obstacle can be observed. So the ink is transported in axial directions to both sides. LES show similar behavior, see Fig. 4.5 (right) and reveal that these disturbances are correlated with the forefront of the wound up secondary vortices generated at the obstacle. Although in the experiments the secondary vortices can not be explicitly observed they are implicitly visible in virtue of their action upon the primary vortices. The bursting of the vortex core during the passage of the disturbance is associated with an agglomeration of the tracer marked fluid at the head of the disturbance in both experiment and simulation.

PIV recordings are taken in vertical planes directly above the bar and at different distances from it,
$\Delta x^* = 0, \Delta x^* = 1.05$, and $\Delta x^* = 3.6$ and at a single position in case of flat ground. From the gained time-resolved 3-component velocity vector fields properties like vorticity and vortex circulation as well as vortex core traces are evaluated. In Fig. 4.6 a patchy vorticity layer with opposite sign is generated at the ground. The strut wake turbulence is clearly

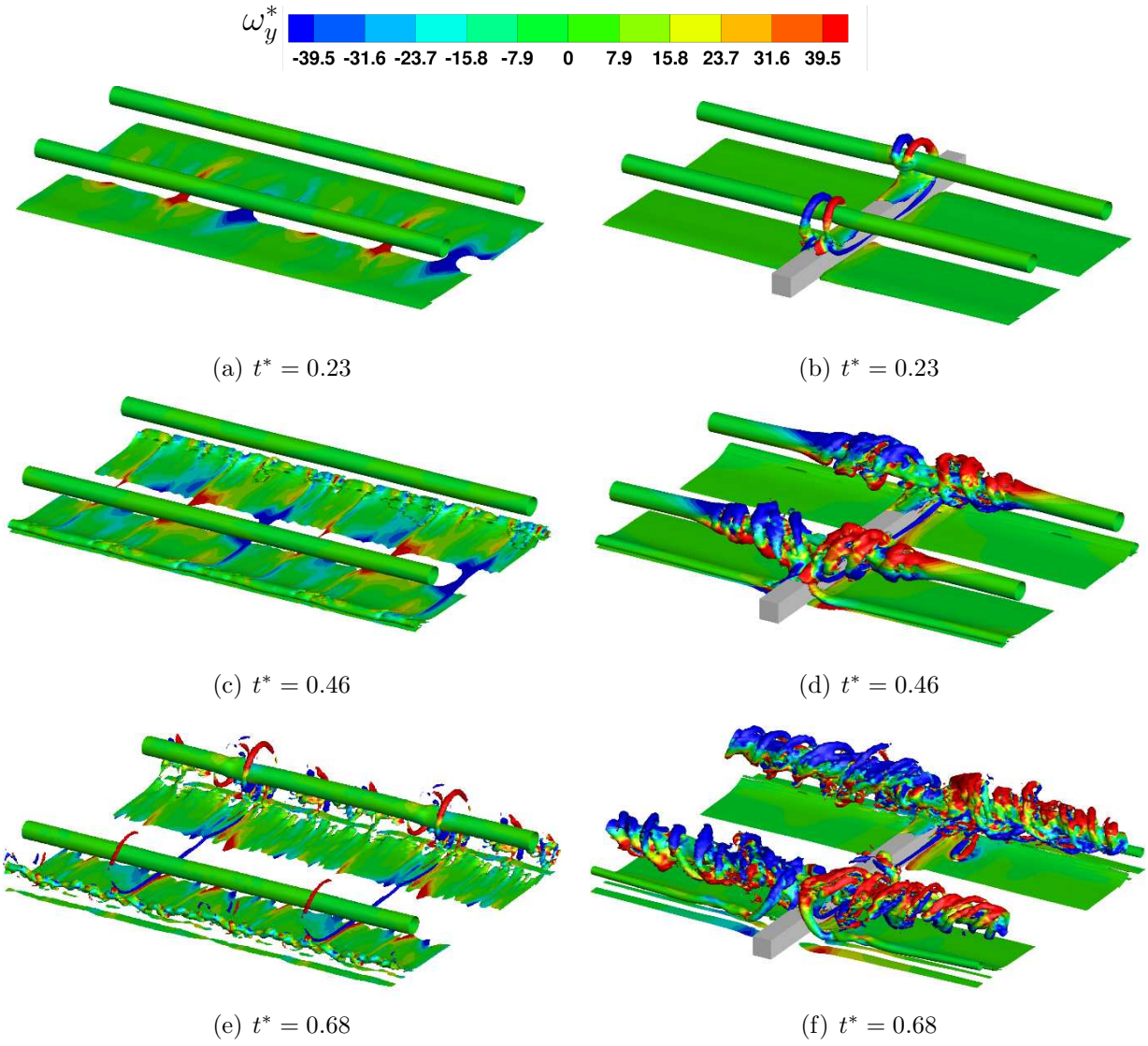

(a) $t^* = 0.23$ (b) $t^* = 0.23$

(c) $t^* = 0.46$ (d) $t^* = 0.46$

(e) $t^* = 0.68$ (f) $t^* = 0.68$

Abbildung 4.4.: Wake vortex evolution without (left, case 5) and with square-shaped obstacle (right, case 4) at the ground. Iso-surfaces of $||w^*|| = 79$ colored by vorticity strength ω_y^* in spanwise direction. Cutout from the original domain (Stephan et al., 2013c).

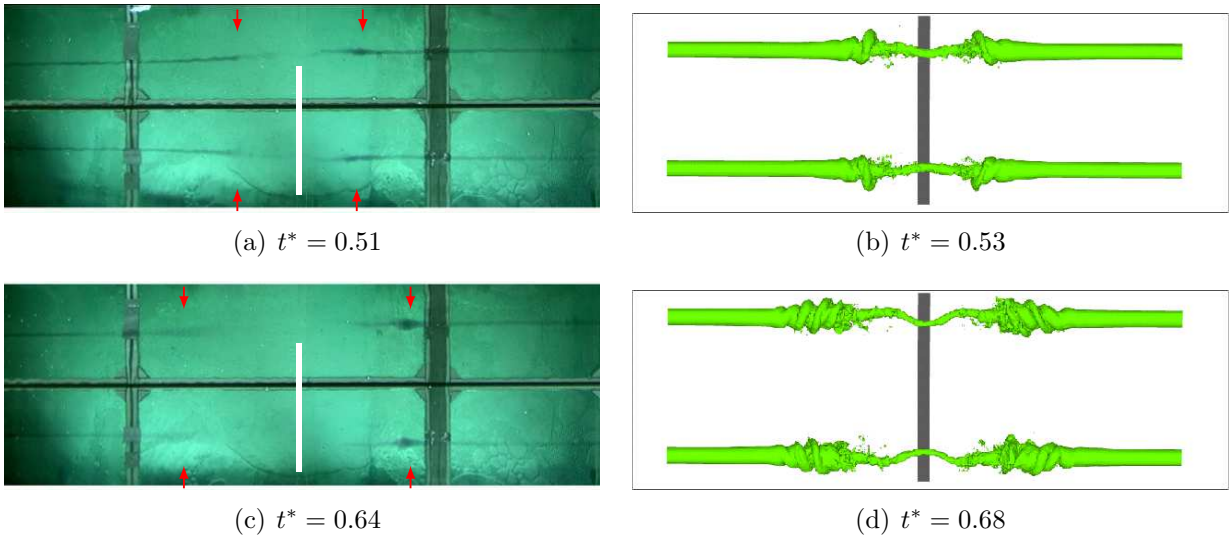

(a) $t^* = 0.51$ (b) $t^* = 0.53$

(c) $t^* = 0.64$ (d) $t^* = 0.68$

Abbildung 4.5.: Obstacle effects. Vortex cores visualization in towing tank (a) and (c), LES with passive tracer, case 4, (b) and (d). White bars show the obstacle position. Arrows pointing at disturbance caused by obstacle (Stephan et al., 2013c).

visible at $t^* = 0.3, y^* = 0$. In a circular region around the primary vortex patchy vorticity of opposite sign, corresponding to SVS detached from the ground, can be observed. The vortex does not rebound significantly in the region of the obstacle but stays close to it. Already at $t^* = 1.6$ the vortex is much more weakened above the obstacle than above flat ground. Vorticity distributions and velocity vectors indicate that at $t^* = 2.9$ the vortex at the obstacle has already substantially lost its strength.

4.1.5. Trajectories and decay

The primary vortex centers are tracked detecting local centroids of vorticity distributions in the PIV measurements Konrath et al. (2009). Experimental data depicted in the plots in this paragraph represent quantities in the observation plane averaged over 3 to 5 runs. Note that in LES periodic boundary conditions are used. So interpreting the simulations correctly, not the influence of a single obstacle is calculated, but periodically arranged obstacles with a separation equal to the domain length. However until the disturbance reaches the domain boundary in flight direction which occurs roughly at $t^* = 1$ the influence of other obstacles can be neglected enabling a fair comparison with experiments.

Fig. 4.7 shows the impact of an obstacle on wake vortex rebound height. Initialized at $b_0/2$ the primary vortices rise in the experiments to a height of about $1.2b_0$ above flat ground, Fig. 4.7 left. Above the obstacle the rebound height is very much reduced. The maximal rebound height increases with the distance to the obstacle. Note that at a distance of $3.6b_0$ the rebound height exceeds the height above flat ground. The results from LES show similar characteristics, see Fig. 4.7 right, despite pronounced scatter due to very

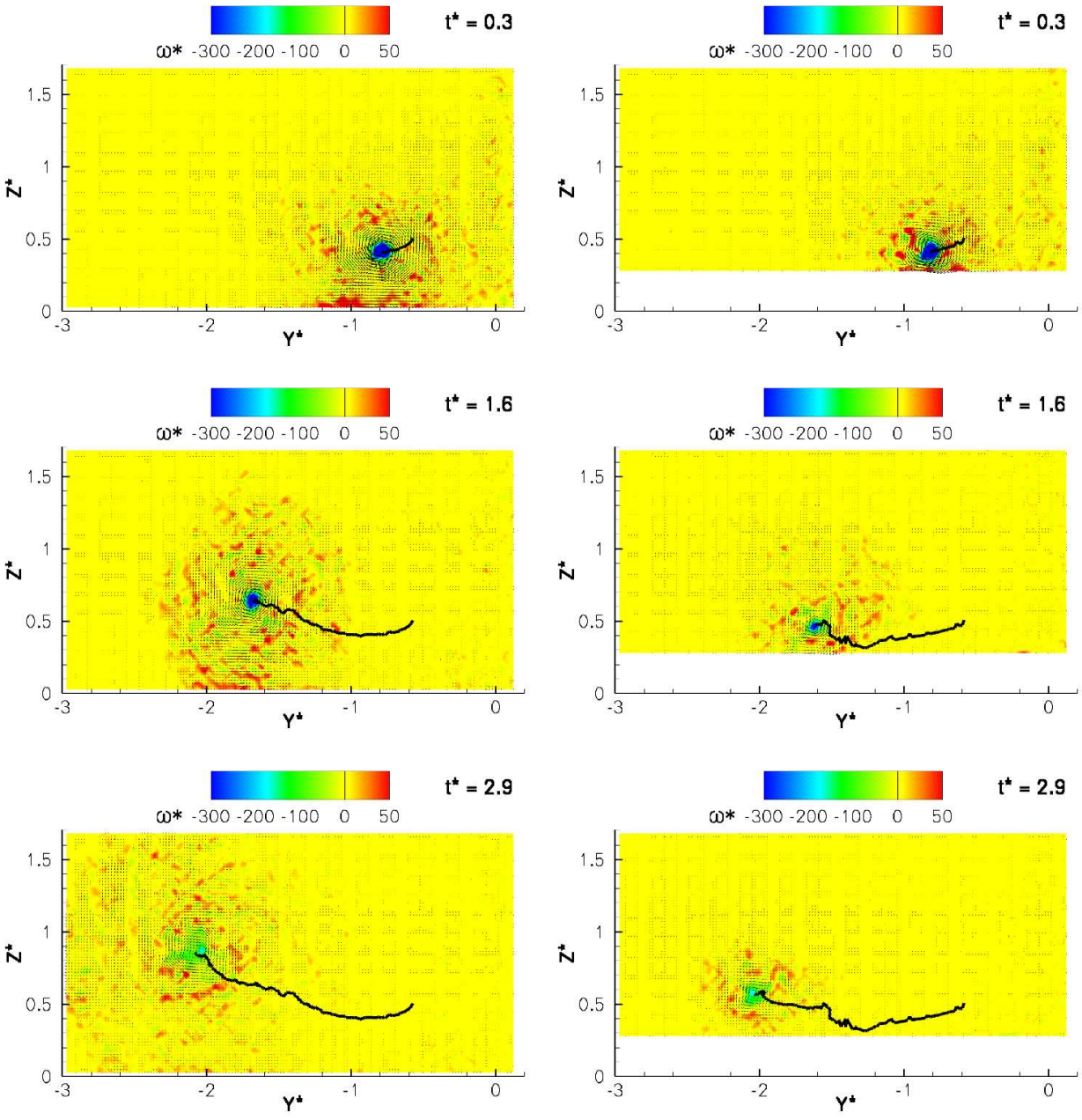

Abbildung 4.6.: Vorticity (color coded), velocity (tiny vectors) and vortex tracks (black lines) measured by PIV above flat ground (left) and above the obstacle (right). (Stephan et al., 2013c)

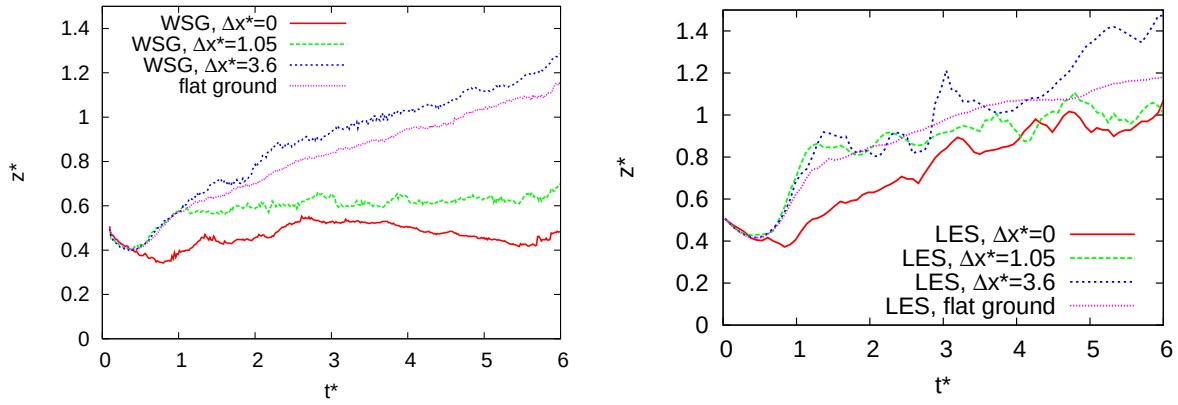

Abbildung 4.7.: Vortex trajectories derived from PIV (left) and LES (right, case 4 and 5), at different distances from a $0.2b_0 \times 0.2b_0$ square obstacle and above flat ground (Stephan et al., 2013c).

disturbed and incoherent vortices and the fact that just one single run is evaluated. The tendencies coincide, however more fluctuations in the LES are observed as well as a higher rebound height at all distances. Particularly the rebound heights at $\Delta x^* = 1.05$ and at $\Delta x^* = 0$ are much larger in the LES.

As a measure of vortex strength the physically interesting $\Gamma_{\max}$, see Se. 2.1.6, is compared as it reveals the actual maximal strength of a vortex. Above the obstacle a tremendous reduction of circulation during the first t_0 is observed. Both experiments and simulations feature a rapid reduction to about 40% of the initial circulation, see Fig. 4.8 (a) and (b), whereas somewhat lower circulation values are achieved in the towing tank. By contrast, in case of a flat ground the circulation does not change significantly during this early time period. Further away from the obstacle the circulation is also reduced faster and further. At a time of $t^* = 1$ above the obstacle the steep decrease of circulation stops abruptly and recovers to a slightly higher level. This occurs in experiments as well as in LES. Particularly in the LES the circulation recovers in slices apart from the obstacle. Qualitatively, experiments and LES agree very well, see Fig. 4.8 (b) to (d). Throughout substantial parts of the development also quantitatively good agreement is found. However, the circulation is further reduced in experiments than in the LES for times larger than $t^* = 3$ in both cases with or without obstacle except at $\Delta x^* = 3.6$. The idealized conditions in the LES seem not to include all relevant sources of turbulence that influence the decay. In Fig. 4.8 (d) we observe strong deviations of LES results from the experiments at $\Delta x^* = 3.6$ after a time $t^* = 1.8$. This can be explained by effects of the periodic obstacles, that have to be taken into account at this position and further reduce the circulation.

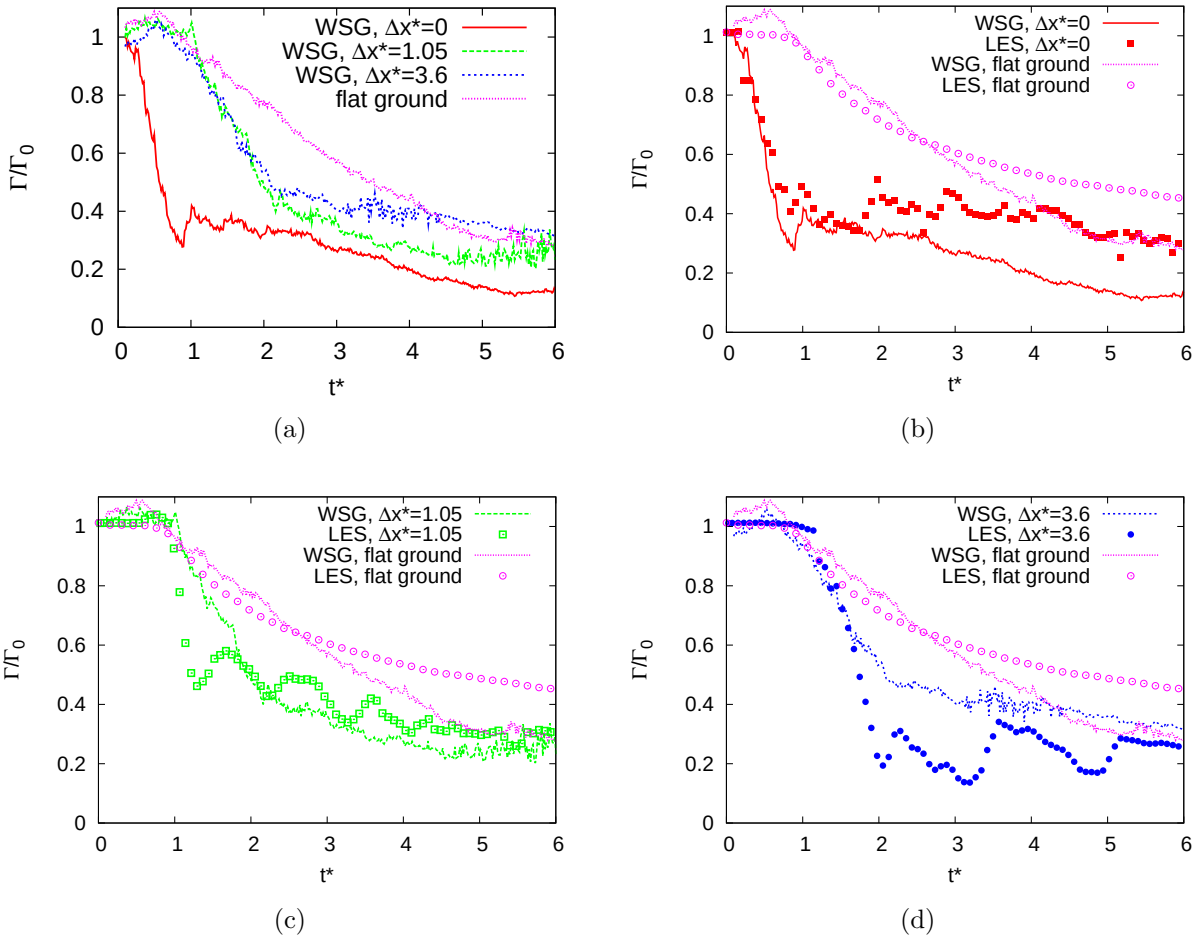

Abbildung 4.8.: Vortex circulation maxima Γ_{max} derived from PIV (a) and comparison with LES, case 4 and 5, (b), (c) and (d) at different distances from a square obstacle (Stephan et al., 2013c).

4.1.6. Propagation of end effects

In this paragraph the propagation speed of the helical disturbance, which we also call end effects, induced by obstacles in LES as well as in experiments is compared. In the experiments the disturbances travel either in towing direction or against it, see Fig. 4.5. From the video a propagation speed of 0.5 m/s or 0.4 m/s can be estimated, respectively, which corresponds to 0.45 m / s if we cancel out the flow speed stemming from the model wake. Hence the propagation speed normalized by the wake vortex descent speed equals $U^*_{hel} = 9.2$.

The initial core radius of the primary vortex in the experiment is 0.0085 m. Assuming that the circulation, ring radius and core radius of the secondary vortex scale with the corresponding circulation and the core radius of the primary vortex, Eq. 3.1 provides a propagation speed of 0.34 m / s again underestimating the observed value of 0.45 m / s. Hence, Eq. 3.1 supports scaling of the propagation speed between experiments and LES to first order and enables to estimate the propagation speed of the disturbance depending on initial circulation and primary vortex core radius. The experiments provide a scaling factor $A = U^*_{hel}/U^*_{ring}$ of 1.32. These results suggest that a fair approximation of the propagation speed of the helical disturbance may be achieved employing a correction factor of about 1.4.

4.1.7. Effects of several obstacles

Considering more than one obstacle leads to the question how the previously discussed disturbances interact when they collide. Assuming sufficiently large separations of the obstacles no interaction of the omega-loops occurs at the early stage of the flow but during the propagation along the primary vortices. Note two main differences between simulation and experiment. While in our setting simulations with streamwise periodic boundary conditions can not avoid the influence of neighboring obstacles several obstacles in the experiments are employed on purpose.

Second, in our simulations fully rolled-up vortices approaching both obstacles at the same time are assumed. Consequently this is a symmetric situation, where the collision of the propagating disturbances occurs exactly in the center between two obstacles. In the experiments the second obstacle will influence the wake vortex with an offset in time proportional to the towing speed whereas in real approaches to an airport the flight speed is partly compensated by the aircraft descent. As a consequence the point of collision of the disturbances is shifted axially. Hence in LES there is a symmetric situation whereas an asymmetric one in experiments and reality.

The collision of the propagating disturbances can be seen in the snapshots at $t^* \sim 0.8$ taken from the towing tank experiments with two obstacles, see Fig. 4.9 (left). For visualization of the simulations with a passive tracer in Fig. 4.9 (right) one half of the domain is cut and connected from the other side to the other half domain.

Approaching disturbances coming apparently from two obstacles and an accumulation of fluid marked by a tracer initialized in the vortex core can be observed in both experi-

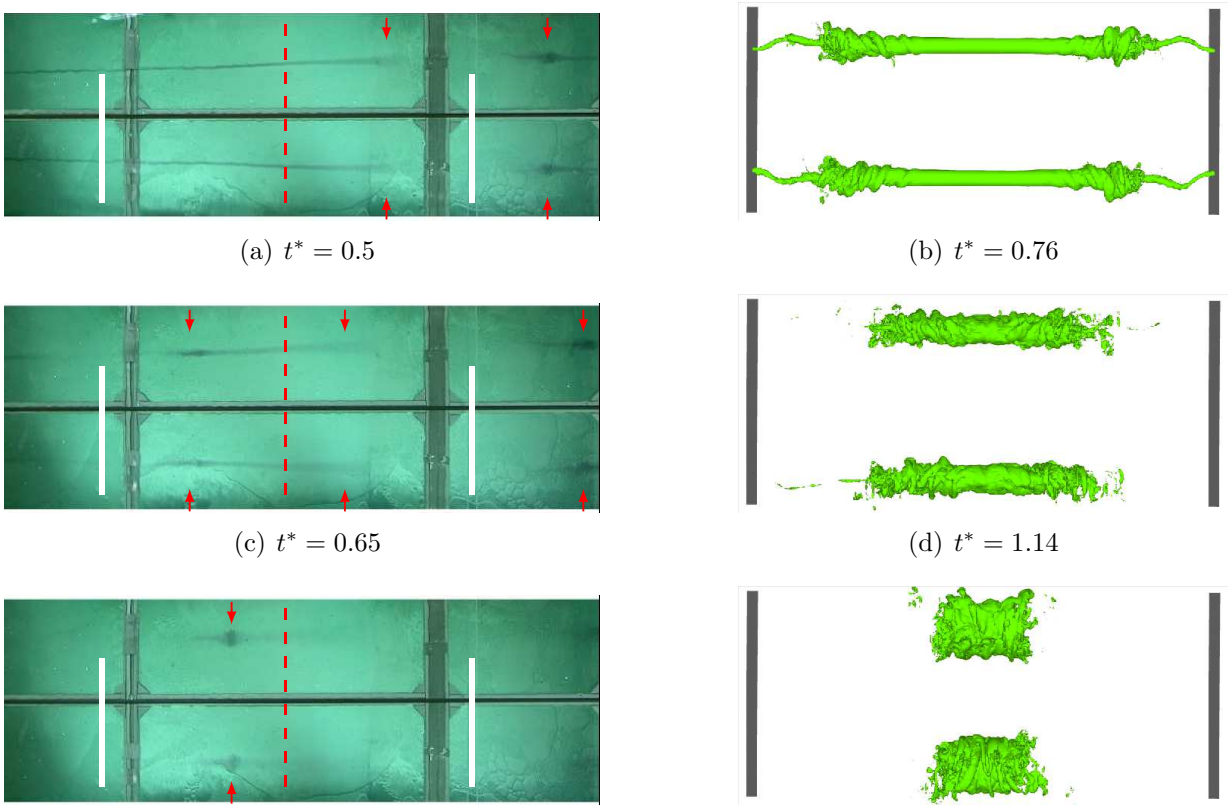

(a) $t^* = 0.5$ (b) $t^* = 0.76$

(c) $t^* = 0.65$ (d) $t^* = 1.14$

(e) $t^* = 0.77$ (f) $t^* = 1.52$

Abbildung 4.9.: Effect of two obstacles. Vortex core visualization in towing tank with ink (a),(c) and (e), obstacles left and right, dashed line PIV measurement plane, distribution of passive tracer in LES, case 4, (b),(d) and (d) (Stephan et al., 2013c).

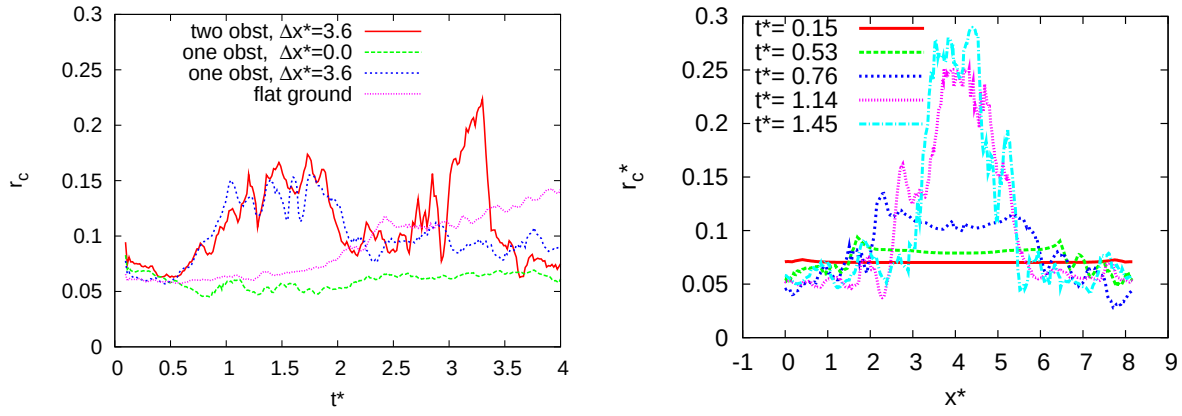

Abbildung 4.10.: Development of vortex core radius derived from PIV (left) for different distances from the obstacle and from LES along the vortex center line, case 4, (right) for different vortex ages.

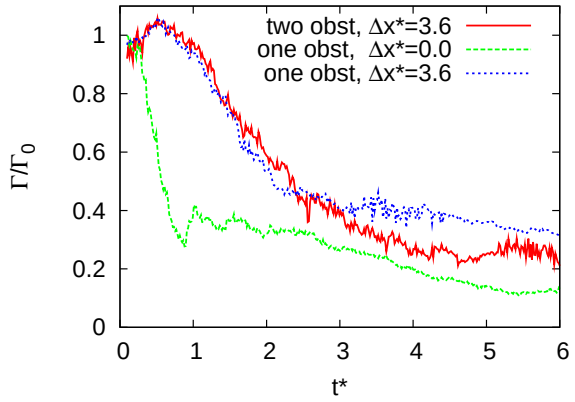

Abbildung 4.11.: Vortex circulation maxima Γ_{max} derived from PIV (left) at different distances from one or two $0.2b_0 \times 0.2b_0$ square obstacles (Stephan et al., 2013c).

ment and simulation. Eventually the disturbances collide and the vortex bursts. The good qualitative agreement between experiment and simulation provides confidence in the two methods and the interpretation that the tracer is actually transported and accumulated at the head of the propagating disturbances. Similar effects are discussed thoroughly in Ref. Misaka et al. (2012b).

Fig. 4.10 shows the development of the core radius for different configurations in the experiment (left) and the LES (right). The core radius maxima in the experiment are caused by the disturbance passing the measuring plane in the setup with two obstacles. First after the passage of the disturbance propagating in towing direction at $t^* = 1.5$ and then after the passage of the disturbance against towing direction at $t^* = 3$. Core radii increase almost fourfold during the passage of the second disturbance. Once more the circulation reduces significantly, see Fig. 4.11, compared to the case with one obstacle. After the passage of the disturbances the core radius shrinks again. On the other hand, in simulations a growing core radius at the front of the helical vortex train is observed, which is further increased again by a factor of four, where the disturbances collide. This is consistent with the bursting ink traces in the snapshots in Fig. 4.9 where also maximum core radii occur where the disturbances collide. Beside the helical vortex train the core radii also shrink in the simulation, see Fig. 4.10 (right).

4.2. Comparison with field measurement campaigns

The presented simulation results are derived for low Reynolds number vortex flow or a wall model was employed. These low Reynolds number investigations need to be assessed at realistically high Reynolds numbers to determine how the results apply to real aircraft and potential reduction of ICAO separations. Also it is impossible to achieve realistically high Re in towing tanks. Hence, flight experiments are mandatory to prove the stated effects in reality. However, it is known from flight measurements (Holzäpfel & Steen, 2007) that wake vortex trajectories, descent height and rebound characteristics, in ground proximity compare well with low Re simulations, see Sec. 4.2.1. Thus we may assume that the strength of secondary vortices is similar and the effects presented here scale well.

Real wake vortex flows have mainly been investigated by measurements with a LIDAR device (Constant et al., 1994), so far. An emitted laser beam is reflected and scattered by aerosols moving with the vortex flow. The detected signal provides the particle position and the phase shift of the photons reveals the velocity towards the detector by the Doppler-shift. Circulation as the most important parameter for wake vortex characterization can be evaluated (Holzäpfel et al., 2003a). New technologies using PIV systems at the airport have been proposed in Konrath et al. (2013), but applications to wake vortex flow still have to be performed.

From August to December 2004 a field measurement campaign has been performed at Frankfurt Airport (Holzäpfel & Steen, 2007) and another campaign from 11 March to 12 May 2011 at Munich Airport. At Frankfurt data of 288 landings has been collected whereas 779 wakes have been measured in Munich. A 2μ m pulsed Doppler LIDAR system (Köpp

et al., 2004; Smalikho & Rahm, 2010) scanned in a measurement plane perpendicular to the approach corridor at different distances to the runway. The initial wake-vortex height varied between 10 m and 100 m.

4.2.1. Frankfurt (WakeFRA)

The averaged normalized closest approach to the ground of the LES primary vortices is 0.49 for the upwind and 0.57 for the downwind vortex. LIDAR measurements at Frankfurt airport indicate average minimum altitudes of 0.525 and 0.62, respectively, in corresponding crosswind situations (Holzäpfel & Steen, 2007). The measured lateral displacement of the primary vortex trajectories scatters around a median of 3.2 at average vortex ages of $t^* = 3$ Steen (2005). The LES results show a lateral displacement of 3.2 at a time of $t^* = 3$. This good agreement of two key parameters indicates that the LES results may be representative for wake vortex evolution in ground proximity.

4.2.2. Munich (WakeMUC)

During the WakeMUC field measurement campaign 779 flights have been measured by Stephan Rahm and Rudolf Simmet, processed by Igor Smalikho, and evaluated by Stephan Körner, who kindly provided the resulting plots. For assessment of the LES results, of a landing aircraft (case 9), wake vortex trajectories from the simulations are integrated into the WakeMUC results, see Fig. 4.12-4.15. Normalized altitude z^* and wake-vortex separation Δy^* are depicted on the left side of each multiplot and vortex circulation averaged in temporal as well as circulation intervals on the right side.

Analyzing the vortex altitude we observe that LES data agrees very well with mean measured altitudes until $t^* = 3$ in all four cases for $z_0^* = 0.9$ and $z_0^* = 0.7$ even up to $t^* = 4$. However, the strong rebound for $z_0^* = 1.1$ and $z_0^* = 0.5$ exceed the 90% percentile. This is probably an unphysical result in the case $z_0^* = 0.5$ resulting from upwards velocity induction when the vortices approach the lateral periodic boundaries of the simulation domain, see Sec. 3.7. For the case $z_0^* = 1.1$ the vortex ground connection as well as contraction of the vortex helix causes the vortices to rise. Interestingly, the local rebound peaks observed in the LES data, see Fig. 4.12-4.15, are not present in the measured mean curves, however they clearly appear in the upper percentiles in all cases. Thus, the rebound peaks might be a physical vortex rebound characteristic which either does not scale with b_0 and hence vanish in the average or occurs rarely. Again, these local peaks can possibly be explained by the complex three dimensional vortex topology of a contracting and shifting vortex helix due to linking with the ground. For further investigation single flights have to be considered separately. As in the Frankfurt data the minimum vortex height from LES is below the measured average in all cases but still within the 90% envelope. Note, that as no wind is integrated in the LES we have to compare with the mean of luff and lee vortex position. The descent slope coincides well.

Vortex separation is found to agree well with measurements. The cases $z_0^* = 0.9$ and $z_0^* = 0.7$ resemble very well, see Fig. 4.13, 4.14. In Fig. 4.14 Δy^* from LES is slightly

above the mean curve. Only for low starting altitudes the separation strongly deviates. However the slope of the curves agrees well. Note that the measured values below 1 are unphysical. The initial separation was surely measured before the roll-up was completed, so a systematic error in some of the cases might exist because of normalization. A rescaling would lead to a much better agreement. Note further that just few measurement data are available at the respective altitudes. Overall it can be concluded, that the LES reproduce the wake vortex topology observed in the field measurement campaign quite well. The more pronounced deviations can be attributed to the impact of simulation domain boundaries. So the LES topology can serve as an explanation for particular measured trajectories giving insight into the three dimensional fields.

Averaging circulation in temporal intervals shifts the averaged values towards the long living vortices, due to the fact that the LIDAR has a certain threshold for the estimation of circulation. This gives an overestimated mean curve for large life times. As an unphysical consequence the mean circulation may even increase in the plots, see Fig. 4.12 (right, down). Averaging circulation in circulation intervals accounts for the fast decaying vortices, due to the fact that the long living vortices are quite much deformed and patchy such that the coherent structure is getting lost and they cannot be tracked. For large times the mean circulation is now underestimated. This may even result in the unphysical consequence of two circulation values at the same vortex time, see Fig. 4.12 (right, up). For large times the different averaging processes should be viewed as envelopes enclosing a realistic mean circulation.

Overall the vortex circulation observed in LES is much higher than the measured circulation. The decay slope is less steep, especially at high altitudes we have a phase of nearly constant vortex circulation. These effects are most likely unphysical and can be explained by the numerical setting. Subgrid turbulence of the RANS field is not mapped to the LES field, as in Misaka et al. (2013), which would lead to a vortex decay in the first phase. No ambient turbulence is considered in the LES which would accelerate the vortex decay and consequently decrease the slope, see Stephan et al. (2013a).

Beside these obvious shortcomings coincidences may be observed. First note that mean circulation decay curve is getting steeper with lower initial altitudes in the experiments, which might indicate end effects appearing at the touchdown but could also originate in the low generation altitude and the related accelerated interaction with ground effect secondary vortices, see Geisler & Konrath (2012). However, comparing Fig. 3.28 with Fig. 3.30 it is clear, that the circulation decay shortly after touchdown coincides with the end effects not with the ground interaction. Note that in the percentiles of Fig. 4.15 we see a distinct kink at a time of $t^* = 1$ in both ways of averaging. This kink is also visible in the LES data and clearly corresponds to the end effect. In Fig. 4.12-4.14 we also can detect this kink in the percentiles as well as in the LES curves, in Fig. 4.14 even visible in the mean curves. It is shifted between the figures corresponding to the propagation speed of the end effects. Case studies are mandatory to confirm that the kink in the percentiles originates in a kink in single decay curves, which would confirm a dedicated circulation reduction caused by end effects in reality.

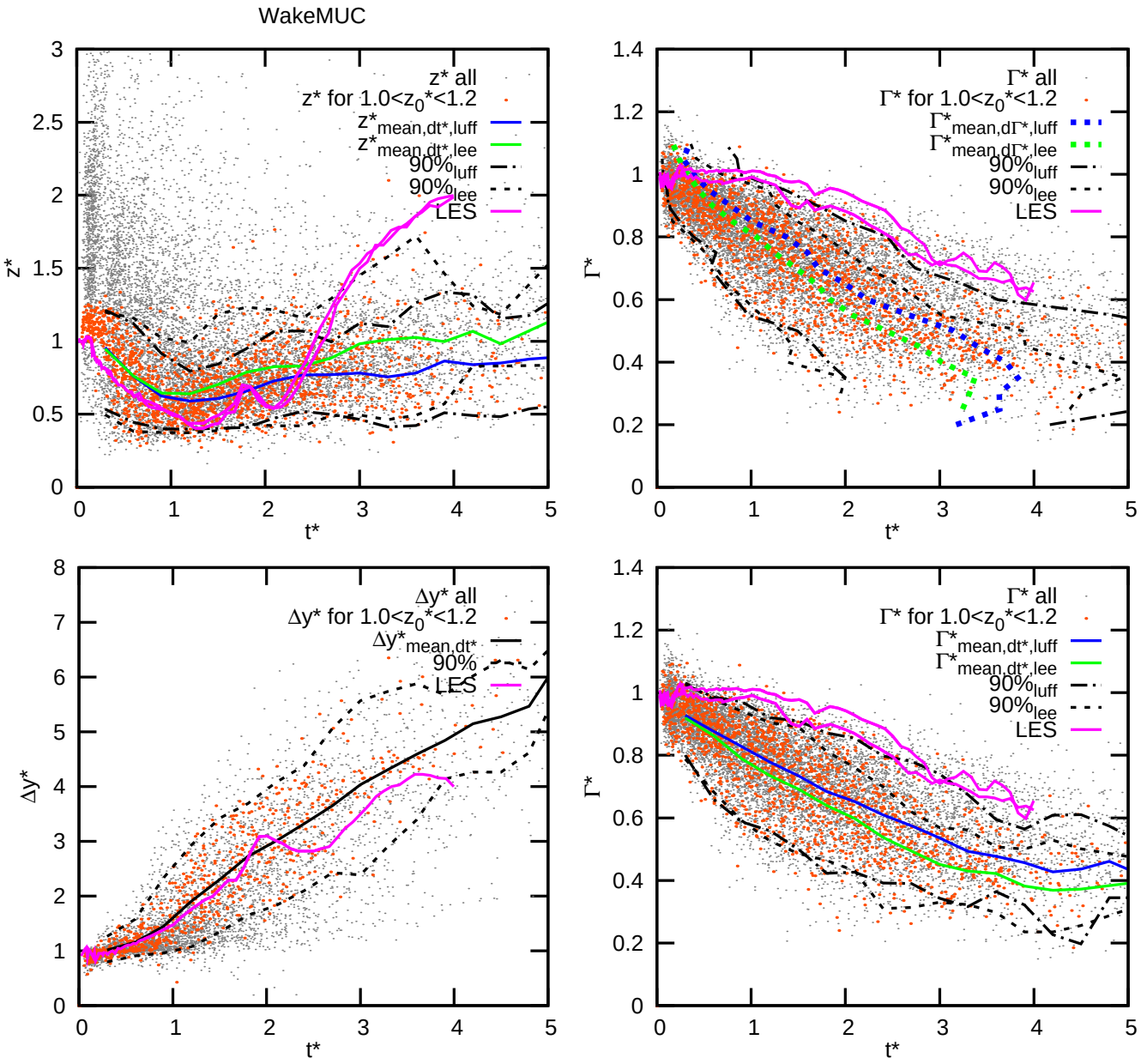

Abbildung 4.12.: Normalized altitude, wake-vortex separation and circulation averaged in temporal as well as circulation intervals, measurements, mean values, and percentiles for flight altitudes $1.0 < z_0^* < 1.2$ (red dots) and LES data with $z_0^* = 1.1$. Grey dots represent measurement data of all landings.

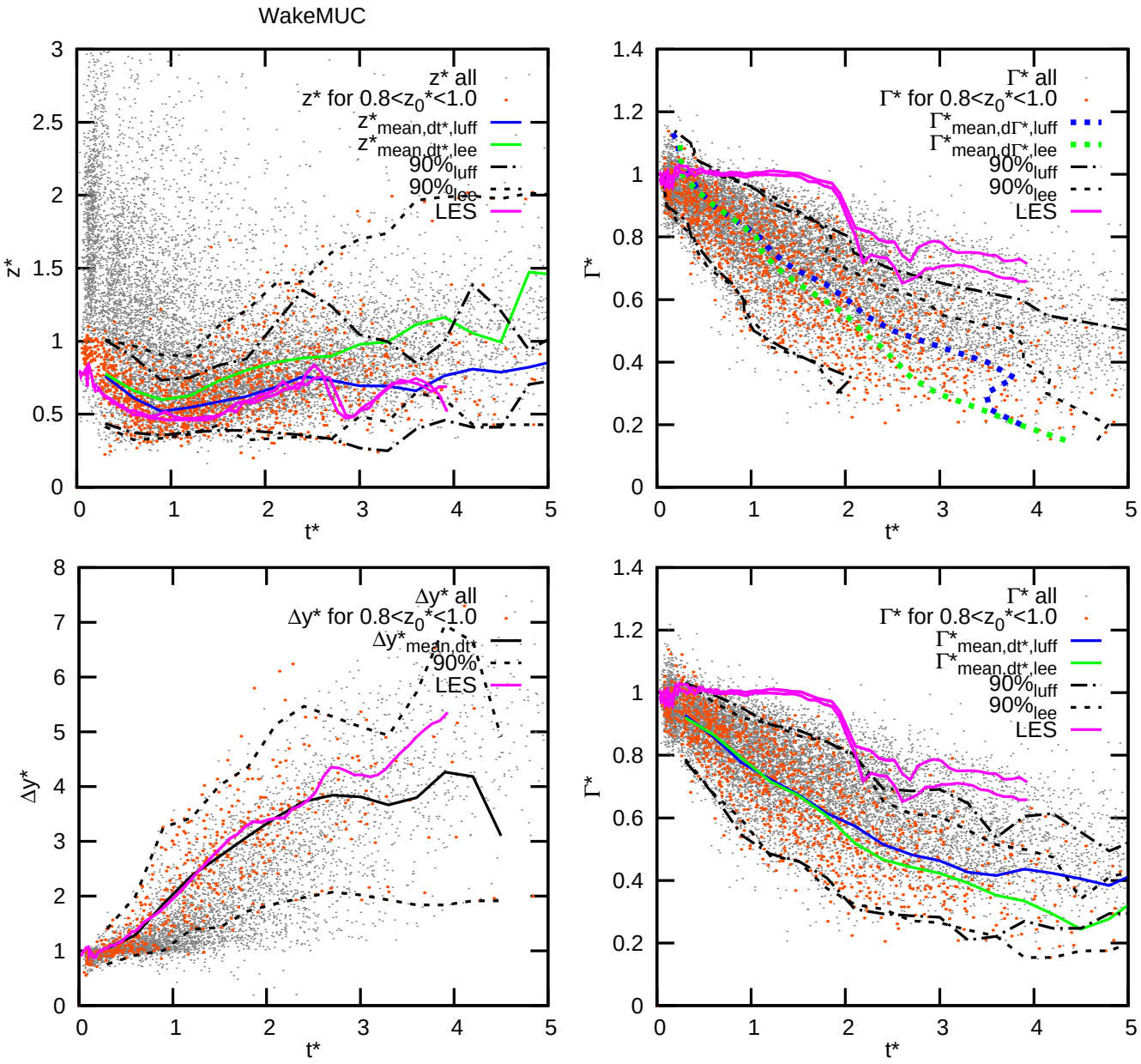

Abbildung 4.13.: Normalized altitude, wake-vortex separation and circulation averaged in temporal as well as circulation intervals, measurements, mean values, and percentiles for flight altitudes $0.8 < z_0^* < 1.0$ (red dots) and LES data with $z_0^* = 0.9$. Grey dots represent measurement data of all landings.

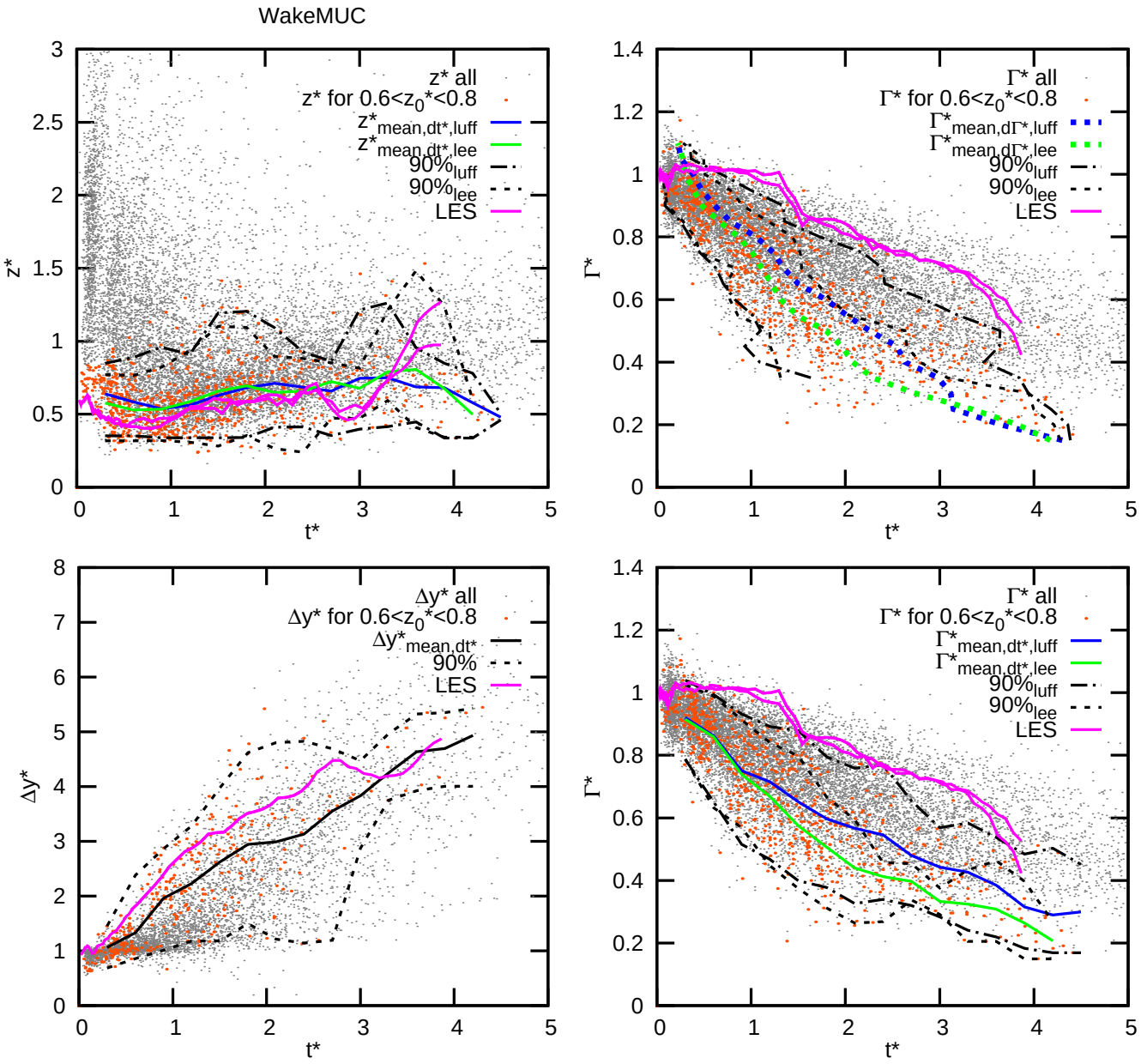

Abbildung 4.14.: Normalized altitude, wake-vortex separation and circulation averaged in temporal as well as circulation intervals, measurements, mean values, and percentiles for flight altitudes $0.6 < z_0^* < 0.8$ (red dots) and LES data with $z_0^* = 0.7$. Grey dots represent measurement data of all landings.

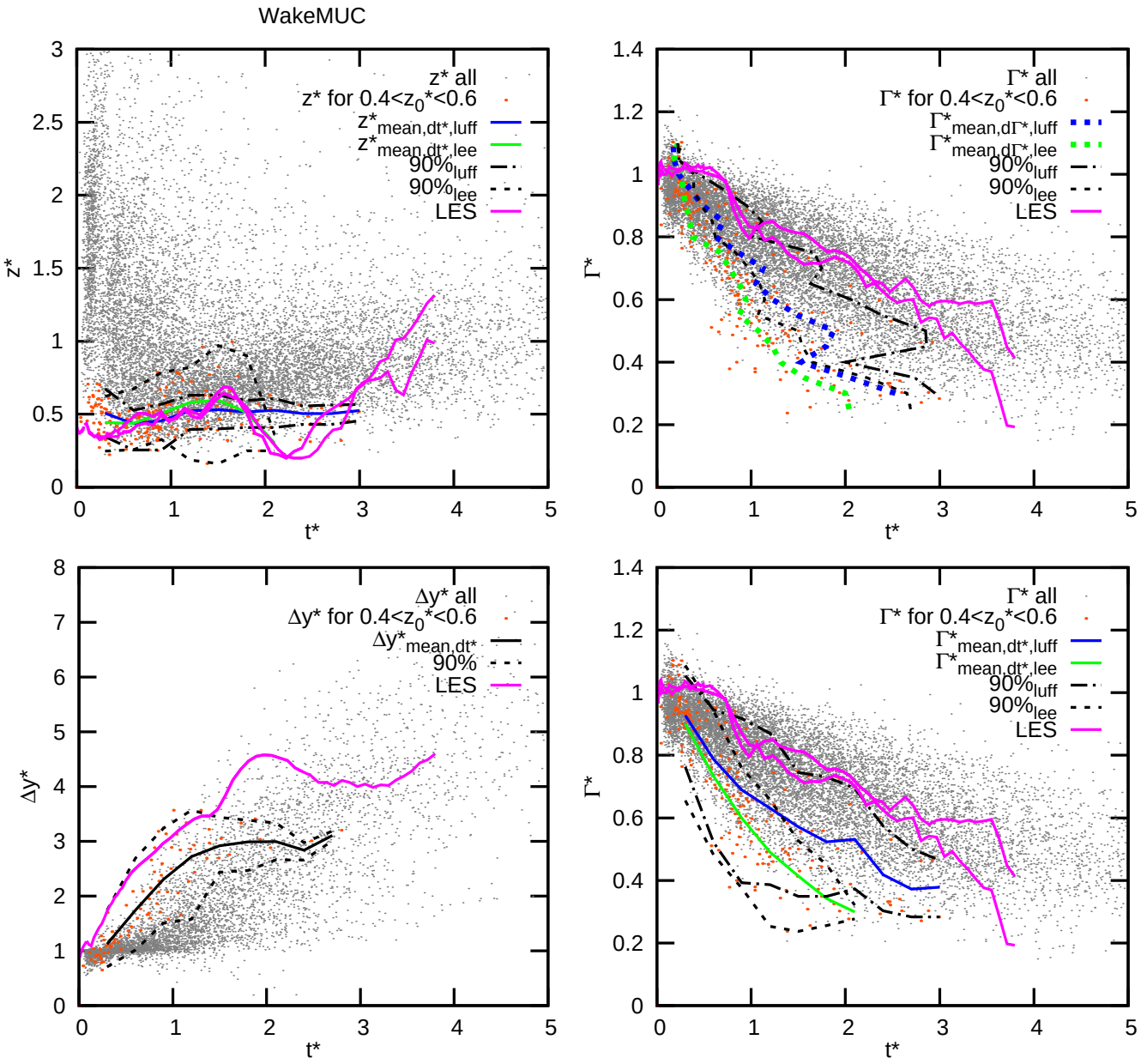

Abbildung 4.15.: Normalized altitude, wake-vortex separation and circulation averaged in temporal as well as circulation intervals, measurements, mean values, and percentiles for flight altitudes $0.4 < z_0^* < 0.6$ (red dots) and LES data with $z_0^* = 0.5$. Grey dots represent measurement data of all landings.

4.3. General Remarks

Since the landing process was approximated by one stationary RANS field, the flare as well the instant of touch down is not simulated very accurately. As a consequence we expect that end-effects are initiated later in LES than in reality. Furthermore the investigated angle of approach of 3.56 degree is to high compared to 3 degree as a standard in aviation. As a consequence the effect of the plate line should be even more pronounced at an airport. The effect of a turbulent wind during the landing will also be investigated in future. The absence of turbulence leads to unphysical decay slopes. Hence, the simulation results have to be interpreted carefully.

5. Conclusions and Outlook

Three main questions lead the way through the thesis:

1. How can the flow field, generated by a landing aircraft, be simulated accurately?
2. Can the wake-vortex decay in ground proximity be artificially enhanced?
3. Can the numerical findings be confirmed by measurement data?

To handle these topics the physics of aircraft landing with a particular focus on the aircraft wake is studied. The investigations require a couple of methods and concepts which are introduced and developed. The physics of vortex generation is presented as well as the wing in ground effect. It is pointed out that stationary considerations of the wing in ground effect can not fully explain the effects of an unsteady landing, where parameters of interest change in a complex way. Aircraft flight test data is used to explain unsteady landing effects. The synopsis of different sources suggests a slight increase of wake vortex strength with the approach to the ground surface. Four phases of the landing process are differentiated and respective vortex phases are postulated. Concepts of turbulence theory, required in the thesis, are introduced. As the main instrument to investigate wake-vortex evolution during landing the large-eddy simulation code MGLET is presented including selected details of the relevant algorithms. The investigation of the phenomena appearing during final approach require completely new methodologies. For this purpose the concept of the so-called spatial LES as a tool to spatially and temporally initialize the aircraft wake is adopted. Spatial LES was developed further to enable more complex aircraft flight paths, e.g. aircraft descent. Concepts for turbulence initialization as well as for the introduction of complex ground obstacles are developed. A wall model is introduced enabling high Reynolds number boundary layer flows. The computational setting as well as the developed post processing tools are detailed.

To address the first question a complete landing of a long range aircraft in high lift configuration with flaps and slats deployed including approach, touchdown, and the respective evolution of the wake is simulated combining a Reynolds-averaged Navier-Stokes flow field and a large-eddy simulation. The steady RANS flow field is used as a forcing term in the ground fixed LES domain. The complex flow field of the landing aircraft, particularly the multiple vortices constituting the wake in the near-field, are visualized and analyzed. The wing in ground effect evolving during flare is investigated and touchdown effects are characterized. The vortex advection in ground proximity is quantified. End effects occurring at touchdown lead to circulation decay combined with a core radius growth close to the area of touchdown. The ground effect leads to separation of secondary vortex structures at

the ground wrapping around the primary vortices. Simulations further reveal the complex developments of vortex topology after touchdown with multiple ground linkings reducing the rolling moment potentially acting on following aircraft. These three effects elucidate that landing is indeed safer than anticipated by established wake vortex advisory systems. These insights provide a basis to optimize WVAS with respect to safety and capacity of airports.

In order to address the second question we conduct wall-resolved temporal LES computations to study wake vortex behavior in ground effect with and without crosswind as well as with and without obstacles at the ground. The investigation of the decay mechanisms at $\mathrm{Re}_\Gamma = 23\ 130$ reveals that perturbations of the secondary vortices trigger rapid vortex decay of the primary vortices. It is shown that simple wall modeling does not bring forth the coherent structures in the boundary layer flow that are critical for rapid vortex decay in ground effect. We expect that at realistic Reynolds numbers surface irregularities and meteorological conditions will affect the boundary layer flow and perturb the secondary vortices similarly. In order to further accelerate vortex decay in ground proximity we impose differently shaped obstacles and analyze and quantify the respective accelerated wake vortex decay. At flight altitudes of one initial vortex separation above ground the decay process is initiated nearly one characteristic vortex time t_0 earlier, whereas circulation levels relevant for aircraft separation are reached already two t_0 earlier. This rapid wake vortex decay in ground proximity is achieved by the dedicated use of properties of vortex dynamics with the following characteristics:

- Early detachment of strong omega-shaped secondary vortices
- Omega shaped secondary vortices approach the primary vortices by self-induction
- After the secondary vortices have looped around the primary vortices they separates and propagate along the primary vortices again driven by self induction
- The dedicated secondary vortices remain connected to the regular ground effect vortices and thus obtain continued supply of energy
- The highly intense interaction of primary and secondary vortices leads to rapid wake vortex decay independent from natural external disturbances

These disturbances propagating along the wake vortices can also be considered as a variation of so-called end effects where we identify two different types. One type corresponding to a pressure disturbance propagating inside the vortex core and one corresponding to propagating helical vortex structures that develop from the rolled-up secondary vortices. The obstacles are optimized with respect to size and shape. We show that a plate line triggers even slightly stronger secondary vortices and higher decay rates than a much more massive block-shaped barrier. Headwind does not degrade the averaged circulation decay triggered by the plate line. Most of the numerical investigations of the obstacle effect are performed with wall-resolved temporal LES at a relatively small Reynolds number. In addition the effect of a plate line established in front of the runway is demonstrated with spatial LES

at moderate Reynolds numbers and a wall model. There we observed a rapid circulation reduction caused by the plate line and the interference with the end effects spreading from the touchdown zone. We argue that the presented effects of the obstacles, in particular the strong secondary vortex structures that trigger an early vortex decay, are relatively independent from the Reynolds number. In summary the introduction of plate lines at the ground supports the selective generation of secondary vortices and enables a smart utilization of vortex properties in order to generate fast approaching secondary vortex structures and rapidly spreading disturbances leading to early vortex decay in ground proximity.

Addressing the third question we verify the effectiveness of obstacles for the acceleration of vortex decay with results from water towing tank experiments. In the water towing tank "Wasser Schleppkanal Göttingen" a generic aircraft wing model was towed over flat ground as well as a block shaped obstacles with a squared cross section. A vortex core visualization using black ink was employed in order to get both a first qualitative overview as well as a global quantitative characterization. Velocity vector fields have been recorded by stereo PIV for quantitative analysis. A vortex tracking evaluation was performed allowing the determination of the vortex core trajectories in selected cross planes as well as vortex parameters like circulation strength and core radius. In order to create comparability with the experiments a passive tracer distributed in the vortex core is used in LES. In the case of a flat ground we model the turbulent strut wake as the most important source of turbulence. Both, experiment and LES show that the well known wake vortex flow in ground proximity is significantly disturbed by the obstacles. The disturbance first appears above the obstacle and then propagates axially along the wake vortices visualized by an accumulation of the tracer. This end effect phenomenon arises from propagating helical vortex structures that develop from the rolled-up secondary vortices at the obstacle. The propagation speed of the disturbance in the experiment as well as in the simulations is evaluated. We suggest a propagation speed formula for the helical disturbances based on a thin vortex ring. The scalability of this simple model appears reasonable. Colliding disturbances generated by two obstacles lead to vortex bursting and additionally support the decay process.

The peculiarities of wake vortex decay characteristics are compared in the case of a flat ground as well as an obstacle at the ground. Quantitative comparisons comprise vortex decay, rebound altitude, vortex core radius development and propagation speed of the helical disturbances generated by the obstacles. The quantitative analysis of the flow field measured with time-resolved PIV reveals that the circulation is reduced significantly by obstacles in qualitative agreement with LES. The decay process at different distances to the obstacle agrees qualitatively between experiment and LES. Also the vortex core trajectories depending on the distance to the obstacle agree qualitatively. The experiments support the results of the simulations and indicate that flight safety could be improved and/or ICAO separations of aircraft might be optimized if the presented method for the enhancement of wake vortex decay would be applied at an airport at runway tails. Therefore an appropriate wake vortex advisory system should be installed including the obstacle effect to predict wake vortex behavior along the glide path. We hope that this will lead to a reduced number of wake encounters and increase the efficiency of wake vortex advisory systems.

The measurement campaign WakeMUC at Munich airport serves as an assessment for the developed concepts with spatial LES simulating the complete landing phase. A good agreement of wake vortex trajectories as well as vortex separation was observed. In particular, quite irregular and strong vortex rebound in a measurement plane can be explained by complex three-dimensional vortex deformations in connection with ground linking. Enhanced measured circulation decay can be explained by end effects propagating into the measurement plane as revealed by the simulations. The comparisons reveal that dedicated sources of turbulence, like ambient wind and subgrid scale turbulence of the flow around the aircraft have to be considered in the simulations to achieve realistic circulation decay curves.

At the beginning of the dissertation a patent entitled "Surface Structure on a Ground Surface for Accelerating Decay of Wake Turbulence in the Short Final of an Approach to a Runway" has been filed by Frank Holzäpfel under number DE 10 2011 010 147. In the meanwhile flight experiments have been conducted at Oberpfaffenhofen airport (Germany) employing the plate line design elaborated in the thesis. The flight tests confirm that plate lines with the proposed dimensions actually accelerate wake vortex decay in ground proximity. However, statistically the effect is less pronounced than anticipated by results of the thesis which might be explained by too few plates such that several times the wake vortices missed the plates. The experiments have been reported by a number of national and international newspapers like Süddeutsche Zeitung and Neue Züricher Zeitung to name but a few. A three-year DLR project is planned to start at 2014 entitled "Land-Based and Air-Borne Wake Systems (Wirbelschleppe)". The following outreaching work is planned within that project. Since the landing process so far was approximated by one stationary RANS field, the instant of touchdown is not simulated very accurately. As a consequence we expect that end-effects are initiated later than it is expected in reality. In the project it is planed to establish and employ in the LES unsteady RANS simulations of the touchdown. Detailed insights into wing in ground effect during flare and the formation of end effects are expected. Aiming at a highly realistic simulation of the landing, a coupling of the LES field to an aircraft dynamic RANS model is required, a so-called two way coupling. However, this would require intense collaboration with RANS specialists. It is planned to further optimize the design of the plate lines with LES and to verify the accelerated wake-vortex decay by an installation at Munich airport. At the Institute of Aerodynamic and Flow Technology (DLR) a risk assessment of induced rolling moment of wake vortices disturbed by a plate line is planned. In addition, the wall model will be changed to a surface roughness model that reflects the situation at real airports more sensible. As another application of spatial LES the integration of the engine jet into the RANS/LES coupling is planned in order to study the entrainment of the jet into the wake flow and the impact of the exhaust properties on the formation and evolution of contrails. State-of-the-art WVAS are quasi-two-dimensional and cover the described strongly three-dimensional vortex deformations only in a probabilistic sense. To include them into the deterministic part would require so-called vortex filament methods that are not mature in the setup of landing aircraft. Further the end effects generated by plates and touchdown could be parametrized more sophisticatedly with vortex filament methods and integrated into the WVAS.

A. Appendix: Aircraft Geometry

The aircraft model used in the spatial LES is the AIRBUS A340-300 catapult model of ONERA with a scale 1:27, a wingspan of $b = 2.236\,\mathrm{m}$ and an aerodynamic mean chord of $c = 0.269\,\mathrm{m}$. The Geometry of the AIRBUS A340-300 is depicted in Fig. A.1 and Fig. A.2, (Airbus, 2012).

Table A.1 lists aircraft parameters and vortex parameters of the A340-300 and A340-600 which serve as example aircraft for this thesis. In addition the model parameters of the ONERA A340-300 catapult model are listed, which are employed in the spatial LES, as well as the vortex parameters employed in the temporal LES.

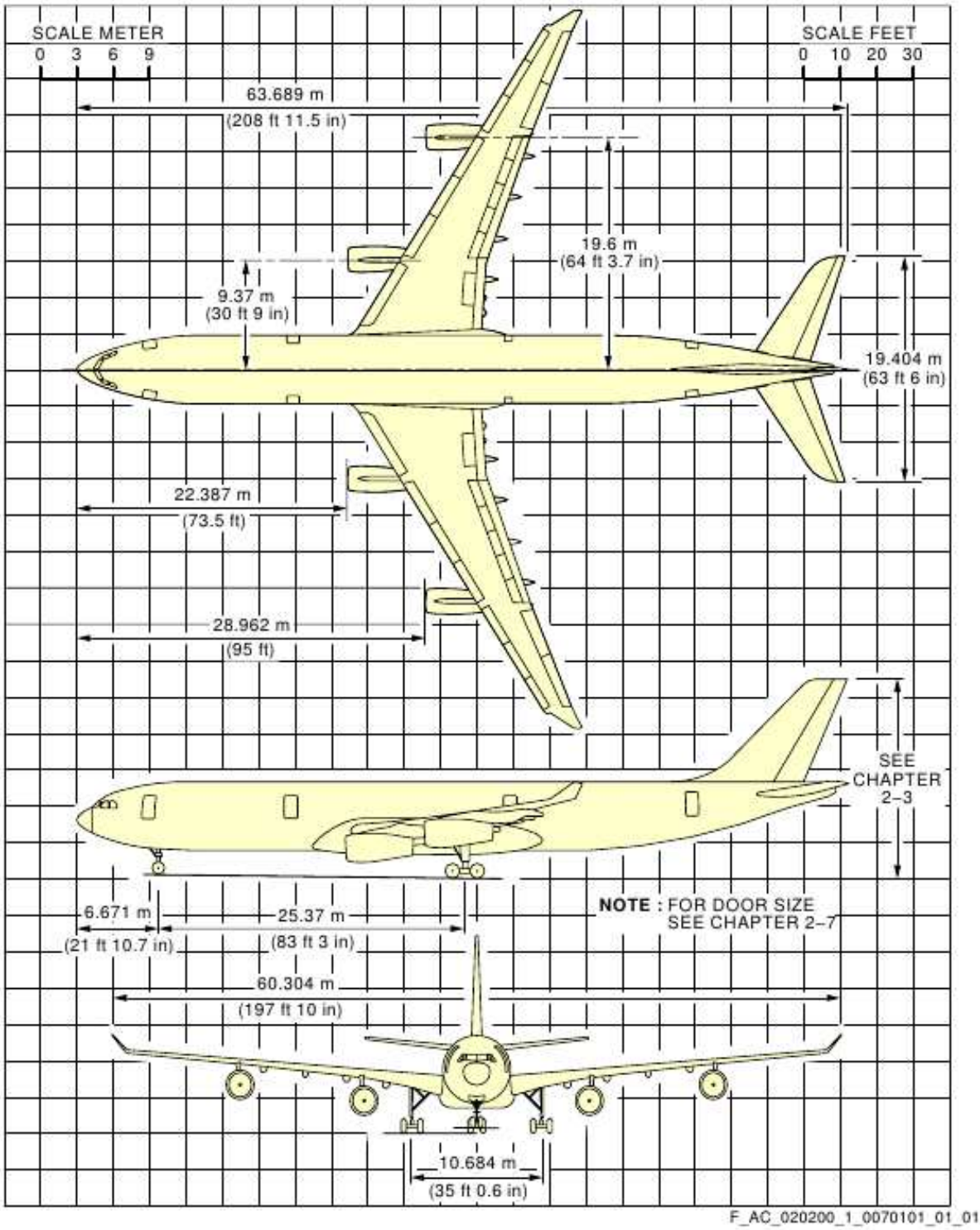

(a)

Abbildung A.1.: General airplane dimensions of an A340-300 (Airbus, 2012)

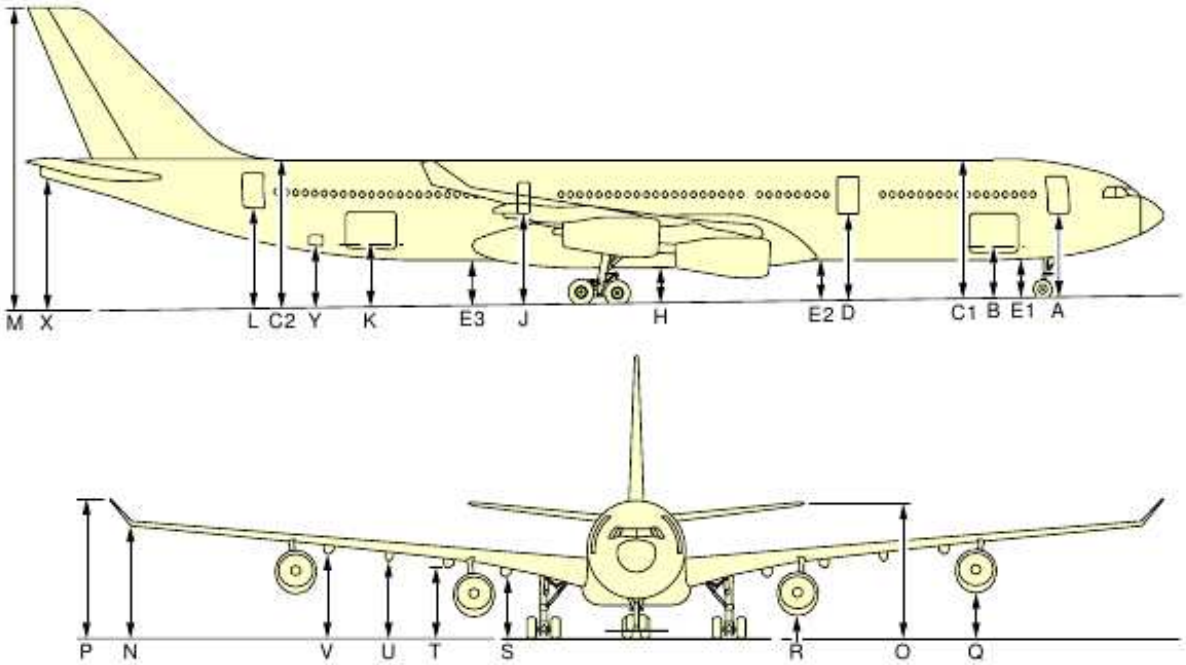

MRW 254 900 kg 561 949 lb		OPERATING WEIGHT EMPTY CG 31.9%		MAXIMUM RAMP WEIGHT CG 20.7%		MAXIMUM RAMP WEIGHT CG 38.2%		AIRCRAFT ON JACKS	
		m	ft	m	ft	m	ft	m	ft
	A	4.59	15.05	4.45	14.59	4.52	14.8	6.32	20.7
	B	2.73	8.95	2.54	8.33	2.58	8.62	4.14	13.5
FR 26	C1	7.76	25.45	7.58	24.86	7.60	25.09	9.32	30.5
FR 72	C2	8.42	27.62	8.25	27.06	8.20	26.73	9.32	30.5
	D	4.84	15.87	4.65	15.25	4.67	15.41	6.32	20.7
FR 20	E1	2.13	6.98	1.94	6.36	1.96	6.59	3.68	12
FR 37	E2	2.27	7.44	2.09	6.85	2.10	6.95	3.68	12
FR 56	E3	2.37	7.77	2.49	8.17	2.46	7.97	3.68	12
FR 45	H	2.02	6.62	1.84	6.03	1.83	6	3.26	10.7
	J	5.31	17.42	5.12	16.80	5.10	16.73	6.32	20.7
	K	3.44	11.28	3.26	10.69	3.23	10.49	4.24	13.9
	L	5.70	18.69	5.52	18.10	5.47	17.74	6.53	21.4
	M	16.99	55.72	16.82	55.17	16.73	54.61	17.62	57.80
	N	6.35	20.83	6.01	19.71	5.98	19.55	7.55	24.7
	O	8.14	26.70	7.96	26.11	7.88	25.58	9.23	30.2
	P	7.91	25.94	7.57	24.83	7.53	24.60	8.96	29.4
	Q	2.59	8.49	2.35	7.71	2.34	7.67	3.98	13
	R	1.42	4.65	1.23	4.03	1.24	4.10	2.79	9.1
	S	3.85	12.63	3.67	12.04	3.65	11.94	5.25	17.2
	T	4.31	14.14	4.12	13.51	4.10	13.45	5.70	18.7
	U	4.59	15.05	4.38	14.37	4.36	14.23	6	19.6
	V	4.90	16.07	4.66	15.28	4.64	15.15	6.30	20.6
	X	7.30	23.94	7.12	23.35	7.05	22.83	8.10	26.5
	Y	3.58	11.74	3.39	11.12	3.35	10.86	4.39	14.4

NOTE: PASSENGER AND CARGO DOOR CLEARANCES ARE MEASURED FROM THE CENTER OF THE DOOR SILL AND FROM FLOOR LEVEL.

F_AC_020300_1_0050101_01_01

(a)

Abbildung A.2.: Ground clearance of various points of the aircraft for an A340-300 (Airbus, 2012)

Tabelle A.1.: Configurations and vortex parameters of large aircraft, Breitsamter (2007)

			A340-300	A340-600	tLES	sLES
high lift configuration ($\rho = 1.2\,\mathrm{kg}\,/\,\mathrm{m}^3$)						
mass (landing)	m	[kg]	190000	254000		30.51
mass (take off)	m_{TO}	[kg]	271000	365000		30.51
wing span	b	[m]	60.3	63.7		2.236
wing planform area	A	[m^2]	361.6	437.0		0.53
aspect ratio	Λ	[−]	10.1	9.3		9.3
flight speed	U	[m / s]	75	78		25
Reynolds number	Re_c	[−]	32×10^6	33×10^6		5.2×10^5
lift coefficient	C_L	[−]	1.527	1.562		1.4
vortex parameters						
circulation	Γ_0	[$\mathrm{m}^2\,/s$]	435	531	530	5.36
descent speed	w_0	[m / s]	1.46	1.69	1.79	0.49
time unit	t_0	[s]	32.38	29.60	26.3	3.6

B. Appendix: Rough Surfaces

An approach to model the wall shear stress in Sec. 2.4.2 which reflects the atmospheric boundary layer of an airport more realistically is to consider a rough surface. For rough surfaces with a neutral atmospheric stability the velocity in the logarithmic layer can be written as

$$u_{tan}(z) \quad = \quad \frac{u_\tau}{\kappa} \log\left(\frac{z}{z_0}\right), \tag{B.1}$$

where z_0 is a characteristic roughness length, Monin & Obukhov (1954). From Eq. (B.1) and the tangential velocity at the first grid point the tangential wall shear stress can be deduced algebraically independently of the Reynolds number. This model approach is pursued by Schmidt & Schumann (1989) and additionally refined by Hultmark et al. (2013).

However, the roughness length z_0 depends on the averaged height of the roughness elements k_s and the Reynolds number of the flow (Schlichting & Gersten, 1997). In the case that the viscous boundary layer is small compared to k_s, i.e. $k_s^+ \geq 70$, the influence of viscosity effects can be asymptotically neglected yielding a relationship

$$z_0 = k_s \exp(-8.0\kappa) = 0.04 k_s. \tag{B.2}$$

Typical values for airports are in the order of $z_0 \approx 0.01 - 0.03\,\mathrm{m}$.[1] In this thesis simulations are performed with a scaled computational domain and Reynolds number. Modeling the wall shear stress in a scaled simulation we observe from Eq. (B.2) that k_s as well as z_0 has to be scaled according to a characteristic length scale. However in case of a Reynolds number scaling it has to be ensured that $k_s^+ \geq 70$.

[1] http://de.wikipedia.org/wiki/Logarithmisches_Windprofil

Nomenclature

Symbols

α, β ..... parameters of wall switching function

δ ..... Dirac delta function

δ ..... half channel height

η ..... Kolmogorov length scale, m

Γ ..... vortex circulation, $\mathrm{m}^2\,/\,\mathrm{s}$

γ ..... angle of approach

Γ_0 ..... initial vortex circulation, root circulation, $\mathrm{m}^2\,/\,\mathrm{s}$

Γ_{5-15} ..... circulation averaged in a disc segment of 5 m to 15 m, $\mathrm{m}^2\,/\,\mathrm{s}$

Γ_5 ..... circulation a circle of 5 m, $\mathrm{m}^2\,/\,\mathrm{s}$

Γ_{hel} ..... circulation of vortex helix, $\mathrm{m}^2\,/\,\mathrm{s}$

Γ_{ring} ..... circulation of vortex ring, $\mathrm{m}^2\,/\,\mathrm{s}$

κ ..... von Karman constant

Λ ..... aspect ratio b^2/A

λ ..... streak spacing, m

ν_t ..... turbulent viscosity in the strut wake, m^2/s

ν_{mol}, ν ..... molecular viscosity, $\mathrm{m}^2\,/\,\mathrm{s}$

ν_{turb} ..... turbulent viscosity, $\mathrm{m}^2\,/\,\mathrm{s}$

ω_x ..... axial vorticity, $1/\,\mathrm{s}$

Re_τ ..... channel flow Reynolds number

Re_c ..... Reynolds number based on chord length

Re_Γ ..... vortex Reynolds number

ρ ..... fluid density, $\mathrm{kg}\,/\,\mathrm{m}^3$

σ ..... standard deviation

τ ..... shear stress, $\mathrm{N}\,/\,\mathrm{m}^2$

τ_w ..... wall shear stress, $\mathrm{N}\,/\,\mathrm{m}^2$

ε ..... eddy dissipation rate, $1/\,\mathrm{s}$

$\vec{\omega}$ ..... vorticity vector, $1/\,\mathrm{s}$

$\vec{r}$ ..... difference vector $\vec{y} - \vec{x}$, m

$\vec{s}$ ..... normalized tangent vector

$\vec{u}$ ..... velocity vector, $\mathrm{m}\,/\,\mathrm{s}$

$\vec{x}$ ..... position vector, m

A ..... area, wing plan-form area, m^2

a_{hel} ..... core radius of vortex helix, m

a_{ring} ..... core radius of vortex ring, m

B ..... constant

b ..... bi-normal coordinate

b ..... wingspan, m

b_0 ..... separation of circulation centroids, initial vortex separation, m

C ..... chord length, m

C_D ..... induced drag coefficient

C_L ..... total lift coefficient

c_s ..... Smagorinsky constant

D ..... diffusivity, $\mathrm{m}^2\,/\,\mathrm{s}$

D ..... induced drag, N

$d\vec{A}$ ..... vectorial surface element

E ..... kinetic energy, $\mathrm{N\,m}$

E_Γ ..... kinetic energy of the vortex pair, N m

g ..... gravitational acceleration, m / s^2

H ..... aircraft altitude during landing, m

h ..... wing altitude, m

H_0 ..... virtual landing position below ground for *Cat.III* landings , m

H_A ..... aircraft altitude at the beginning of flare, m

k ..... wave number

L ..... lift force, N

L_x, L_y, L_z ..... dimensions of computational domain, m

l_{strut} ..... strut length, m

M ..... aircraft mass, kg

n ..... normal coordinate

N_x, N_y, N_z ..... number of grid points

p ..... pressure, N / m^2

p' ..... deviation from reference pressure p_0, N / m^2

p_0 ..... reference pressure, N / m^2

q ..... arbitrary quantity, passive tracer

r_c ..... vortex core radius, m

R_{hel} ..... ring radius of vortex helix, m

R_{ring} ..... ring radius of vortex ring, m

s ..... wing load factor

$S_{i,j}$ ..... strain rate tensor, 1/ s

T ..... inverse deceleration rate during flare, s

t, t_0, T ..... time, fixed time, time period s

t_0 ..... vortex reference time, s

U ..... aircraft flight speed, model towing speed, m/s

u, v, w ..... velocity components, m / s

u_1, u_2, u_3 ..... velocity components, m / s

U_{hel} ..... propagation speed of vortex helix, m / s

U_{prop} ..... propagation speed of end effects, m / s

U_{ring} ..... propagation speed of vortex ring, m / s

V_x, V_r, V_θ ..... axial, radial, and azimuthal velocities in cylindrical coordinates

w_0 ..... initial vortex descent speed, m / s

x, r, θ ..... axial, radial, and azimuthal cylindrical coordinate

x, y, z ..... coordinates, m

x_1, x_2, x_3 ..... coordinates, m

subscript

0 ..... initial or reference state

max ..... maximum value

min ..... minimum value

rms ..... root mean square of velocity fluctuations, m/s

c ..... centroid coordinate

c ..... coarse

f ..... fine

i, j ..... indices for spatial directions

L ..... large-eddy simulation

W ..... Wasser Schleppkanal Göttingen

w ..... at the wall, first grid point

superscript

$'$ ..... deviation from a reference state

$'$ ..... normalized by chord length

$'$ ..... surface averaged

$*$ ..... normalized by vortex flow parameters

$+$ ..... normalized by intrinsic channel flow parameters

Abbreviations

ATC ..... air traffic control

ATRA ..... Advanced Technology Research Aircraft

AWIATOR .... Aircraft Wing with Advanced Technology Operation (EU project)

C-Wake ..... Wake vortex characterization and control (EU project)

D2P ..... deterministic two-phase wake vortex decay and transport model

DLR ..... German Aerospace Center

DNS ..... direct numerical simulation

EULAG ..... Eulerian and semi-Lagrangian flow solver

FAA ..... American Federal Aviation Administration

FAR-Wake .... Fundamental Research on Aircraft Wake Phenomena (EU project)

HALO ..... high altitude and long range research aircraft

ICAO ..... International Civil Aviation Organization

LES ..... large-eddy simulations

LIDAR ..... Light Detection And Ranging

MGLET ..... Multi-Grid Large Eddy Turbulence

MRS ..... minimum radar separation

NATS ..... British National Air Traffic Secvices

NM ..... nautical miles

ONERA ..... Office National d'Etudes et de Recherche Aérospatiales

P2P ..... probabilistic two-phase wake vortex decay and transport model

PIV ..... Particle Image Velocimetry

RANS ..... Reynolds-averaged Navier-Stokes

REA ..... Royal Aircraft Establishment

RECAT ..... Eurocontrol recategorization program

SVS ..... secondary vortex structures

TKE ..... turbulent kinetic energy

WakeFRA ..... field measurement campaign at Frankfurt airport

WakeMUC .... field measurement campaign at Munich airport

WakeOP ..... field measurement campaign at Oberpfaffenhofen airport

WIG ..... wing-in-ground effect

WSG ..... Wasser Schleppkanal Göttingen

WVAS ..... wake-vortex advisory system

Abbildungsverzeichnis

Tabellenverzeichnis

Literaturverzeichnis

Adrian, R. J., Meinhart, C., Tomkins, C. (2000), Vortex organization in the outer region of the turbulent boundary layer. *Journal of Fluid Mechanics*, vol. 422, pp. 1–54.

Airbus, S. A. S. (2012), A340-200/-300 Airplane Characteristics for Airport Planning. Airbus S.A.S., Customer Service, Technical Data Support and Services, 31707 Blagnac Cedex, France.

Bao, F., Vollmers, H. (2005), Alleviation of End-effects in Facilities for Far Wake Investigations. *AIAA-Paper 2005-0907, 43rd AIAA Aerospace Sciences Meeting and Exhibit.* Reno, Nevada.

Baumert, H. Z. (2012), Universal equations and constants of turbulent motion. *http://arxiv.org/abs/1007.3837v2.*

Béchara, W., Bailly, C., Lafon, P. (1994), Stochastic Approach to Noise Modeling for free Turbulent Flows. *AIAA Journal*, vol. 32, No. 3, pp. 455–463.

Brandt, A., Dendy, J. E., Ruppel, H. (1980), The Multigrid Method for Semi-Implicit Hydrodynamics Codes. *Journal of Computational Physics*, vol. 34, pp. 348–370.

Breitsamter, C. (2007), *Nachlaufwirbelsysteme großer Transportflugzeuge.* Herbert Utz Verlag, ISBN: 978-3-8316-0713-6.

Breitsamter, C. (2011), Wake vortex characteristics of transport aircraft. *Progress in Aerospace Sciences*, vol. 47, pp. 89–134.

Butler, K. M., Farrell, B. F. (1993), Optimal perturbations and streak spacing in turbulent shear flow. *Physics of Fluids*, vol. 5, pp. 774–777.

Campbell, S., Dasey, T., Freehart, R., Heinrichs, R., Matthews, M., Perras, G., Rowe, G. (1997), Wake Vortex Field Measurement Program at Memphis, TN Data Guide, Project Report NASA/L-2. Techn. Ber., Lincoln Laboratory, Massachusetts Institute of Technology.

Cantwell, B., Coles, D., Dimotakis, P. (1978), Structure and entrainment in the place of symmetry of a turbulent spot. *Journal of Fluid Mechanics*, vol. 87, pp. 641–672.

Chapman, D. R. (1979), Computational Aerodynamics Development and Outlook. *AIAA Journal*, vol. 17, No.12, pp. 1293–1313.

Chong, M. S., Perry, A. E., Cantwell, B. J. (1990), A general classification of three-dimensional flow fields. *Physics of Fluids*, vol. 5, pp. 050765.

Constant, G. D. J., Foord, R., Forrester, P. A., Vaughan, J. M. (1994), Coherent laser radar and the problem of aircraft wake vortices. *Journal of Modern Optics*, vol. 41, pp. 2153–2173.

Coton, P. (1998), Study of Environment Effects by Means of Scale Model Flight Test in a Laboratory. *21st ICAS Congress*, ICAS-98-391. Melbourne.

Cottin, C., Desenfans, O., G., D., Winckelmans, G. (2007), Towing-tank visualization of two-vortex systems in ground effect. Techn. Ber., FAR-Wake, Université Catholique de Louvain (UCL).

Coustols, E., Stumpf, E., Jaquin, L., Moens, H., F.and Vollmers, Gerz, T. (2003), Minimized Wake: A Collaborative Research Programme on Aircraft Wake Vortices. *AIAA Paper 2003-0938*.

Critchley, J., Foot, P. (1991), UK CAA Wake Vortex Database: Analysis of Incidents Reported Between 1982 and 1990. *Civil Aviation Authority, CAA Paper 91*.

Crouch, J., Miller, G., Spalart, P. (2001), Active-Control System for Breakup of Airplane Trailing Vortices. *AIAA Journal*, vol. 39, No 12, pp. 2374–2381.

Crow, S. C. (1970), Stability Theory for a Pair of Trailing Vortices. *AIAA Journal*, vol. 8, No. 12, pp. 2172–2179.

Daeninck, G., Desenfans, O., Winckelmans, G. (2006), FAR-Wake Technical Report 3.1.1-1, Span loading variations and wake roll-up in ground effect. Techn. Ber., Université catholique de Louvain (UCL).

de Bruin, A., Winckelmans, G. (2005), Cross-flow kinetic energy and core size growth of analytically defined wake vortex pairs. Techn. Ber., NLR-CR-2005-412, NLR.

De Gregorio, F., Ragni, A. (2003), Wake Vortex Characterisation in Towing Tank Facilities Using PIV Technique. *AIAA Paper 2003-93*.

De Visscher, I., Lonfils, T., Winckelmans, G. (2013), Fast-Time Modeling of Ground Effects on Wake Vortex Transport and Decay. *Journal of Aircraft*. Doi: 10.2514/1.C032035.

Deardorff, J. W. (1970), A numerical study of three-dimensional turbulent channel flow at large Reynolds numbers. *Journal of Fluid Mechanics*, vol. 41, pp. 453–480.

Delisi, D. P. (2006), Laboratory Measurements of the Effect of Ambient Turbulence on Trailing Vortex Evolution. *44th AIAA Aerospace Sciences Meeting and Exhibits, San Reno*.

Delisi, D. P., Pruis, M. J., Wang, F. Y., Lai, D. Y. (2013), Estimates of the Initial Vortex Separation Distance, b_0, of Commercial Aircraft from Pulsed Lidar Data. *51st AIAA Aerospace Science Meeting, Grapevine, Texas.*

Doligalski, T. L., Smith, C., A., W. J. D. (1994), Vortex interactions with walls. *Annual Review of Fluid Mechanics*, vol. 26, pp. 573–616.

Dufresne, L., Baumann, R., Gerz, T., Winckelmans, G., Moet, H., Capart (2005), Large Eddy Simulation of Wake Vortex Flows at Very High Reynolds Numbers: A Comparison of Different Methodologies. Techn. Ber., AWIATOR, D1.14-16.

Duponcheel, M., Lonfils, T., Bricteux, L., Winckelmans, G. (2006), Simulations of three-dimensional wake vortices in ground effect using a fourth-order incompressible code. *7th National Congress on Theoretical and Applied Mechanics, Mons.*

Etkin, B. (1972), *Dynamics of Atmospheric Flight.* John Wiley & Sons, New York.

Eurocontrol (2013), Challenges of growth. Techn. Ber., Summary Report.

Fabre, D., Jacquin, L., Loof, A. (2002), Optimal perturbations in a four-vortex aircraft wake in counter-rotating configuration. *Journal of Fluid Mechanics*, vol. 451, pp. 319–328.

Fischenberg, D. (1999), Ground Effect Modeling Using a Hybrid Approach of Inverse Simulation and System Identification. *AIAA Paper 99-4324.*

Fröhlich, J. (2006), *Large Eddy Simulation turbulenter Strömungen.* B.G. Teubner Verlag.

Fujii, K. (1995), Unified Zonal Method Based on the Fortified Solution Algorithm. *Journal of Computational Physics*, vol. 118, pp. 92–108.

Geisler, R., Konrath, R. (2012), Experimental Study on Wake Vortices Impacted by Turbulence and Surfaces. Gerz, T., Schwarz, C., ed., *The DLR Project Wetter & Fliegen - Forschungsbericht 2012-02*, pp. 222–232.

Georges, L., Geuzaine, P., Duponchel, M., Bricteux, L., Lonfils, T., Winckelmans, G., Giovannini, A. (2005), Technical Report 3.1.1-3, LES of two-vortex system in ground effect with and without wind. Techn. Ber., Université catholique de Louvain (UCL), Institut de Mécanique des Fluides de Toulouse(IMFT).

Germano, M., Piomelli, U., Moin, P., Cabot, W. H. (1991), A dynamic subgrid-scale eddy viscosity model. *Physics of Fluids*, vol. 3, pp. 1760–1765.

Gerz, T., Holzäpfel, F., Darracq, D. (2002), Commercial aircraft wake vortices. *Progress in Aerospace Sciences*, vol. 38, No. 3, pp. 181–208.

Gerz, T., Schumann, U., Elgobashi, S. E. (1989), Direct numerical simulation of stratified homogeneous turbulent shear flows. *Journal of Fluid Mechanics*, vol. 200, pp. 563–594.

Grötzbach, G. (1987), Direct numerical and large eddy simulations of turbulent channel flows. *Encyclopedia of fluid mechanics (ed. N. Cheremisinoff).* West Orange, NJ.

Hah, C., Lakshminarayana, B. (1982), Measurement and prediction of mean velocity and turbulence structure in the near wake of an airfoil. *Journal of Fluid Mechanics*, vol. 115, pp. 251–282.

Harris, D., Williamson, C. (2012), Instability of secondary vortices generated by a vortex pair in ground effect. *Journal of Fluid Mechanics*, vol. 700, pp. 148–186.

Harris, M., J.M. Vaughan, J. M., Hünecke, K., Hünecke, C. (2000), Aircraft wake vortices: a comparison of wind-tunnel data with field trail measurements by laser radar. *Aerospace Science and Technology*, vol. 4, No. 5, pp. 363–370.

Harvey, J., Perry, F. (1971), Flow field produced by trailing vortices in the vicinity of the ground. *AIAA Journal*, vol. 9(8), pp. 1659–1660.

Hecker, P. (2006), *Flugführungssysteme (Flugführung II).* Technische Universität Braunschweig.

Hennemann, I. (2010), *Deformation und Zerfall von Flugzeugwirbelschleppen in turbulenter und stabil geschichteter Atmosphäre.* PhD Thesis, Technische Universität München.

Hennemann, I., Holzäpfel, F. (2011), Large-Eddy simulation of aircraft wake vortex deformation and topology. *Journal of Aerospace Engineering*, vol. 25, pp. 1336–1350.

Hinton, D., Tatnall, C. (1997), A Candidate Wake Vortex Strength Definition for Applications to the NASA Aircraft Vortex Spacing System (AVOSS), NASA Technical Memorandum 110343. Techn. Ber., Langley Research Center, Hampton, Virginia, 1997.

Hirt, C. W., Cook, J. L. (1972), Calculating three-dimensional flows around structures and over rough terrain. *Journal of Computational Physics*, vol. 10, pp. 324.

Hokpunna, A. (2009), *Compact Fourth-order Scheme for Numerical Simulations of Navier-Stokes Equations.* PhD Thesis, Technische Universität München (Germany).

Hokpunna, A., Manhart, M. (2010), Compact Fourth-order Finite Volume Method for Numerical Solutions of Navier-Stokes Equations on Staggered Grids. *Journal of Computational Physics*, vol. 229, No. 20, pp. 7545–7570.

Holzäpfel, F. (2003), Probabilistic Two-Phase Wake Vortex Decay and Transport Model. *Journal of Aircraft*, vol. 40, No. 2, pp. 323–331.

Holzäpfel, F. (2004), Adjustment of Subgrid-Scale Parametrizations to Strong Streamline Curvature. *AIAA Journal*, vol. 42, No. 7, pp. 1369–1377.

Holzäpfel, F., Dengler, K., Gerz, T., Schwarz, C. (2011), Prediction of Dynamic Pairwise Wake Vortex Separations for Approach and Landing. *3rd AIAA Atmospheric Space Environments Conference*. Honululu, Hawaii.

Holzäpfel, F., Gerz, T., Baumann, R. (2001), The Turbulent Decay of Trailing Vortex Pairs in Stably Stratified Environments. *Aerospace Science and Technology*, vol. 5, No. 2, pp. 95–108.

Holzäpfel, F., Gerz, T., Frech, M., Tafferner, A., Köpp, F., Smalikho, I., Rahm, S., Hahn, K.-U., Schwarz, C. (2009), The Wake Vortex Prediction and Monitoring System WSVBS - Part I: Design. *Air Traffic Control Quarterly*, vol. 17, No. 4, pp. 301–322.

Holzäpfel, F., Gerz, T., Köpp, F., Stumpf, E., Harris, M., Young, R. I., Dolphi-Bouteyre, A. (2003a), Strategies for Circulation Evaluation of Aircraft Wake Vortices Measured by Lidar. *Journal of Atmospheric and Oceanic Technology*, vol. 20, No.8, pp. 1183–1195.

Holzäpfel, F., Hofbauer, T., Darracq, D., Moet, H., Garnier, F., Ferreira Gago, C. (2003b), Analysis of wake vortex decay mechanisms in the atmosphere. *Aerospace Science and Technology*, vol. 7, pp. 263–275.

Holzäpfel, F., Robins, R. E. (2004), Probabilistic Two-Phase Aircraft Wake-Vortex Model: Application and Assessment. *Journal of Aircraft*, vol. 41, No. 5, pp. 1117–1126.

Holzäpfel, F., Steen, M. (2007), Aircraft Wake-Vortex Evolution in Ground Proximity: Analysis and Parametrization. *AIAA Journal*, vol. 45, pp. 218–227.

Hultmark, M., Calaf, M., Parlange, M. B. (2013), A New Wall Shear Stress Model for Atmospheric Boundary Layer Simulations. *Journal of the Atmospheric Sciences*, vol. 70, pp. 3460–3470.

Hünecke, K. (2001), The Characterization of transport aircraft vortex wakes. *AIAA Paper 2001-2427*.

Jacquin, L., Fabre, D., Geffroy, P., Coustols, E. (2001), The properties of a transport aircraft wake in the extended near field: an experimental study. *AIAA Conference Proceedings*, 2001-1038.

Jategaonkar, R. V. (2006), *Flight Vehicle System Identification*. Progress in Astronautics and Aeronautics.

Jeong, J., Hussain, F. (1995), On the identification of a vortex. *Journal of Fluid Mechanics*, vol. 285, pp. 69–94.

Jimenez, J., Moin, P. (1991), The minimal flow unit in near-wall turbulence. *Journal of Fluid Mechanics*, vol. 225, pp. 213–240.

Kalnay, E. (2003), *Atmospheric Modeling, Data Assimilation and Predictability*. Cambridge University Press.

Keye, S. (2011), Fluid-Structure Coupled Analysis of a Transport Aircraft and Flight-Test Validation. *Journal of Aircraft*, vol. 48, No. 2, pp. 381–390.

Kobayashi, M. H. (1999), On a Class of Páde Finite Volume Methods. *Journal of Computational Physics*, vol. 156, No. 1, pp. 137–180.

Konrath, R., Agocs, J., Geisler, R., Otter, D., Roosenboom, E., Wolf, T., Quest, J. (2013), Flow Field Measurements by PIV at High Reynolds Numbers. *AIAA Paper 2013-0869, 51st AIAA Aerospace Sciences Meeting,*. Grapevine, Texas, USA.

Konrath, R., Carmer, C., Schrauf, G., Schmidt, K., Winckelmans, G., Cottin, C., Desenfans, O., G., D., Cocle, R. (2008), Dynamics and decay of spatially-evolving two- and four-vortex wakes near the ground. Techn. Ber., FAR-Wake project deliverable D 3.1.2.

Konrath, R., Pallek, D., Mattner, H., v.Cramer, C. (2009), Analysis of flow field measurements obtained in a large tow tank regarding the decay of wake vortices in the far-field for two- and four-vortex systems. *AIAA-Paper 2009-342, 47th AIAA Aerospace Science Meeting, Orlando (Florida)*.

Kundu, P. K., Cohen, I. M. (1990), *Fluid Mechanics*. Academic Press.

Köpp, F., Rahm, S., Smalikho, I. (2004), Characterisation of Aircraft Wake Vortices by 2-μm Doppler Lidar. *Journal of Atmospheric and Oceanic Technology*, vol. 21, pp. 194–206.

Labbe, O., Stumpf, E., Sagaut, P., Rudnik, R. (2001), Near- to midfield wake: numerical prediction. *Proceedings ODAS 2001, S3-1, ONERA-DLR Aerospace Symposium*. Paris, France.

Lamb, H. (1932), *Hydrodynamics*. Cambridge University Press, 6. Aufl.

Lanchester (1907), *Aerodynamics*. A. Constable, London.

Lang, S., Lunsford, C. (2013), RECAT 1: Lessons Learned from MEM. *WakeNet-Europe Workshop*.

Lele, S. K. (1992), Compact finite difference schemes with spectral-like resolution. *Journal of Computational Physics*, vol. 103, pp. 16.

Lewellen, D. C., Lewellen, W. S., Poole, L. R., DeCoursey, R. J., Hansen, G. M., Hostetler, C. A., Kent, G. S. (1998), Large-Eddy Simulations and Lidar Measurements of Vortex-Pair Breakup in Aircraft Wakes. *AIAA Journal*, vol. 36, No. 8, pp. 1439–1445.

Manhart, M. (2004), A Zonal Grid Algorithm for DNS of Turbulent Boundary Layer. *Computer and Fluids*, vol. 33, No. 3, pp. 435–461.

Manhart, M., Friedrich, R. (2002), DNS of a Turbulent Boundary Layer with Separation. *International Journal of Heat and Fluid Flow*, vol. 23, No.5, pp. 572–581.

Margolin, L. G., Smolarkiewicz, P. K., Wyszogrodzki, A. A. (2002), Implicit Turbulence Modeling for High Reynolds Number Flows. *ASME Journal of Fluids Engineering*, vol. 124, pp. 862–7.

Marshall, J. S. (1997), The flow induced by periodic vortex rings wrapped around a columnar vortex core. *Journal of Fluid Mechanics*, vol. 345, pp. 1–30.

Marshall, J. S., Beninati, M. L. (2005), External turbulence interaction with a columnar vortex. *Journal of Fluid Mechanics*, vol. 540, pp. 221–245.

Marshall, J. S., Brancher, P., Giovannini, A. (2001), Interaction of unequal anti-parallel vortex tubes. *Journal of Fluid Mechanics*, vol. 446, pp. 229–252.

Meneveau, C., Lund, T. S., Cabot, W. H. (1996), A Lagrangian dynamic subgrid-scale model of turbulence. *Journal of Fluid Mechanics*, vol. 319, pp. 353–385.

Misaka, T., Holzäpfel, F., Gerz, T. (2010), Large Eddy Simulation of Wake Vortex Flows: A Comparison of EULAG and MGLET. Techn. Ber., Institut für Physik der Atmosphäre, Deutsches Zentrum für Luft- und Raumfahrt.

Misaka, T., Holzäpfel, F., Gerz, T. (2012a), Wake Evolution of Wing-Body Configuration from Roll-Up to Vortex Decay. *AIAA Paper 2012-0428, 50th AIAA Aerospace Sciences Meeting including the New Horizons Forum and Aerospace Exposition, Nashville, Tennessee, USA.*, 2012-0428, pp. pp. 1–15.

Misaka, T., Holzäpfel, F., Gerz, T. (2013), Wake Evolution of High-Lift Configuration from Roll-Up to Vortex decay. *AIAA Paper 2013-0362, 51st AIAA Aerospace Sciences Meeting, Grapevine, Texas,USA.*

Misaka, T., Holzäpfel, F., Hennemann, I. Gerz, T., Manhart, M., Schwertfirm, F. (2012b), Vortex bursting and tracer transport of a counter-rotating vortex pair. *Physics of Fluids*, vol. 24, pp. (025104–1) – (025104–21).

Moet, H., Laporte, F., Chevalier, G., Poinsot, T. (2005), Wave propagation in vortices and vortex bursting. *Physics of Fluids*, vol. 17, pp. 054109.

Monin, A., Obukhov, A. (1954), Basic laws of turbulence mixing in the surface layer of the atmosphere. *Tr. Geofiz. Inst., Akad. Nauk SSSR*, vol. 24, pp. 163–187.

Moser, R. D., Kim, J., Mansour, N. (1999), Direct numerical simulation of turbulent channel flow up to Re=590. *Physics of Fluids*, vol. Vol. 11, 4, pp. 943–945.

Ortega, J. M., Bristol, R. L., Savas, Ö. (2002), Wake Alleviation Properties of Triangular-Flapped Wings. *AIAA Journal of Aircraft*, vol. 40, pp. 709–721.

Ortega, J. M., Bristol, R. L., Savas, Ö. (2003), Experimental study of the instability of unequal strength counter-rotating vortex pairs. *Journal of Fluid Mechanics*, vol. 474, pp. 35–84.

Piomelli, U., Balaras, E. (2002), Wall-Layer Models for Large-Eddy Simulations. *Annual Review of Fluid Mechanics*, vol. 34, pp. 349–374.

Pistolesi, E. (1937), Ground Effect - Theory and Practice, Technical Memorandum no. 828. Techn. Ber., National Advisory Committee for Aeronautics, Washington.

Prandtl, L. (1918), Tragflügeltheorie, 1. Mitteilung. *Nachrichten von der königlichen Gesellschaft der Wissenschaften zu Göttingen, Mathematisch-pysikalische Klasse*, pp. 451–477.

Prandtl, L. (1919), Tragflügeltheorie, 2. Mitteilung. *Nachrichten von der königlichen Gesellschaft der Wissenschaften zu Göttingen, Mathematisch-pysikalische Klasse*, pp. 107–137.

Prandtl, L. (1923), Der induzierte Widerstand von Mehrdackern. Techn. Ber., Ergebnisse der Aerodynamischen Versuchsanstallt Göttingen, II. Lieferung.

Proctor, F. H. (1998), The NASA Wake Vortex Modeling Effort in Support of an Operational Aircraft Spacing System. *AIAA Paper 98-0589.*

Proctor, F. H., Hamilton, D. W., Han, J. (2000), Wake Vortex Transport and Decay in Ground Effect: Vortex Linking with the Ground. *AIAA, 2000-0757, 38th Aerospace Sciences Meeting & Exhibit, Reno.*

Reynolds, O. (1895), On the Dynamical Theory of incompressible Viscous Fluids and the Determination of the Criterion. *Philos. Trans. R. Soc. London Ser. A*, vol. 186, pp. 123–164.

Robins, R., Delisi, D., Green, G. (2001), Algorithm for prediction of Trailing Vortex Evolution. *AIAA Journal of Aircraft*, vol. 38 No 6, pp. 1030–1040.

Rossow, V. (1999), Lift-Generated Vortex Wakes of Subsonic Transport Aircraft. *Progress in Aerospace Sciences*, vol. 35 No 6, pp. 592–599.

Rossow, V. (2002), Reduction of Uncertainties in Prediction of Wake-Vortex Locations. *AIAA Journal of Aircraft*, vol. 39 No 6, pp. 587–596.

Rotta, J. C. (1972), *Turbulente Strömungen.* B. G. Teubner Stuttgart, ISBN 3-519-02316-4.

Saffman, P. G. (1979), The approach of a vortex pair to a plane surface in inviscid fluid. *Journal of Fluid Mechanics*, vol. 92(3), pp. 497–503.

Saffman, P. G. (1992), *Vortex Dynamics.* Cambridge University Press, ISBN: 0-521-42058-X.

Samulat, G. (2013), Großer Wirbel um die Turbulenz. *Spectrum der Wissenschaft*, vol. 01, pp. 50–59.

Schlichting, H., Gersten, G. (1997), *Grenzschicht-Theorie*. Springer.

Schlichting, H., Truckenbrodt, E. (1967), *Aerodynamik des Flugzeugs*, vol. 2. Springer-Verlag Berlin Heidelberg New York, 2. Aufl.

Schmidt, H., Schumann, U. (1989), Coherent structures of the convective boundary layer derived from large-eddy simulations. *Journal of Fluid Mechanics*, vol. 200, pp. 511–562.

Schumann, U. (1975), Subgrid Scale Model for Finite Differences Simulations of Turbulent Flows in Plane Channels and Annuli. *Journal of Computational Physics*, vol. 18, pp. 376–404.

Schwamborn, D., Gerhold, T., Heinrich, R. (2006), The DLR TAU-Code: Recent Applications in Research and Industry. *European Conference on Computational Fluid Dynamics, ECCOMAS CDF*.

Schwarzer, H. S., Schwertfirm, F., Manhart, M., Schmidt, H. J., Peukert, W. (2006), Predictive Simulation of Nanoparticle Precipitation Based on the Population Balance Equation. *Chemical Engineering Science*, vol. 61, No.1, pp. 167–181.

Schwertfirm, F., Gradl, J., Schwarz, C., Peukert, W., Manhart, M. (2007), The Low Reynolds Number Turbulent Flow and Mixing in a Confined Impinging Jet Reactor. *International Journal of Heat and Fluid Flow*, vol. 28, No.6, pp. 1429–1442.

Shaw, R. H., Schumann, U. (1992), Large-Eddy Simulation of Turbulent Flow above and within a Forest. *Boundary-Layer Meteorology*, vol. 61, pp. 47–64.

Shen, S., Ding, F., Han, J., Proctor, F. H. (1999), Numerical Modeling Studies of Wake Vortices: Real Case Simulations. *37th AIAA Aerospace Sciences Meeting and Exhibit*. Reno, Nevada, USA.

Smalikho, I., Rahm, S. (2010), Lidar Investigations of the Effects of Wind and Atmospheric Turbulence on an Aircraft Wake Vortex. *Journal of Atmospheric and Oceanic Technology*, vol. 23 No.2, pp. 137–146.

Smits, A. J., Marusic, I. (2013), Wall-Bounded Turbulance. *Physics Today*, vol. 66, No. 9, pp. 25–30.

Smolarkiewicz, P. K. (2006), Multidimensional Positive Definite Advection Transport Algorithm: An Overview. *International Journal of Numerical Methods in Fluids*, vol. 50, No.10, pp. 1123–1144.

Spalart, P. (1998), Airplane trailing vortices. *Annual Review of Fluid Mechanics*, vol. 30(1), pp. 107–138.

Spalart, P., Strelets, M., Travin, A., Shur, M. (2001), Modeling the Interaction of a Vortex Pair with the Ground. *Fluid Dynamics*, vol. 36(6), pp. 899–908.

Spalart, P. R. (2009), Detached-Eddy Simulation. *Annual Review of Fluid Mechanics*, vol. 41, pp. 181–202.

Steen, M. (2005), *Analyse und Parametrisierung des Wirbelschleppenverhaltens in Bodennähe*. Master Thesis, Technische Universität Braunschweig.

Stephan, A., Holzäpfel, F., Misaka, T. (2012), Aircraft Wake Vortex Decay in Ground Proximity - Physical Mechanisms and Artificial Enhancement. *AIAA-Paper 2012-2672-285, 4th AIAA Atmospheric and Space Environments Conference, New Orleans (Louisiana).*

Stephan, A., Holzäpfel, F., Misaka, T. (2013a), Aircraft Wake Vortex Decay in Ground Proximity - Physical Mechanisms and Artificial Enhancement. *Journal of Aircraft*, vol. 50, No. 4, pp. 1250–1260. Doi: http://arc.aiaa.org/doi/abs/10.2514/1.C032179.

Stephan, A., Holzäpfel, F., Misaka, T. (2013b), Towards Realistic Simulation of Wake-Vortex Evolution during Landing with Flat and Complex Terrain. *TSFP-8 conference*, AER1A. Poitiers, France.

Stephan, A., Holzäpfel, F., Misaka, T. (2014), Hybrid Simulation of Wake-Vortex Evolution During Landing on Flat Terrain and with Plate Line. *International Journal of Heat and Fluid Flow*, vol. special issue on the tsfp-8 conference. Submitted.

Stephan, A., Holzäpfel, F., Misaka, T., Geisler, R., Konrath, R. (2013c), Enhancement of Aircraft Wake Vortex Decay in Ground Proximity - Experiment versus Simulation. *CEAS Aeronautical Journal*. Accessed November 30, 2013, doi:http://www.springerlink.com/openurl.asp?genre=article&id=doi:10.1007/s13272-013-0094-8.

Stumpf, E. (2005), Study of Four-Vortex Aircraft Wakes and Layout of Corresponding Aircraft Configurations. *Journal of Aircraft*, vol. 42, pp. 722–730.

Sujudi, D., Haimes, R. (1995), Identification Of Swirling Flow In 3-D Vector Fields.

Sun, X.-H. (1995), Application and accuracy of the parallel diagonal dominant algorithm. *Parallel Computing*, vol. 21, No. 8, pp. 1241–1267.

Tchipev, N. (2013), *Numerical Simulation of Wind Impact on Transport and Decay of Wake Vortices of Landing Aircraft*. Master Thesis, Technical University of Munich.

Trenkle, F. (1999), *Einführung in Luftdatensysteme: Pitotstatik, Anstell- und Schiebewinkelmessung, Vereisung und Eisschutz.* Thomas.

Widnall, S., Barrows, T. M. (1970), An analytic solution for two- and three-dimensional wings in ground effect. *Journal of Fluid Mechanics*, vol. 41, part 4, pp. 769–792.

Wieselsberger, C. (1922), Wing Resistance near the ground. *NACA TM-77*, vol. 77.

Williamson, J. H. (1980), Low-storage Runge-Kutta Schemes. *Journal of Computational Physics*, vol. 35, No. 48, pp. 48–56.

Winckelmans, G., Cocle, R., Dufresne, L., Capart, R. (2005), Vortex Methods and Their Application to Trailing Wake Vortex Simulations. *Compte Rendus Physique*, vol. 6, pp. 467–486.

Yi, J., Kim, C. (2013), Design Optimization of Vortex Generators for a Junction Vortex of Wing-Body Configuration by Discrete Adjoint Approach. *51st AIAA Aerospace Sciences Meeting, Grapevine, Texas,USA*.

Zhang, Q., Lee, S. W., Ligrani, P. M. (2004), Effects of surface roughness and free stream turbulence on the wake turbulence structure of a symmetric airfoil. *Physics of Fluids*, vol. 16, No. 6, pp. 2044–2053.

Acknowledgments

I received a lot of support and inputduring the course of the work, so many people have a stake in the present thesis. First of all I would like to express my gratitude to my mentor Frank Holzäpfel, particularly, for the magnificent subject - the elaboration of his patent with LES. Beside his ongoing support, he was always ready for questions and discussions, which gave me the impression of always being of high priority. I would like to thank Prof. George Craig for supervising this thesis and for his helpful comments and valuable suggestions during the course of the work. I would also like to thank Prof. Ulrich Schumann for supervising this thesis as a co-examiner as well as for his bright ideas and beneficial comments. I'm deeply grateful having closely worked together with my dear colleague and friend Takashi Misaka and about the heritage he left at the institute.

I would also like to thank Dr. Reinhard Geisler as well as Dr. Robert Konrath (Institut für Aerodynamik und Strömungstechnik, DLR-Göttingen), for their fruitful and ongoing cooperation and the significance this work got due to the towing tank experiments. I would like to thank Christian Raab (Institut für Flugsystemtechnik, DLR Braunschweig) for providing flight measurement data, as well as Stefan Melber (Institut für Aerodynamik und Strömungstechnik, DLR-Braunschweig) for providing the RANS flow field of the AWIATOR long range aircraft model. I also acknowledge Airbus for the allowance to use it. I would like to thank Stephan Körner for the evaluation of the Wake MUC data, as well as Michael Manhart (TUM) for his fruitful cooperation and the provision of the original version of the LES code MGLET. Computer time provided by Leibniz-Rechenzentrum (LRZ), Juropa (Jülich) and DKRZ is greatly acknowledged, as well as the support I got from Andreas Dörnbrack. Also I would like to thank Gregor Hochleitner and Thomas Ruppert (DFD), for the fancy landing videos they generated with Autodesk. I would like to thank Nikola Thipev, who I had the opportunity to supervise, for his accurate work and improvement of the code performance. Moreover, I deeply appreciate the suggestions, help and encouragement of my colleagues Thomas Gerz, Winfried Beer, Dennis Stich, Martin Köhler, Simon Kriegel and Peter Mühlbauer.

I would like to express my personal gratitude to my childreen and particularly to my unique wife Galina. The success of this thesis is owed to her dedicated and passionate care for the family. From the bottom of my heart I thank God the father, for his encouragement, the Son, for the delight in working he provides, and the Holy Spirit for his amazing leadership.

S. D. G.